Experimental and Numerical Investigation into the Destemming of Grapes

by
Stephanus Gerhardus Lombard

Thesis presented in partial fulfilment of the requirements for the degree Master of Science in Mechanical Engineering at the University of Stellenbosch

Supervisor: Dr. Corné Coetzee
Faculty of Engineering
Department of Mechanical and Mechatronic Engineering

March 2011

Declaration

By submitting this thesis electronically, I declare that the entirety of the work contained therein is my own, original work, that I am the authorship owner thereof (unless to the extend explicitly otherwise stated) and that I have not previously in its entity or in part submitted it for obtaining any qualification.

Date: …………………..........

Signature:…………………….
         S.G. Lombard

Abstract

The removal of grape berries from the stems is an important step in the wine making process. Various problems are experienced using the destemming machines currently available, where the berries are mechanically removed and separated from the stems by a rotating beater shaft and drum. Not all berries are removed from the stems and broken stems can end up with the removed berries which can result in unwanted characters and flavours in the wine. The development of these machines is currently limited to experimental tests.

In this study, the destemming process was investigated experimentally. The ability of the Discrete Element Method (DEM) to simulate this process was also investigated. A range of experiments was designed to obtain the material properties of the grapes. These experiments included the measurement of the stem stiffness and break strength, the berry stiffness, and the force needed to remove a berry from the stem.

Experiments were conducted to gain further insight into the destemming process. Firstly, a simplified destemming machine with only a beater shaft and a single grape bunch was built. The influence of the bunch size and the speed of the beater shaft on the number of berries removed from the stems were investigated. Secondly, field tests on a commercial destemming machine were conducted and the performance of the machine was measured.

A DEM model of both the simplified and the commercial destemming machine were built. Commercial DEM software was used with linear contact and bond models. The stems were built from spherical particles bonded together and a single spherical particle was used to represent each berry. The measured stiffnesses and break strengths were used to set the particle and bond properties. Modelling the simplified destemming machine, it was found that the DEM model could accurately predict the effect of the bunch size and the speed of the beater shaft on the number of berries removed from the stems. The model of the commercial destemming machine could accurately predict the machine's performance in terms of the number of berries removed as well as the number of broken stems.

ii

Opsomming

Die verwydering van druiwekorrels vanaf die stingels is 'n belangrike stap tydens die wynmaak proses. Verskeie probleme word ondervind met huidige beskikbare ontstingelaars, waar die korrels meganies verwyder en skei word vanaf die stingels deur middel van 'n roterende klop-as en drom. Nie alle korrels word vanaf die stingels verwyder nie en gebreekte stingels kan saam met die verwyderde korrels beland, wat ongewensde karakters en geure in die wyn kan veroorsaak. Die ontwikkeling van ontstingelaars is tans beperk tot eksperimentele toetse.

In hierdie studie is die ontstingel proses eksperimenteel ondersoek Die vermoë van die Diskrete Element Metode (DEM) om hierdie proses te simuleer is ook ondersoek. 'n Reeks eksperimente is ontwikkel om die materiaal eienskappe van die druiwe te bepaal. Hierdie eksperimente sluit in die meet van die styfheid en breeksterkte van die stingel, die korrel styfheid, en die krag benodig om 'n korrel vanaf die stingel te verwyder.

Eksperimente is gedoen om verdere insig oor die ontstingel proses te bekom. Eerstens is 'n vereenvoudigde ontstingelaar gebou, met slegs 'n klop-as en een tros. Die invloed van die trosgrootte en die klop-as spoed op die aantal korrels wat verwyder is, is ondersoek. Tweedens is 'n toets in die veld gedoen met 'n kommersiële ontstingelaar om die werkverrigting van die masjien te bepaal.

'n DEM model van beide die vereenvoudigde en kommersiële ontstingelaar is gebou. Kommersiële DEM sagteware is gebruik met lineêre kontak- en bindingsmodelle. Die stingels is gebou deur sferiese partikels aan mekaar te bind en 'n enkele sferiese partikel is gebruik om 'n druiwe korrel voor te stel. Die gemete styfhede en breeksterktes is gebruik om die partikel- en bindingseienskappe te spesifiseer. Die modellering van die vereenvoudigde ontstingelaar het getoon dat die DEM model akkuraat kan voorspel wat die invloed is van die trosgrootte en die klop-as spoed op die aantal korrels wat verwyder is. Die model van die kommersiële ontstingelaar kon die werkverrigting van die masjien akkuraat voorspel in terme van die aantal korrels wat verwyder is asook die aantal gebreekte stingels.

Acknowledgements

I would like to thank the following people and organisations for their help and support during my research:

- For their financial support I would like to thank:

    - Department of Mechanical and Mechatronic Engineering

    - Tienie Louw Bursary Fund

    - National Research Foundation (NRF)

- Joris van Almenkerk for making his cellar and equipment available to us for tests during the harvesting season.
- My supervisor, Dr. Corné Coetzee, for his good and helpful advice.

Table of Contents

List of Tables

List of Figures

1. Introduction

1.1. Background

As soon as grapes arrive at the cellar for wine making, the grape berries must be separated from the stems. For making wine, it is desirable to only have the good berries available. Impurities such as stems, green-, rotten- or sunburnt-berries or any other foreign objects can all have a negative influence on the wine.

The machines being used to separate the berries from the stems are called destemmers or destemming machines. Nearly all destemmers in use today use the same basic principle and layout. Currently available destemmers suffer from problems that mainly include stems ending up with berries, berries exiting with the stems, and occasional blockages. The destemmers are also unable to separate most of the other impurities found in grapes from the berries.

Very expensive sorting machines or highly labour intensive sorting lines are used to remove impurities from the grapes in order to improve the quality of the grapes used for wine making. These methods are only viable for low volume production rates (less than 15 tons per hour).

The development of current destemming machines relies entirely on experimental development and testing. A trial-and-error approach is often followed and the mechanics involved in the destemming of the grapes are not always understood completely. Since grapes are a seasonal produce, experimental developments are limited to a few months per year.

1.2. Objectives

The Discrete Element Method (DEM) is a numerical model used for the simulation of the mechanics of a system of particles, both under static and dynamic conditions. The ability of DEM to model the dynamic behaviour of grape bunches during the destemming process is investigated.

For the calibration of the DEM model, a range of experiments is designed and conducted. These experiments serve both as calibration method for the DEM model as well as to increase the understanding of the mechanics involved during the destemming process. The experiments include determining the material properties of the grapes, an experiment of a simplified destemmer replicating destemming conditions, as well as determining the performance of a commercial detemmer.

The accuracy of simulating the destemming of grapes using DEM is investigated. Material properties obtained from the experiments are used as initial values in the DEM model. These values are then calibrated by simulating an entire grape bunch under destemming conditions and comparing the results to the

experiments. As a final comparison, the model is used to simulate a commercial destemmer to validate the DEM model.

The aim of this study is not to solve the current problems associated with the destemming processes as used by industry, but rather to increase the understanding of the current processes and mechanics of destemming and destemming machines. Also, to investigate the ability of DEM to accurately model these processes so that in future, DEM can be used to solve the existing problems and to optimise the destemming process.

1.3. Motivation

In South Africa, as well as globally, the wine industry is known as a reliable and growing industry. Investments towards making better wine are being done worldwide and the technology being used by the wine industry is constantly being improved. Improving the destemming process is a much needed issue for the wine industry. The knowledge gained through this study can be applied to improve existing processes and the development of new technologies.

The possibility of developing a simulation model of the destemming process can result in a better understanding of the process, improvement of current machines as well as faster development of new concepts and machines. Using simulations for the development or improvement of machines can decrease development time as less prototypes need to be designed, build and tested. Tests can only be done during the harvesting season, but simulations can be done throughout the year. The decrease in development time, as well as the decrease in prototypes, can result in significant cost savings.

The knowledge and tools developed in this research can also be applied to other industries. These include the harvesting, packing, and the transportation of wine- and tablegrapes, as well as the processing of grapes for the food and juice industries. It can also be applied to the development of mechanical grape harvesting machines seeing as these machines use a technique similar to destemmer, when removing the grapes from the vines.

2. Literature

2.1. DEM

The DEM is a numerical method for studying the dynamic behaviour of particles (Raji & Favier, 2004a). It is very useful to study both individual particles as well as the behaviour of a system of particles.

DEM was originally used to simulate rocks and rock mechanics. However, due to the versatility of this method, it is possible to apply it in a much wider variety of applications and DEM has been used to simulate the flow characteristics of various granular materials. These applications range from pharmaceutical applications to agricultural applications, such as the simulation of centrifugal fertilizer spreaders. DEM has also been used to simulate various biomaterials, including rice, grain, oilseeds (Raji & Favier, 2004b) and soybeans (Zhang & Vu-Quoc, 2000). In these applications DEM was mainly used to study the flow characteristics and compressive loading of these materials. Other biomaterial simulations include studying the damage on apples during transportation (Van Zeebroeck *et al.*, 2008) and the bruising of tomatoes (Van Zeebroeck *et al.*, 2007a). However, no research can be found where it has been used to simulate grapes or grape bunches. An overview of the DEM background and theory is given in *Appendix A*.

2.2. DEM Simulations of Biomaterials

DEM has been used in various applications to simulate biomaterials. However, the application of DEM in the simulation of fruit handling is at present very limited. In the majority of the research done, the primary objectives of the studies are to determine damage and bruising of the fruit and not to determine the physical properties and dynamic behaviour of the fruit. A tactile sensing system was used by Herold *et al.* (2001) to measure the contact force distribution between fruit. The study focused on the mechanics involved when fruit is bruised, using apples for the experiments. Van Zeebroeck *et al.* (2003) developed a pendulum device to measure the contact force, displacement and displacement rate of an impactor during its impact on biological materials and were tested using apples, tomatoes and potatoes. The damage of apples due to vibration during transportation was studied by Van Zeebroeck *et al.* (2006) and the impact damage to apples during transport was studied by Van Zeebroeck *et al.* (2008).

In the agricultural and food growing industry, the firmness of fruit is often of great importance. Plenty of studies have been done, and are still being done, to use the firmness of fruit to indicate fruit properties, predict shelf life and determine its susceptibility to bruising (Van Zeebroeck et al., 2007b; Van Zeebroeck et al., 2007a).

2.3. Grapes and Wine

Wine making is an ancient practice and is reported in some of the oldest scripts known to man. Wine making has always been regarded as an art and even though the chemistry involved in today's processes are well known, wine making is still not an exact science. The chemistry involved is very complex, but winemakers know from experience which factors influence the wine, both in a positive and negative way.

The single most important factor when making wine is the grapes. Farmers and winemakers go to great lengths to ensure that the quality of the grapes is of a high standard. However, good quality grapes can still produce low quality wine if the wine making process is not executed carefully.

The process starts when the grapes arrive at the cellar and the berries are separated from the stems. Ideally, the berries used for the making of wine should be free from any stems, green-, rotten- or sunburnt berries, leaves or any other foreign objects. However, during the harvesting process, a variety of foreign objects can end up with the grapes including snails, or other insects, metal staples and stones. To control the process as efficiently as possible, to make the best wine possible, winemakers want only the ripe berries and none of these impurities. For example, winemakers know from experience that the green berries and stems can result in green phenolic flavours in the wine, while rotten and sunburnt berries can produce various flavours of rot (Falconer, 2006). For this reason, winemakers often go to great extents to remove these impurities from the grapes. However, current methods are only viable for low volume production rates (less than 15 tons per hour) and can't be used for higher production rates (see Section B.2. for more on sorting methods).

Two different methods are followed for the making of white and red wine. When making white wine, the berries are usually pressed directly after de-stemming to extract the juice. The juice is then fermented into wine and the fermentation process can be controlled in various ways, such as controlling the temperature. The winemaker can also add different types of yeasts. The juice must have as little exposure to oxygen as possible, to limit the growth of natural, unwanted yeasts. To prevent exposure of the wine to oxygen, inert gasses, such as nitrogen and carbon dioxide, are sometimes used to replace the oxygen carrying air around the grapes. An inert system called Kappa 15 Natural is offered by Diemme to limit oxidation effects (Diemme, 2010).

When making red wine, it is important to note that the juice that is obtained from the red cultivar grapes is not red but white. The red colour is extracted from the skins of the berries. After the grapes are destemmed and the juice is pressed from the berries, the pressed berries now known as the *skins*, are mixed back into the juice to allow the juice to extract the colour from the skins. The intensity of the colour of the wine is determined by the time it is in contact with the skins.

The fermentation process starts while the skins are still mixed with the juice. As the skins have an influence on the wine, it is important not to have included any unwanted elements such as stems mixed with the skins. When the winemaker is satisfied with the colour, the skins are removed from the fermenting juice and the juice continues to ferment on its own.

It is normally accepted that impurities have a greater influence on red wine than on white wine, as the impurities are in contact with the red wine for longer and can also start fermenting with the wine. The impurities in white wine are only in contact with the wine/juice while the juice is drained from the berries (Goussard & Du Toit, 2010).

South Africa grows a wide variety of both red and white cultivars but many more cultivars are grown all over the world. Each cultivar has its own characteristics of both the vines as well as the wine it produces. In this study, only the characteristics of the grape bunches are of interest. This includes the bunch size and shape, berry size and shape, the packing density of the berries in the bunch and the material properties of the bunch, for example, the stem tensile strength. The material properties of the grape bunch are influenced by a number of factors including the cultivar. The region where the grapes are grown, the irrigation schedule, the weather, the fertilizers used, the toxins used on the vines, diseases present in the vines, and many more factors can all influence the properties. The condition of the grapes is quantified by the winemakers by measuring various chemical levels in the grape berries and stems, such as the acid-, sugar- and pH-levels. These are not a direct indication of the material properties but are used more as a measurement of ripeness. Grape bunches from the same vine can also differ depending on where on the vine the bunches are located. The berries on a single bunch can also vary from green- to rotten berries and berries often vary along the length of the bunch.

2.4. De-Stemming Machines

2.4.1. Background
De-stemming machines (called destemmers) are machines that remove the grape berries from the stems as well as separate the stems and the berries. These machines are found at wine cellars and are used to separate the grape berries from the stems for the making of wine.

Stems need to be removed as they can add unwanted characters and flavours to the wine, in two ways: the most common way is during the making of red wine while the wine is in contact with the berry skins and unwanted stems. The second way is during the de-stemming process. If the de-stemming process is not delicate enough, the berries can burst and a number of stems can be bruised, broken or damaged. When the stems are severely damaged, juice from the

stems is mixed with the juice from the berries and in this way all the negative substances from the stems end up in the wine.

For this reason the destemmer is a very important machine when it comes to the wine making process. Not only should it separate the stems from the berries, but it must also handle the grapes in a delicate way in order to limit any damage to the stems.

The vast majority of current destemmers all use the same basic principle called the Amos-principle, developed in the 1940's in Germany (Amos, 2009). It entails first separating the stems and berries before the berries are crushed. Earlier machines first crushed the whole bunch and then separated the berries and the stems. This, however, caused severe damage to the stems and contamination of the grape juice. Berries get crushed to break the skin and release the juice. When crushing the berries it is important that the inside flesh of the berry stays intact as much as possible. If the berries are crushed to a pulp, it is very difficult to drain the juice from the berries. A good crusher should just break the berries open and leave the flesh intact so that the juice can easily be drained.
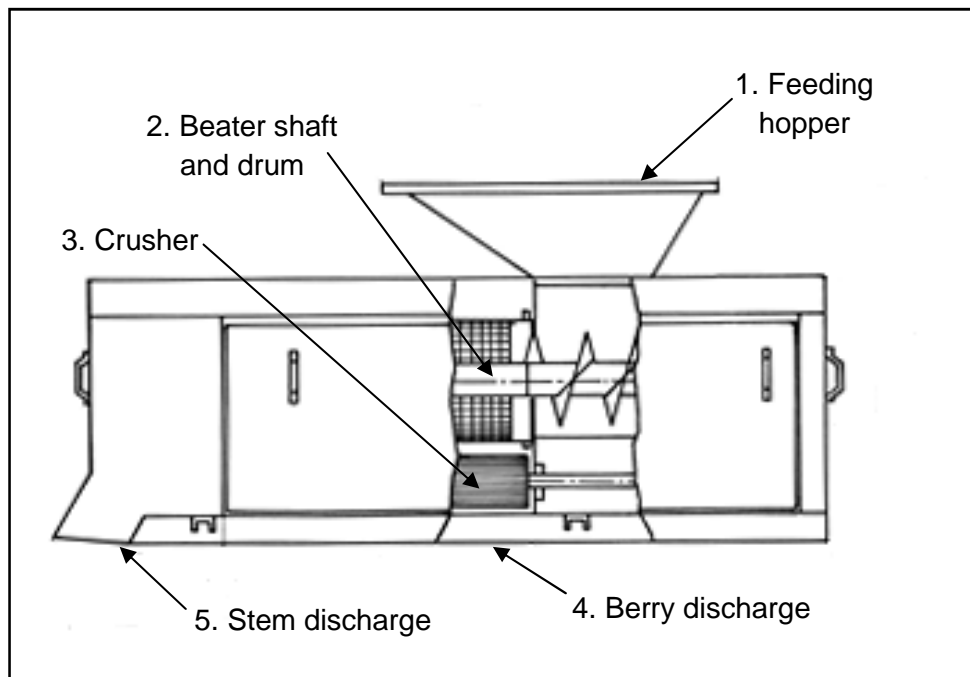
Figure 1 - The basic layout of a horizontal rotating destemmer (Zickler, 2009).

The most commonly used destemmers are horizontal rotating destemmers (also called centrifugal destemmers) which have two basic components called the beater shaft and the drum. Other types of destemmers that are used include vertical destemmers and linear destemmers. The basic layout of a Zickler destemmer, that represents a typical horizontal rotating destemmer, can be seen in Figure 1. The beater shaft consists of a shaft with pins positioned in a spiral around it like an auger. Usually the pins form more than one spiral (up to four).

6

The function of the beater shaft is to beat the berries from the grape bunches and the spiral shape of the pins moves the stems forward through the drum towards the stem discharge. The beater shaft rotates inside the drum, which acts as a rotating sieve. The berries that get beaten from the stems fall through the openings in the drum and into the crusher.

Depending on the manufacturer, the rotation of the drum and the beater shaft can either be in the same direction or in opposite directions. Normally the rotation speed of the drum and the beater shaft are a fixed ratio. The rotation speed is usually adjustable on smaller machines to achieve optimum performance for each batch of grapes. Since this optimum speed is determined by a trial-and-error approach, it takes some time to adjust the machine for each batch of grapes and the improvement can sometimes be very small. However, since smaller machines usually handle smaller quantities but higher value and quality grapes, great care is taken with this process to ensure the good quality of the wine. Larger machines must normally handle larger amounts of grapes and there is no time to adjust the machine for each batch of grapes. These machines normally operate at a fixed speed.

Although all machines use the same basic principle, there are still variations between the machines from different manufactures. Since the drum and beater shaft are the two main components of a destemmer, the most important variations all involve the drum and the beater shaft.
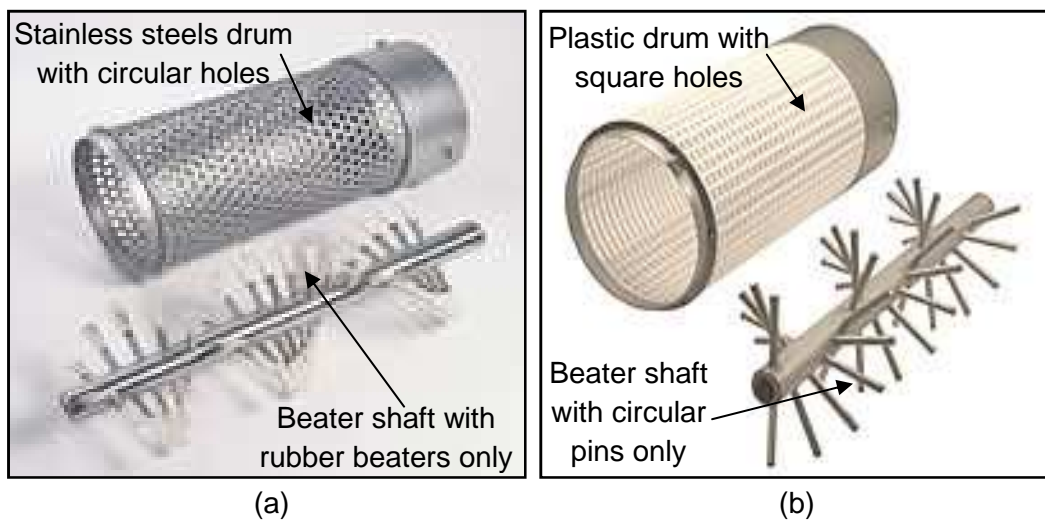
Figure 2 - Two types of beater shaft layouts and two types of drums found in destemmers (Zickler, 2009).

2.4.2. Drums

Drums can vary in length, diameter, rotation speed and direction, as well as hole size and shape. There are two basic types of drums that are used. The most popular type is the stainless steel drum with circular holes (Figure 2a); the other type is an aluminium drum (plastic has also been used) with square holes (Figure

2b). The size of the holes is of great importance and is usually chosen depending on the cultivar the machine would process most. Some wineries have up to three different interchangeable drums, with varying hole sizes, per machine (Phillips, 2005). The size of the holes can also vary along the length of the drum, starting with larger holes where the grape bunches enter the destemmer and smaller holes at the end of the drum where the stems exit. The reason for this distribution is that most of the berries are removed from the stems in the first quarter of the machine (Amos, 2009) and as a result there is a high concentration of berries in this part of the machine. Larger holes are used to ensure the berries can move through the drum as easily and quickly as possible. In this part of the machine the stems are usually still intact, since they have been exposed to very little beating, which means they are still large and do not pass through the holes. As the stem is moved along the length of the drum by the beater shaft's spiral pins, it can break into smaller pieces depending on the speed of the beater shaft as well as the properties of the stems. For this reason the holes in the drum are smaller towards the end of the drum to prevent pieces of stem passing through, but still allowing berries to pass through.

2.4.3. Beater shafts

Beater shafts can differ in length, rotation speed, diameter, type of pins, size of pins, the pitch of the pins and number of pins. Although the rotation speed of the beater shaft is of great importance, it is also important to note that one should take into account the diameter of the beater shaft to determine the tip speed of the beaters, since this is the maximum speed and acceleration that the grape bunches experience. Tip speeds of the beater tip range roughly from 2 to 5 m/s.

There are two types of pins that are used on beater shafts: cylindrical pins or rubber beaters (Figure 2a and b) or a combination of both. Both types of pins can range in size and length. When a combination of rubber beaters and cylindrical pins are used, the rubber beaters are located where the grape bunches enter the machine. Since the rubber beaters are larger that the cylindrical pins, the force is applied over a larger area of the grape bunch. This means that the stems are under less stress and the force is transmitted to more of the berries, knocking more berries from the stems. Some machines use large solid beaters at the start of the beater shaft where the grapes enter the machine, as shown in Figure 3. Manufacturers claim that this improves the removal of berries from the stems.

The pitch angle of the rubber beaters can usually be adjusted. This pitch angle influences the rate at which the grapes are moved through the machine. If the pitch is too high, the grapes will move too quickly through the machine and some berries will exit with the stems. If the pitch angle is set too low, the machine might get blocked. The rate at which the grapes are moved through the machine is also influenced by the pitch of the pins on the beater shaft.
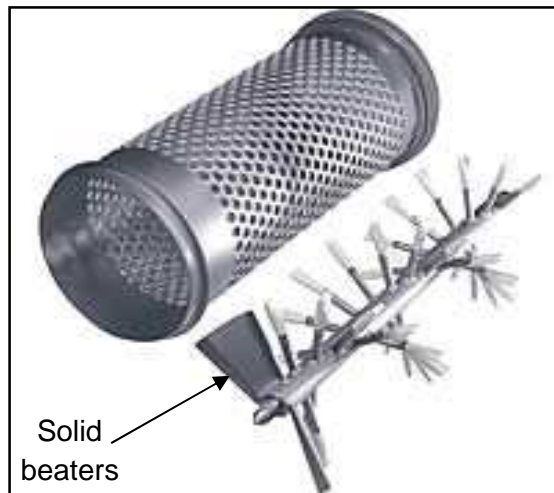
Figure 3 - Solid beaters shown where grapes enter the machine (Zickler, 2009).

Although some machines have only rubber beaters on the beater shaft, rubber beaters are much more expensive than cylindrical pins. For this reason rubber beaters are often only used where the grapes enter the machine to improve performance but cylindrical pins are used on the rest of the beater shaft to keep the cost down. On beater shafts that use cylindrical pins only, the pins can be placed closer to each other in order to produce a more equally distributed force over the bunches as they enter the machine.

The clearance between the beater shaft and drum can vary between different machines. Some machines have a small clearance so that the bunches cannot fit between the tip of the beater pins and the drum, while other machines use a larger clearance. The larger clearance allows bunches to move between the tip of the beater pins and the drum and this can create an affect where the bunches are milled between the drum and the beater shaft. This can help to improve the removing of berries from the stems but can slow down the movement of the grapes through the machine and cause more stem breakage. Some manufacturers use a small clearance for the first part of the drum and then increase the clearance in the second part. This helps to keep up the flow of the grapes through the machine, and berries that are not removed in the first part can then be removed in the second part of the machine where there is a larger clearance between the beater pins and the drum.

The length of the drum and beater shaft is an important variable when designing a destemmer. If the drum is too short, all the berries might not be able to fall through the drum and will exit with the stems which mean the capacity of the machine is reduced. An example of this comparison is the Magitec A5 and A15 machines (Figure 4). Both machines use the same basic drum and beater shaft, but the A5 is rated to handle 5 tons per hour, while the A15 machine, which is longer than the A5, is rated to handle 15 tons per hour. If the drum and beater shaft are too long, the stems need to be moved for a longer distance and stay in

the machine for a longer time which can result in more stem breakage. The breakage of the stems is a big problem in destemmers since the broken stems can pass through the drum and end up with the berries. From observations, if stems do fall through the drum with berries, it is usually in the last section of the machine.

Figure 4 - The Magitec A5 (left) and A15 (right) machines. Note the difference in length (Amos, 2009).

The feed rate of the machines can influence the performance. It is recommended that the machines are fed at their specified feed rate (Phillips, 2005). If the machine is fed too slowly, the stems might not be moved out of the machine quickly enough and this can result in stem breakage and stems ending up with the grape berries. If the machine is fed at too high a capacity, all the berries might not be removed or separated from the stems and berries might exit with the stems.

It is also important that the grapes are fed correctly into the machine – incorrect feeding influences the destemmer's performance. Grapes should be fed vertically into the machine, not at an angle as this gives the grapes an entrance velocity in the same direction as the grapes are already moving inside the machine. This can cause berries to exit with the stems (Amos, 2009).

3. Experiments

In this chapter, the experimental equipment, methods, material and results are presented.

3.1. Grapes

Natural products, such as grapes, tend to have large variations in physical, as well as chemical properties. Grapes coming from the same plant can vary in properties and this variation can be influenced by factors such as the location of the bunch on the plant, the number of bunches per shoot, its exposure to sunlight, etcetera. Grape properties in the same vineyard can vary due to influences such as the change in soil composition, irregular irrigation and wind exposure. Winemakers need to use multiple samples to determine the chemical composition of a batch. Other factors that can influence the state of the grapes include the trellising system used, the pruning system used, the presence of diseases and viruses in the vines, atmospheric influences during the development of the bunches and the treatment of the vines (Goussard & Du Toit, 2010).

To limit the variation in physical properties as far as possible, this study focused on one cultivar, Shiraz, from the farm Almenkerk Wine Estate, Grabouw, South Africa. Two batches of grapes from two vineyards were used to determine the physical properties. The results from each batch were processed separately to investigate the variation in physical properties.

Goussard & Du Toit (2010) suggested using Shiraz grapes in the experiments since this cultivar usually has very uniform shaped bunches and it is a well known cultivar in South Africa. Shiraz, also known as Syrah, originated in France and is also cultivated in Australia, Argentina and Italy. Shiraz bunches are described as medium sized bunches (12 to 18 cm long) with a long cylindrical shape and can be slightly shouldered (extensions of the bunch at the top), as shown in Figure 5. The berries are medium sized (12 to 18 mm in diameter at the equator), short-oval shaped with a thin skin and are packed fairly loose on the bunch (Goussard, 2008).

Two batches of Shiraz grapes from the Almenkerk Wine Estate were used for the experiments done on the 19th and 24th of March 2010. The Almenkerk Wine Estate were chosen since they cultivate Shiraz grapes and use a small Magitec A5 destemmer that feeds onto a sorting conveyor belt before crushing of the berries (Figure 4). This is an ideal setup to test the performance of the destemmer since the grapes can be monitored after destemming but before they are crushed. The Magitec A5 destemmer was also the machine of choice since it is a low volume machine (5 tons per hour) which makes it easier to measure the performance of the destemmer. All the necessary technical specifications were made available by Mr. Helmut Amos, the owner of Magitec.

11

(a)   (b)
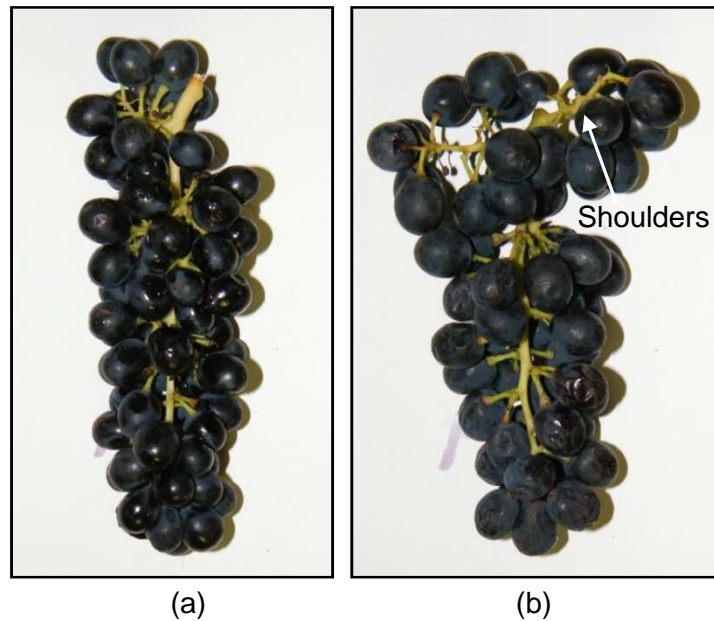
Figure 5 - Two typical Shiraz bunches: A cylindrical shaped bunch (a) and a bunch with two small shoulders (b).

A chemical analysis of the grapes was performed by the Department of Viticulture and Oenology at the University of Stellenbosch and a summary of the results is in Table 1.

Table 1 - Chemical analysis of grapes used in experiments.

Substance measured:	Reading:
Glucose	264
Brix	25.4
Density	1.11 kg/l
pH	3.20
Total Acid	6.11 g/l
Malic Acid	0.9
Folin C ind.	439.3
OD 280	66.8

3.2. Density

The density of the grape berries and stems was determined separately by weighing a sample of berries or stems and then submerging it into water and measuring the volume of water it displaced. The average density of the berries

12

was calculated as 1130 kg/m^3 and the density of the stems as 1108 kg/m^3. Table 2 shows the measured and calculated values for the two samples taken. The number of berries is used later as an additional verification of the average weight and volume of the berries.

Table 2 - Density of grape berries.

Test Number	Number of Berries	Weight of Berries [g]	Volume Displaced [ml]	Density [kg/m^3]
1	300	448	398	1126
2	300	454	400	1135

3.3. Stiffness and Tensile Strength

In order to build an accurate numerical model of a grape bunch, various measurements of strength and stiffness are needed. These include the stiffness of the berries and the force at which the berries burst, the force needed to remove the pedicel from the berry (Figure 6) and the stiffness between the berry and the pedicel, the strength and stiffness of the stems, and the strength and stiffness of the connection between a side and main stem. An experimental setup was designed to measure all these parameters.

Figure 6 - Berry with pedicel.

3.3.1. Experimental Setup

The experimental setup (Figure 7) was designed and built by Jarco Groenewald as part of his final year mechanical project in 2009 (Groenewald, 2009). It was designed to measure the stiffness of the grape stems and berries as well as the break strength. Force and displacement can be measured in both tension and compression. Force is measured using a 50 N load cell and displacement is measured using a linear inductive transducer with a range of 100 mm. Data sampling is done at a minimum of 100 Hz and the speed of the head can be varied from 0.24 mm/s to 2.4 mm/s. Two chucks from drilling machines are used to clamp the test specimen.
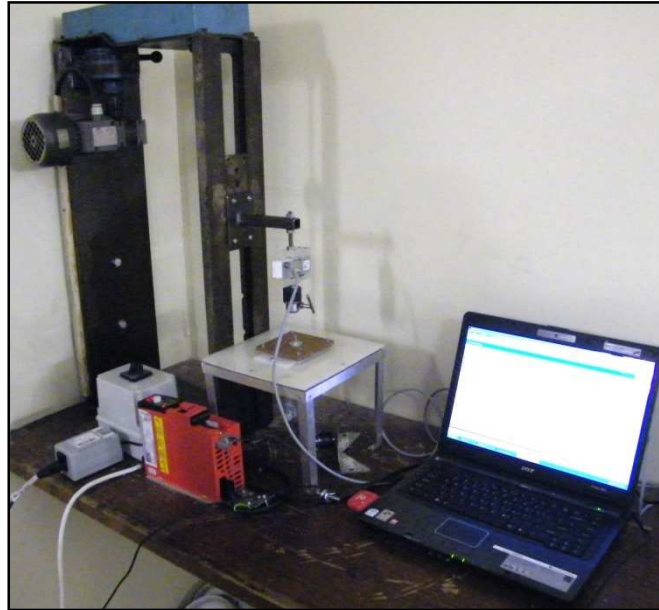
Figure 7 - The experimental setup used to measure the properties of the grapes.

Four types of experiments were conducted, namely: compression of a single berry, pulling the pedicel out of a berry, tensile loading of a stem, and shearing off a side stem from the main stem. Each type of experiment was conducted at three different speed settings (0.26 mm/s, 1.35 mm/s and 2.4 mm/s) and 25 tests were done at each of the three speed settings, resulting in 75 tests of each type. Kidd (2010) suggested that between 50 and 100 tests of each type should be done to achieve accurate statistical results. Two batches of grapes were used, resulting in a total of 150 tests per experiment type.

3.3.2. Data Processing

To describe the data processing, the compression of a berry is used as an example. The data collected from the experiments was first cleaned to eliminate any data that had been collected outside the experimental time period. (Figure 8). The start point was zeroed and a new force-displacement plot was drawn (Figure 9a). Four parameters were calculated from this data, namely: the failure force (Figure 9a), the force-based stiffness (Figure 9b), the total energy (Figure 9c), and the energy-based stiffness (Figure 9d).

The stiffness was assumed linear and calculated by using the displacement and force at the failure point (Figure 9a) and dividing the maximum force by the maximum displacement to determine the gradient of the stiffness line (Figure 9b). The stiffness calculated using this method is referred to in this document as the force-stiffness. It is important to note that some of the results from the other experiments showed much more linear behaviour than the compression of the berry.

14

The total amount of strain energy needed to achieve failure was determined by calculating the area under the force-displacement graph (Figure 9c) by using a Riemann sum. Note that the total energy was not used in the numerical simulation and is only included as additional data. This energy was then used to calculate a second stiffness, referred to in this document as the energy-stiffness. The energy-stiffness is calculated by drawing a second graph (Figure 9d) that has the same failure force and energy (area) as calculated from the experiment, but uses a linear stiffness and not the data line from the experiments. The result is a decrease in displacement and a new stiffness. Figure 9d shows the graph using the energy-stiffness as gradient. Using this linear stiffness, the total strain energy at failure will be equal to the total measured strain energy at the same failure force.

After the data from each experiment was processed, a histogram of the data from all experiments in that batch was drawn up. A normal distribution was fitted to the data and the mean, true variance, minimum and maximum values were calculated.
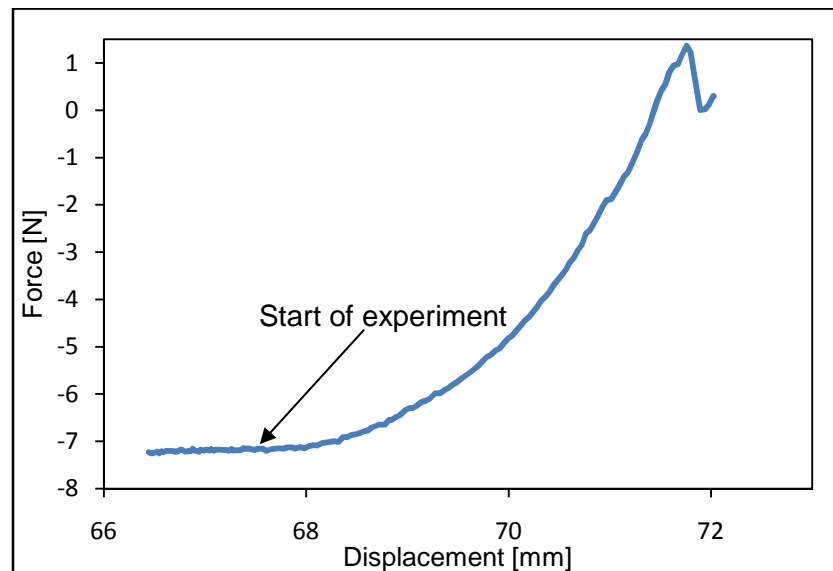
Figure 8 - Force-displacement graph of the raw data from experiments of compression of a berry.

Literature suggests that biomaterials might show visco-elastic behaviour and for this reason the experiments were conducted at three different speeds. However, no direct relation between the speed and the measured force in any of the experiments could be found. A possible reason for this is that the range of the three speed settings that was used was too small and ideally tests should be conducted using a much wider speed range. Due to the equipment limitations, this was not possible and the visco-elastic effect was ignored.
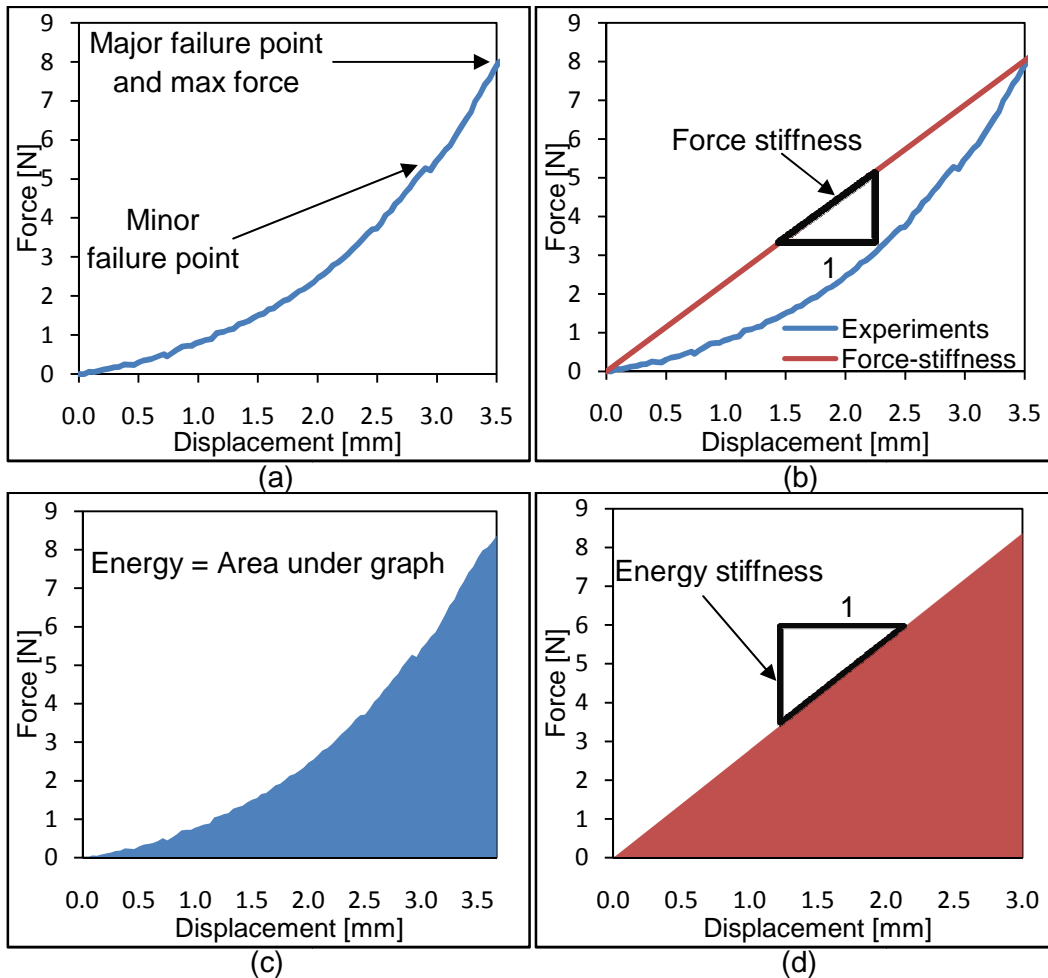
Figure 9 - Calculation steps for determining the force-stiffness (b), energy (c) and energy-stiffness (d) from the raw experimental data (a).

Dimensions of the berries and stems were taken during the experiments to find correlations between the calculated parameters and the physical dimensions of the grapes. These dimensions were also used to calculate the average berry size and stem diameter.

3.3.3. Compression of Berry

Berries were placed between two smooth and flat surfaces and compressed until the berry burst. As can be expected when compressing a spherical object, the force-displacement relation are non-linear, but since the contact model used in the numerical simulation of the berries is a linear contact model, linear behaviour was assumed in the processing of the data. See Section 4.2.3 for a comparison of the experimental results with other numerical non-linear contact models.

The results from the experiments were compared with the physical dimensions of the berries, but no noticeable relation could be found. It is therefore assumed that the stiffness and failure force of the berries are independent from these dimensions.

The results of the two batches of experiments and final averages are shown in Table 3. The final stiffness was taken as 2000 N/m and the failure force as 8 N. This results in a total displacement of 4 mm at failure which is acceptable since the average displacement of the experiments was 3.5 mm at the failure point.

Table 3 - Experimental results of compression of berries.

	Batch 1	Batch 2	Average
Failure Force [N]	6.9	8.7	7.8
Total Energy [Joule]	1.2E-02	1.3E-02	1.2E-02
Force-Stiffness [N/m]	1400	2100	1750
Energy-Stiffness [N/m]	2100	3100	2600

3.3.4. Pulling Pedicel out of Berry

The results from these experiments had a much more linear trend (Figure 10) than the results from the compression of the berries and as a result, a linear stiffness was a good assumption. The results from the experiments are shown in Table 4.
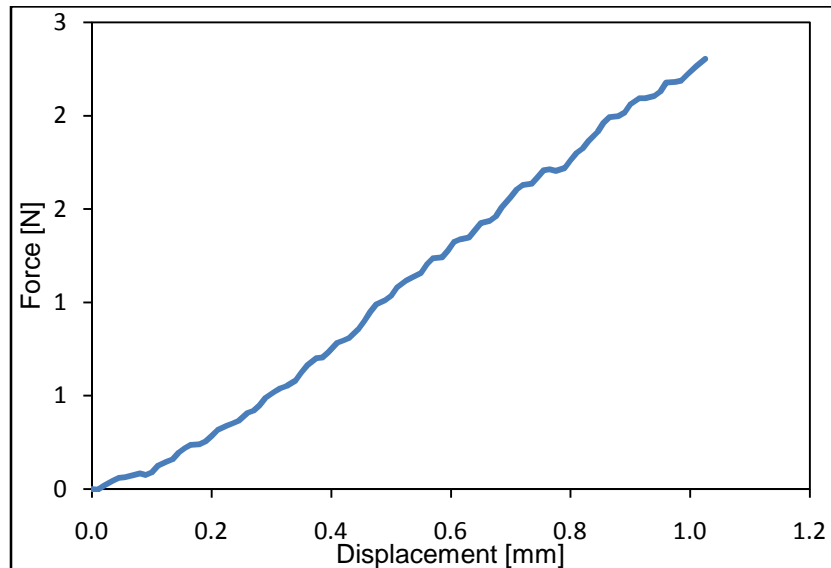
Figure 10 - Typical experimental results from pulling a pedicel from a berry.

Table 4 - Experimental results from pulling the pedicel from the berry.

	Batch 1	Batch 2	Average
Maximum Force [N]	1.1	1.6	1.4
Total Energy [Joule]	7.4E-04	1.3E-03	1.0E-03
Force-Stiffness [N/m]	765	955	860
Energy-Stiffness [N/m]	825	1010	918

The experimental results showed no relation to the physical dimensions of the pedicels or berries. Measurement of the pedicels was very difficult as they don't have a constant diameter, increasing in diameter where it makes contact with the

berry (Figure 11). For the numerical simulations, the maximum force had to be converted to maximum stress, and the stiffness converted to a modulus of elasticity since this is the only way the software accepts the input values. Since there was little relation between the experimental results and the physical dimensions, the diameter of the stems used in the numerical simulation were used to calculate a maximum stress and a modulus of elasticity that would result in an equal maximum breaking force and stiffness.

Figure 11 - Pedicels after being removed from the berries.

3.3.5. Tensile Loading of Stem

In this study the stems were assumed to be a homogeneous and isotropic material in order to keep it compatible with the numerical model used. However, the stems from a grape bunch are not a homogeneous or isotropic material and more research and a special contact model is most likely necessary to simulate the stems accurately.
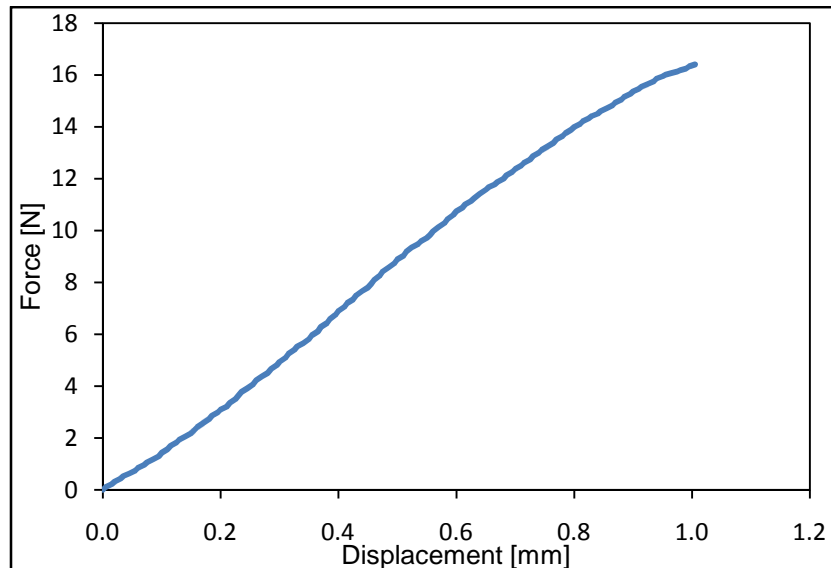
Figure 12 - Typical experimental results from the tensile loading of a stem.

The stems were placed under a tensile force, and the stiffness and failure force were determined (Figure 12). Measurements of the stems were difficult since the stems do not have a uniform diameter. A minimum and maximum diameter was measured and an average diameter was calculated.

The experimental results showed little relation to the physical dimensions of the stems. However, in order to use the results in the numerical simulation, the maximum stress and modulus of elasticity needed to be calculated. The diameter and length of the specimens were used to calculate the modulus of elasticity and maximum stress (Table 5). During the first set of the experiments, the length of the stems was not recorded and the modulus of elasticity could not be calculated.

Table 5 - Experimental results from tensile loading of stems.

	Batch 1	Batch 2	Average
Maximum Stress [MPa]	9.8	13.4	11.6
Modulus of Elasticity [MPa]	-	95	95

3.3.6. Shearing Of Side Stems

A common problem found during the destemming process is that the side stems break off and when the stems are examined, it is clear that these side stems break off in a shearing mode (Figure 13). Due to the experimental layout, it was difficult to place the side stems under a pure shearing force. The side stem and main stem were clamped at a right angle, as shown in Figure 14, and the top chuck was moved upwards, creating a shear force in the side stem where it is attached to the main stem.

Figure 13 - The shearing of side stems as a result of destemming.

Again, little relation could be found between the physical dimensions of the stems and the breaking force or stiffness (Table 6). The measurement of the stems was difficult since a stem does not have a constant diameter and the side stems are wider where it is connected to the main stem. The diameter of the side stems used in the numerical simulation was used to calculate a maximum stress and modulus of elastic that would result in an equal maximum breaking force and stiffness.
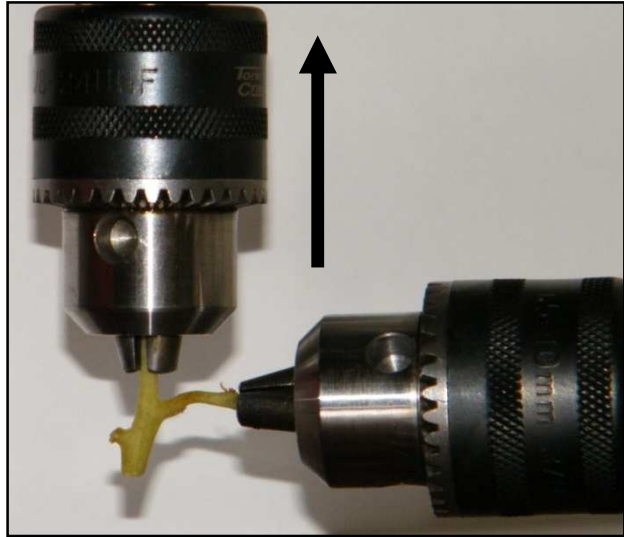
Figure 14 - Shearing of a side stem from the main stem.
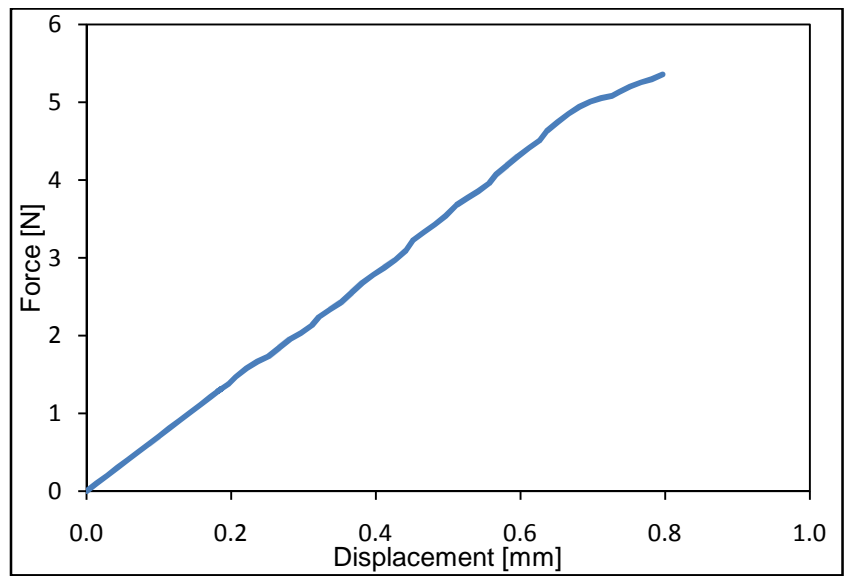
Figure 15 - Typical experimental results from the shearing of a side stem.

Table 6 - Experimental results from shearing off the side stems.

	Batch 1	Batch 2	Average
Maximum Force [N]	9.8	7.8	8.8
Total Energy [Joule]	9.9E-03	9.0E-03	9.4E-03
Force-Stiffness [N/m]	5300	3700	4500
Energy-Stiffness [N/m]	5200	3700	4500

3.4. Beater Experiment

3.4.1. Experimental Setup

The beater experiment was designed to act as a final calibration method of an entire grape bunch in the numerical model. It was designed to duplicate the

20

impact that a grape bunch would experience in a destemmer and helped to understand the destemming process. During the experiment a grape bunch was hit by a set of beaters, similar to the beaters found in a destemmer. The layout and dimensions of the experiment were based on the specifications of the destemmer used in the destemmer tests, Magitec A5.

A drop test was suggested (Amos, 2009) to evaluate the removal of the berries from the stems instead of the beater tests. The drop test would involve dropping the bunches from various heights and monitoring the removal of the berries from the stems. This was investigated, but one of the biggest problems that was experienced was that the orientation of the bunch could not be controlled. From a preliminary investigation it was found that the orientation of a bunch as it hits the ground has a big influence on the amount of berries that is removed.
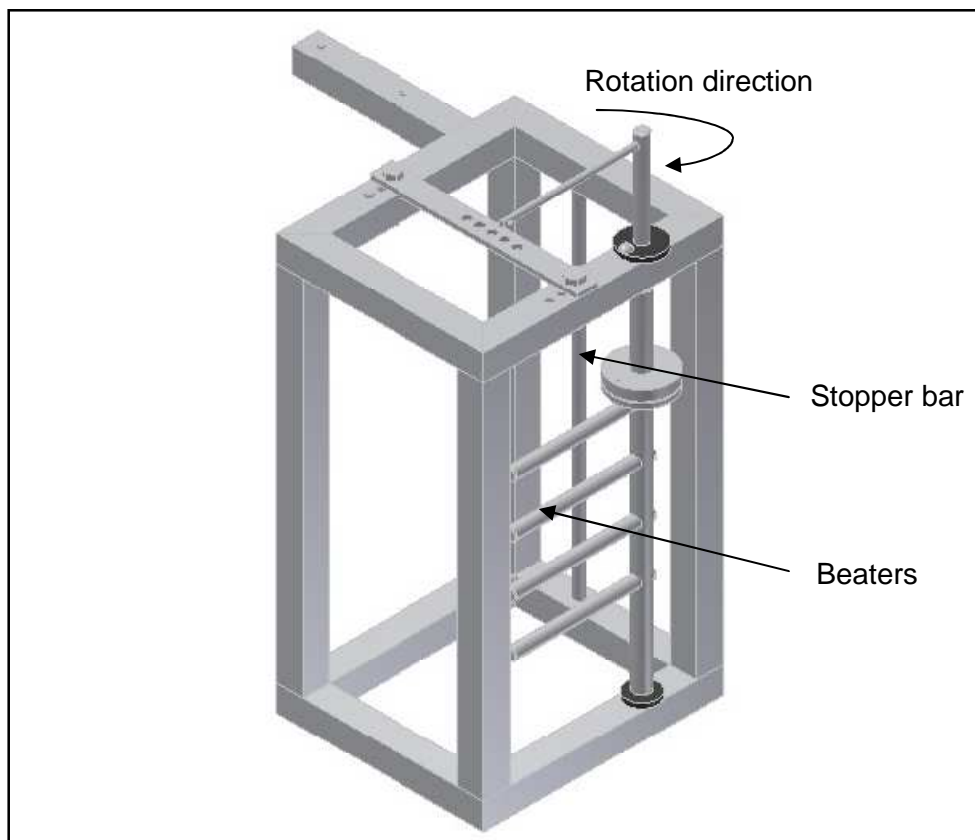
Figure 16 - CAD model of beater experimental setup. Spring not shown.

A CAD layout of the beater experiment is shown in Figure 16. The bunch is held in position by a drill chuck (similar to the one used in the tensile experiments), of which the position is adjustable. The bunch is then hit by a set of four beaters that is mounted on a rotating shaft. This shaft is spring loaded and the speed at which the beaters are rotating can be adjusted by pre-tensioning the torsion spring. The experiment is designed in such a way that the beater tips would achieve similar tip speeds that would be found in a destemmer. A stopper bar

was installed to limit the rotation of the beaters and it was later found that this stopper bar had a profound influence on the removal of the berries from the stems. The rotating shaft was lengthened at the top and an extra bar (sensor bar) was mounted above the grape bunch. A displacement sensor was attached to the sensor bar and was used to measure the displacement of the beaters which was later used to calculate the rotation speed of the shaft.

A high speed camera was used to capture the grape bunch during each experiment and these photos were ideal for visual comparison with the numerical simulation results (Figure 17). These photos also improve the understanding of the destemming process. Photos were captured at 200 frames per second.

3.4.2. Conducting Experiments
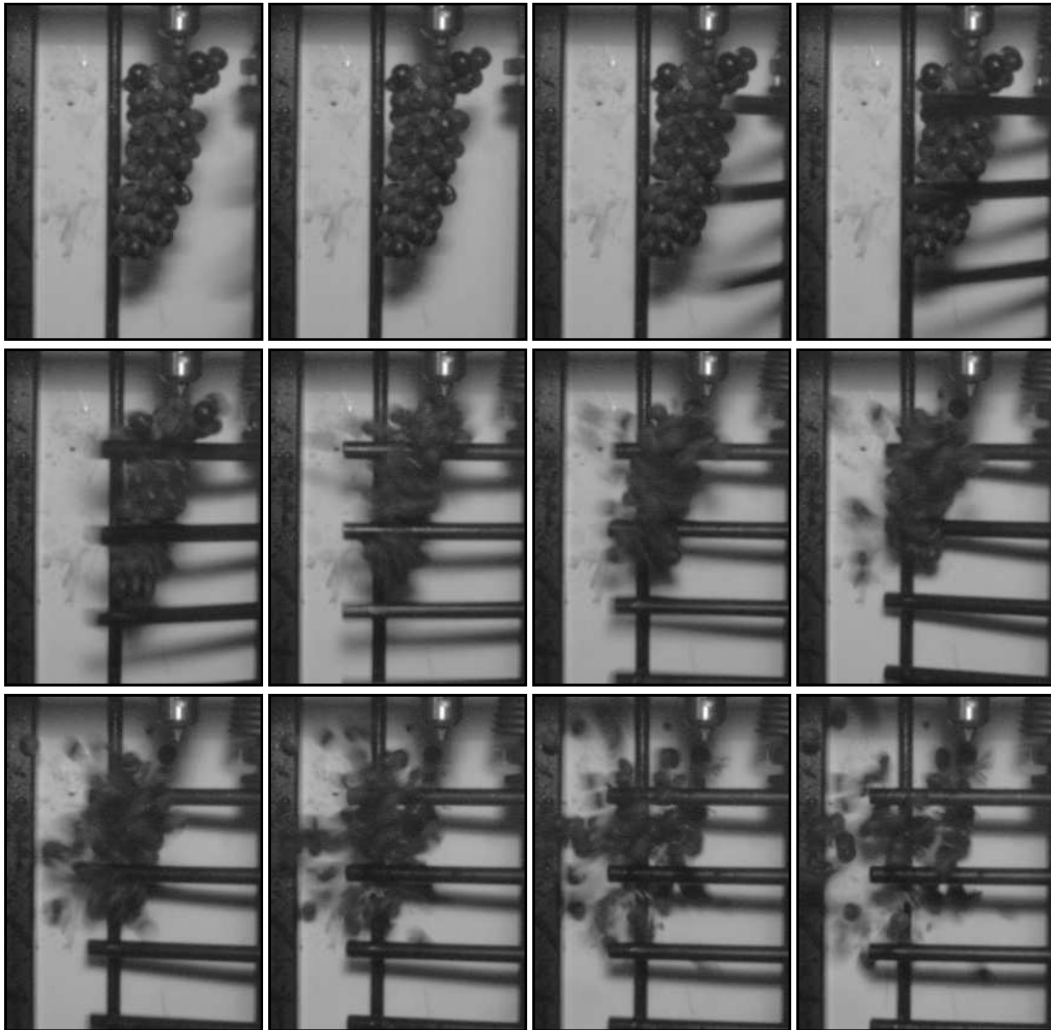
Figure 17 - High speed photos of a bunch being hit by the beaters.

Each bunch was weighed and measured before each test was conducted. After each experiment, the number of berries that were removed was recorded as well

22

as the number of berries still attached to the stem. No stems were broken during the experiments. Photos of each bunch were taken before and after each test.

A total of twenty tests were conducted, ten from each batch of grapes. Figure 17 shows the high speed photos from a typical test. The time interval between the frames was 5/1000 second.

The position of the chuck that held the bunches in position, was not adjusted during the experiments. Some of the bunches had bent peduncles which caused it to hang in a slightly different position. From the photos taken by the high speed camera, it was observed that the stopper bar had an influence on the destemming process. As the bunches hit the stopper bar, a large number of berries were removed. However, due to the variation in position of the bunches, not all bunches hit the stopper bar in exactly the same position and this could result in an increase in the scatter of the data. Replacing the stopper bar with a solid wall could produce better results. However, the experimental setup was designed to have no walls in order to capture the experiment from various angles using the high speed camera.

3.4.3. Results

Since the bunches used in the experiments were not identical, a way had to be found to normalize the results in order to compare the results from bunches of different weight, size and number of berries.

Five graphs were used to evaluate the results from the experiments. The first graph compared the number of berries removed to the weight of the bunch. A reasonable linear trend was found in the data, as shown in Figure 18. However, this comparison ignores the total number of berries and the rotation speed of the beaters. The basic conclusion that can be drawn from the results is that more berries were removed from the heavier bunches. This is as expected since the heavier bunches generally contain more berries.

The second graph that was used compared the percentage of berries removed to the weight of the bunch. This way the total number of berries on each bunch was taken into account and the bunches could be compared more directly. Although the data did not show as definite a trend as in the previous graph, a decrease in the percentage of berries removed can be seen as the weight of the bunch increases (Figure 19). This comparison still ignores the rotation speed at which each bunch was hit.

To take into account the speed of the beater bars at which each bunch was hit, the percentage of berries removed is compared to the rotation speed of the beaters in Figure 20. The data shows a clear linear trend. The results show an increase in the percentage of berries that is removed as the rotation speed of the beaters is increased. This would be expected since the increase in rotation speed of the beaters increases the amount of energy that is transferred to the bunch at

impact and one can expect that this would result in a higher percentage of berries being removed.
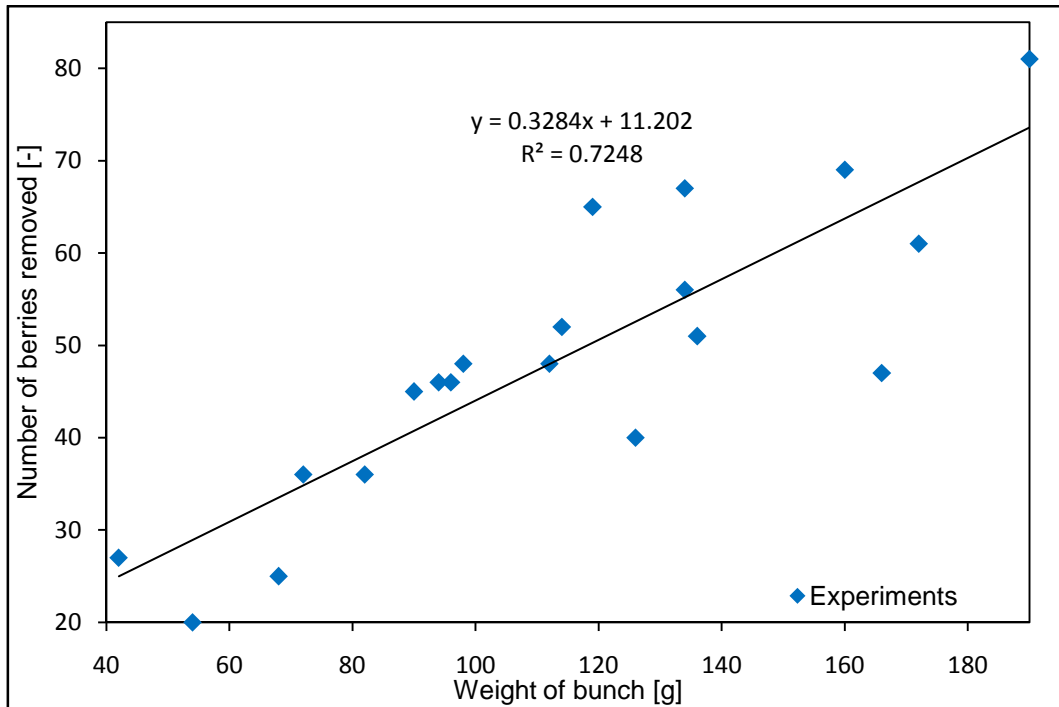
Figure 18 - The number of berries removed versus the weight of the bunches. All rotation speeds.
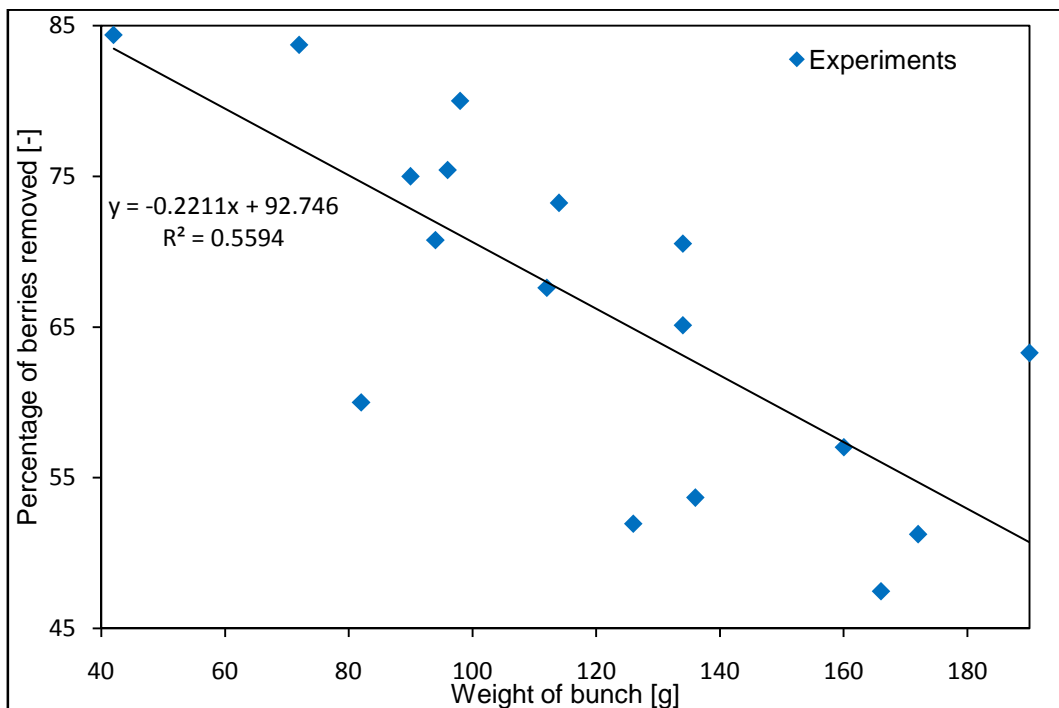
Figure 19 - The percentage of berries removed versus the weight of the bunches. All rotation speeds.

The number of berries removed was also compared to the rotation speed of the beaters but this showed no clear trend and as a result, this comparison was not used for further investigation in this study.
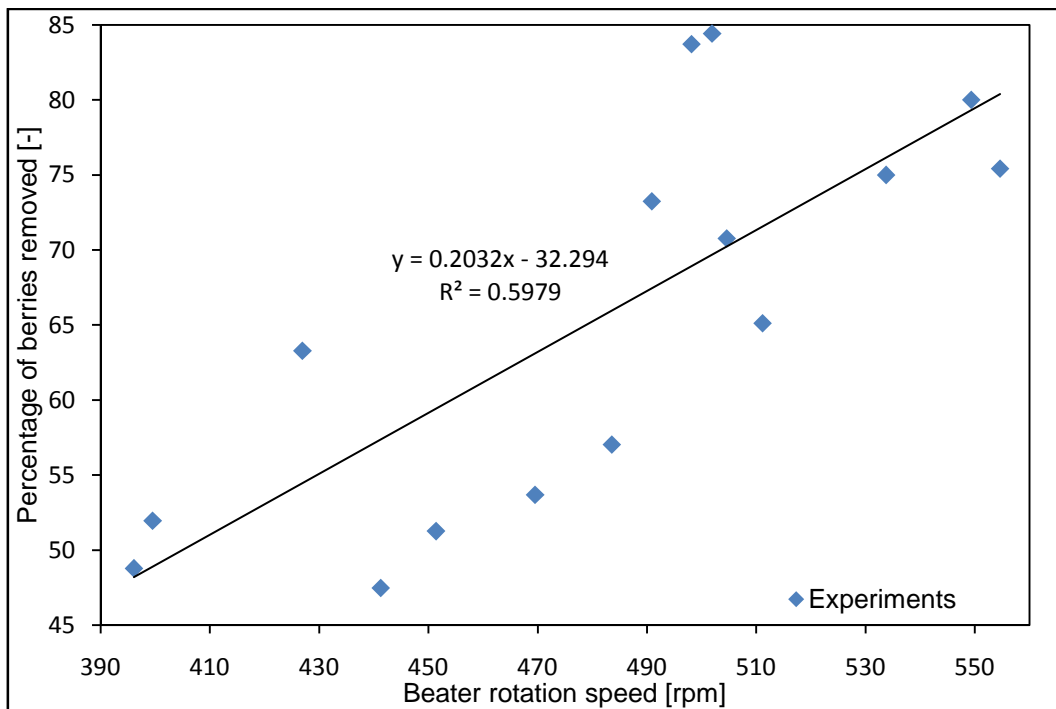
Figure 20 - The percentage of berries removed versus the rotation speed of the beaters.

The three graphs shown above (Figure 18, Figure 19 and Figure 20) take into account the number of berries removed, the percentage of berries removed, the weight of the bunches and the rotation speed of the beaters in some way or another. From the graphs it is clear that the rotation speed and the bunch weight have an influence on the destemming process. In order to include both parameters, the number of berries removed and the percentage of berries removed were each divided by the weight of the bunch and then compared to the rotation speed of the beaters. The number and percentage of berries removed were divided by the weight to normalise the bunches in terms of weight. One would expect that the total number of berries per bunch is closely related to the weight of the bunch and that it is not necessary to incorporate the weight as well as the total number of berries (i.e. percentage of berries removed). In Section 3.7.4. the relation between the total number of berries and the weight of a bunch is discussed and from the experimental data it is clear that there is indeed a correlation between the number of berries and the weight of a bunch. However, it is still important to include the weight of the bunch, as can be seen when comparing Figure 20 and Figure 21. Both these graphs compare the percentage of berries removed to the rotation speed of the beaters, but in Figure 21 the percentage of berries removed are divided by the weight. There is a clear

resemblance between the data scatter in the two graphs, but Figure 21 shows a better correlation coefficient (R^2).
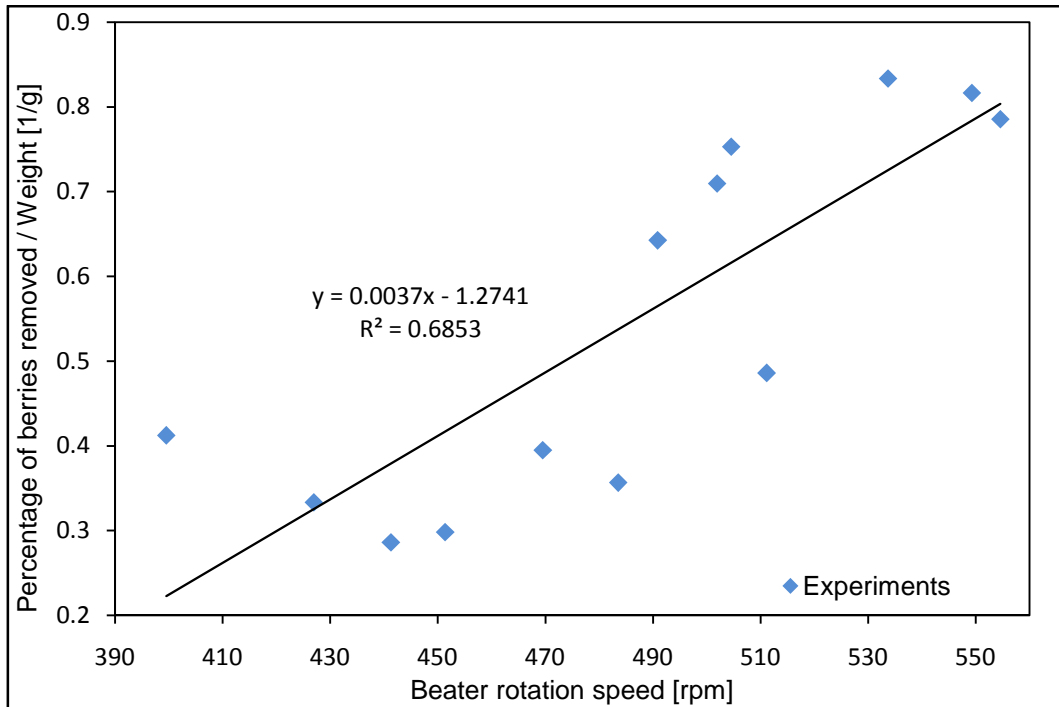
Figure 21 - The percentage of berries removed, divided by the weight, versus the rotation speed of the beaters.
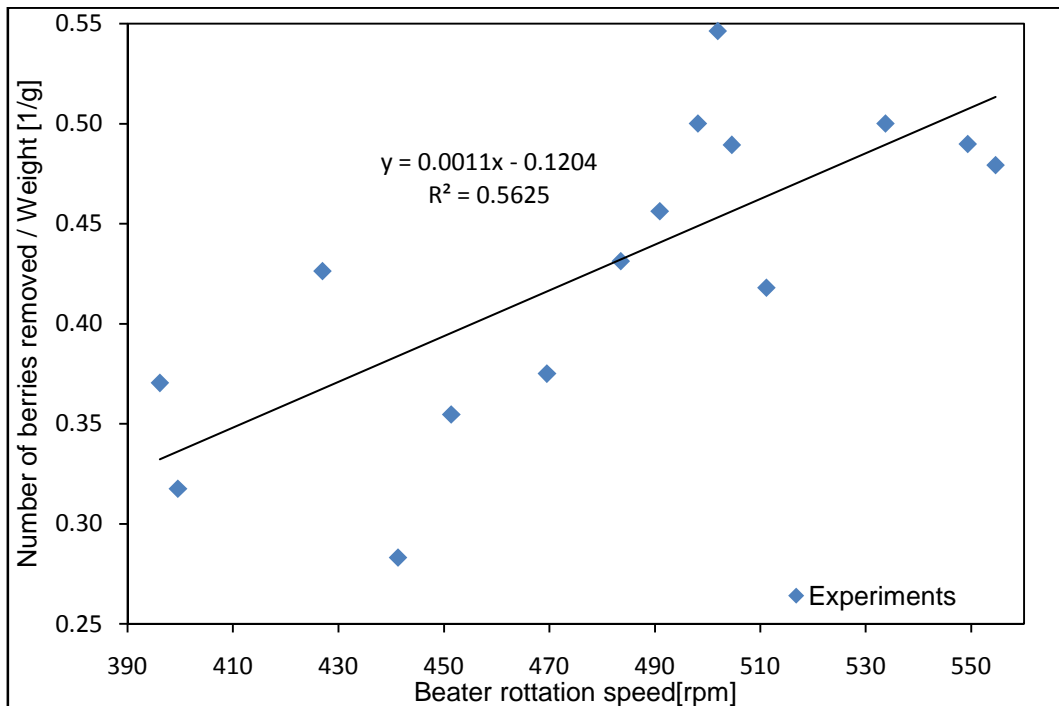
Figure 22 - The number of berries removed, divided by the weight, versus the rotation speed of the beaters.

26

The weight is also of high importance when comparing the number of berries removed to the rotation speed of the beaters (Figure 22). When only the number of berries removed was compared to the rotation speed of the beaters, no definite trend could be found in the data, but when comparing the number of berries, divided by the weight of each bunch, to the rotation speed of the beaters, a clear trend can be found (Figure 22). Also see Figure 62 for a contour plot of the experimental results.

3.5. Destemmer Tests

The main objective of this study was to investigate the possibility of using DEM to simulate the destemming of grape bunches. As a case study, tests were done using a Magitec A5 destemming machine (Figure 4) to determine the performance of the machine and evaluate the results to the DEM simulation.
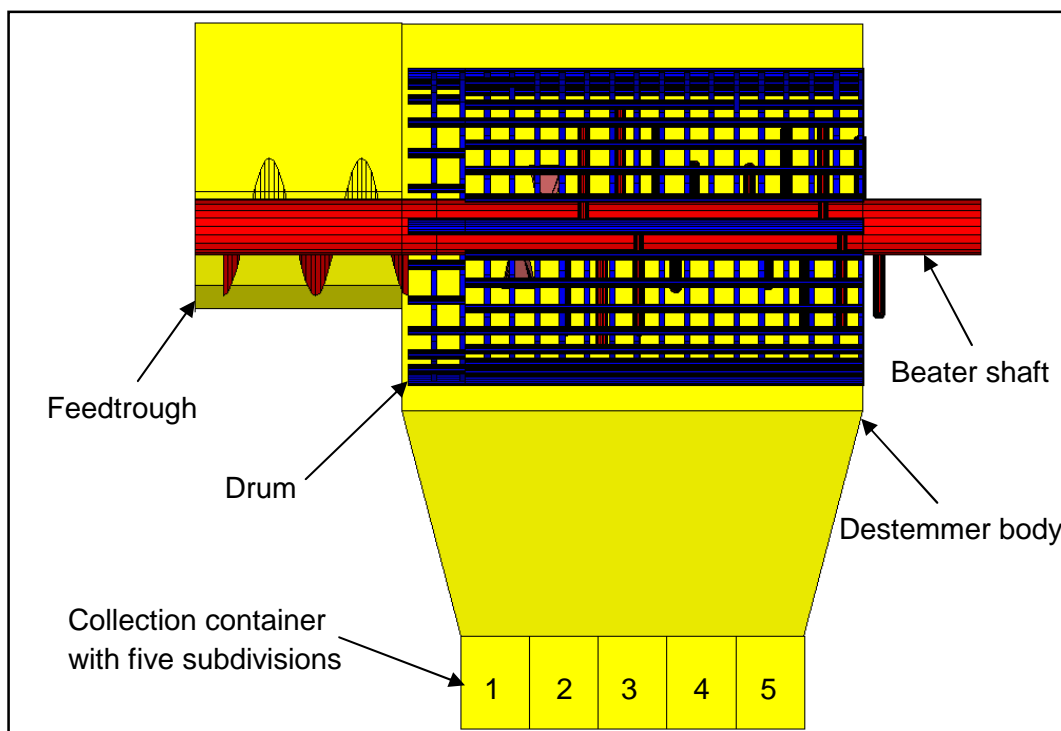
Figure 23 - The basic layout of the destemmer shown in DEM. The feedtrough, beater shaft (red), drum (blue), destemmer body and the collection container with its five subdivisions are shown.

The performance of the machine was tested by monitoring the berries and the stems exiting the machine. A container with five subdivisions was used to determine the number of berries exiting from each part of the machine. The first subdivision started at the berry exit at the side of the machine where the grape bunches enters the machine (labelled 1 in Figure 23, Figure 25 and Figure 26) and the last subdivision ended where the stems exit the machine (labelled 5 in Figure 23, Figure 25 and Figure 26). The berries in each subdivision were weighed and the amount of impurities present in each subdivision was recorded.

27

Impurities that were recorded included stems, leaves and green berries (Figure 24).
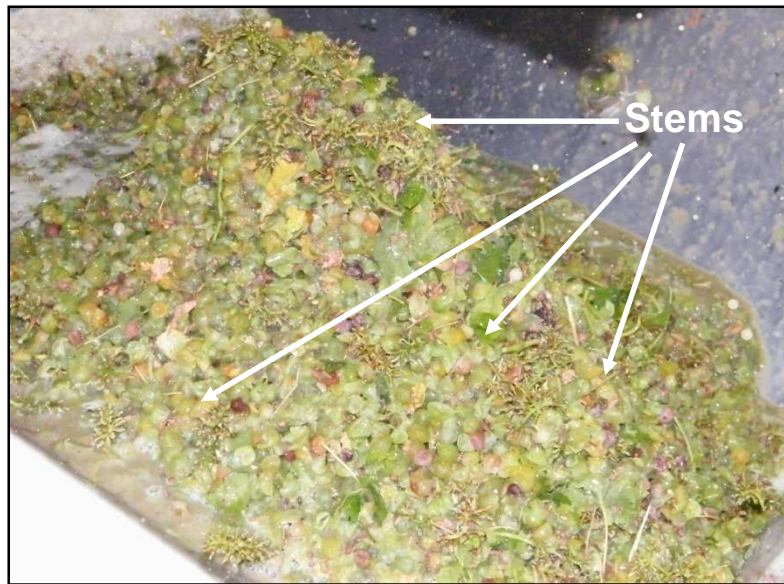
Figure 24 - Broken stems with grapes after destemming.

The stems exiting from the machine were also collected, weighed and counted. The number of berries still connected to the stems was recorded as well as the number of loose berries that exited with the stems. During the test, the rotation speed of the destemmer was recorded as well as the time duration that the grapes were fed into the machine in order to determine the feed rate.

Four different speed setting were used and tests were repeated to verify the repeatability. However, since the grapes were fed by hand, it was very difficult to control the feed rate accurately and, as a result, it was very difficult to create identical conditions for each test. Since the technical data of the machine is confidential, the actual rotation speeds of the destemmer are not listed in this report. Instead, the four speed settings are represented as the setting on the machine namely, setting 4, 6, 8 and 10, in order from slowest to fastest. The drum and beater shaft of the machine rotates in opposite directions at a fixed ratio. From Figure 25 one can see that the majority of the grapes exit the machine in the first subdivision, which is where the grapes enter the machine. As the speed increase, so does the concentration of berries in this region. As the speed decreases, a slightly more equal distribution can be seen across the discharge region of the machine.
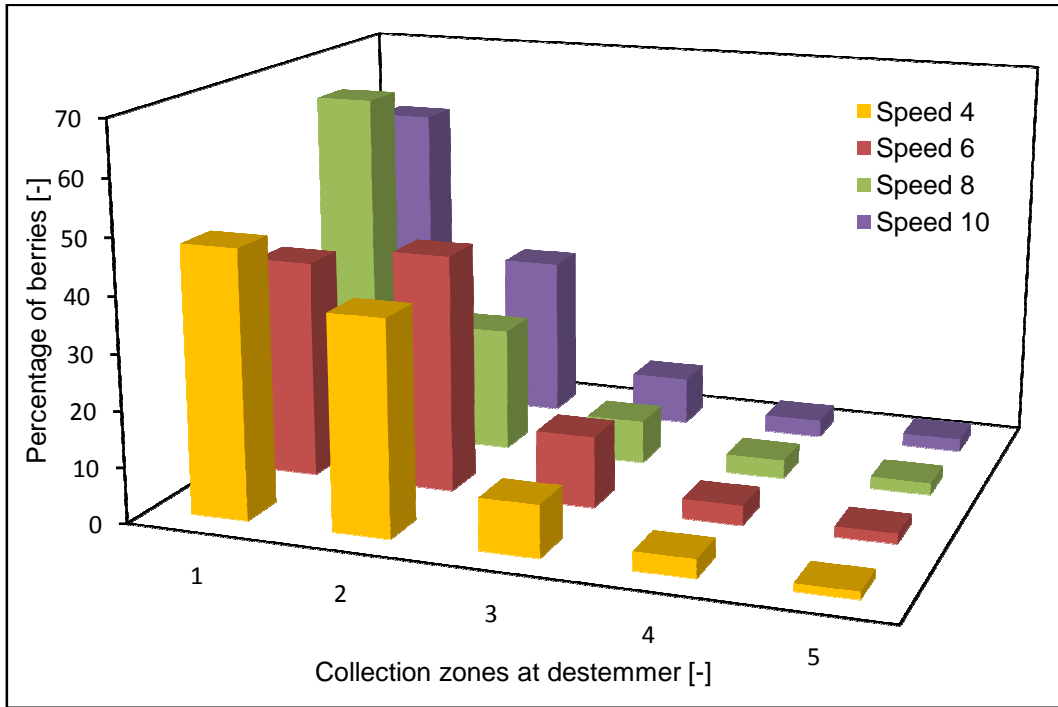
Figure 25 - Berry discharge in each subdivision from the destemmer at four different speed settings. Note: Speed setting 4 is the slowest and setting 10 is the fastest rotation speed.
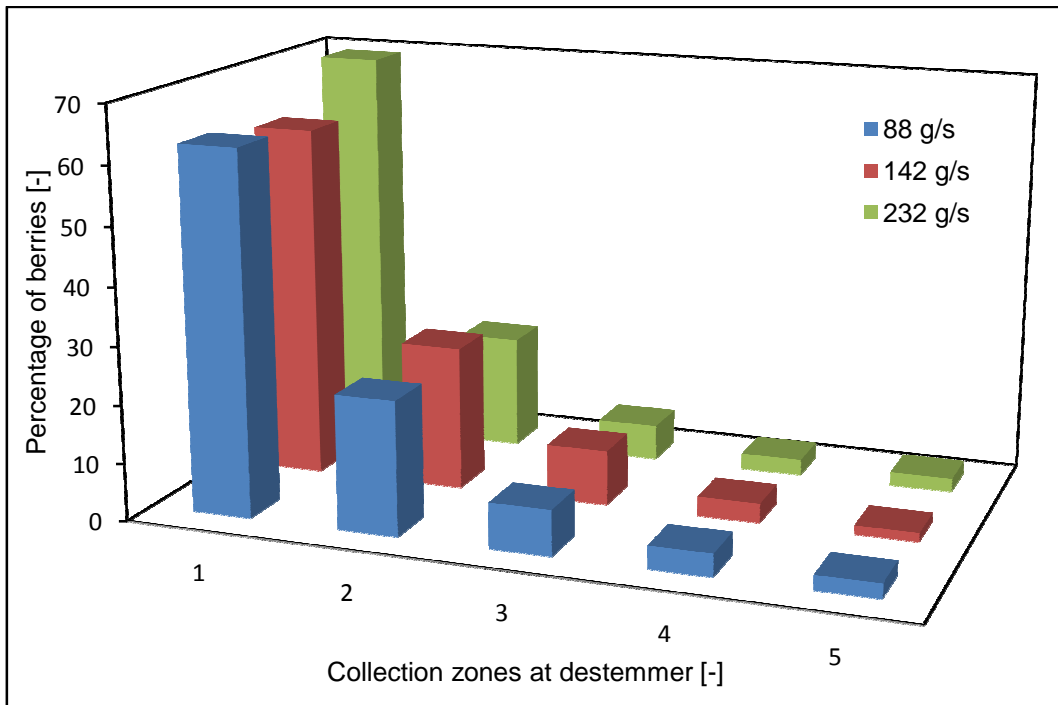
Figure 26 - Berry discharge in each subdivision from the destemmer at three different feed rates.

The feed rate was determined by the time duration that the grapes were fed into the destemmer and the total weight of the grapes and stems collected at the

29

discharge of the machine. Three feed rates were recorded at a speed setting of 8 and are shown in Figure 26. There is very little variation in the results but there is a trend that at the lower feed rates, the distribution of the berries from the discharge is slightly more evenly spread and at higher feed rates, the berry distribution is more concentrated at the first segment. Since the grapes are sorted by hand after destemming, lower feed rates were used and the feed rates recorded during the tests were much lower that the designed feed rate of the machine. The maximum feed rate recorded during the tests was 230 g/s while the designed maximum feed rate of the machine is 1400 g/s. However, the machined operated and performed well under these feeding conditions.

The total number of berries that exit at the stem discharge were normalised by dividing it by the number of bunches. This gave an indication of the number of berries per bunch that ended up with the stems. This was then compared to the speed and feed rate respectively and is shown in Figure 27 and Figure 28.
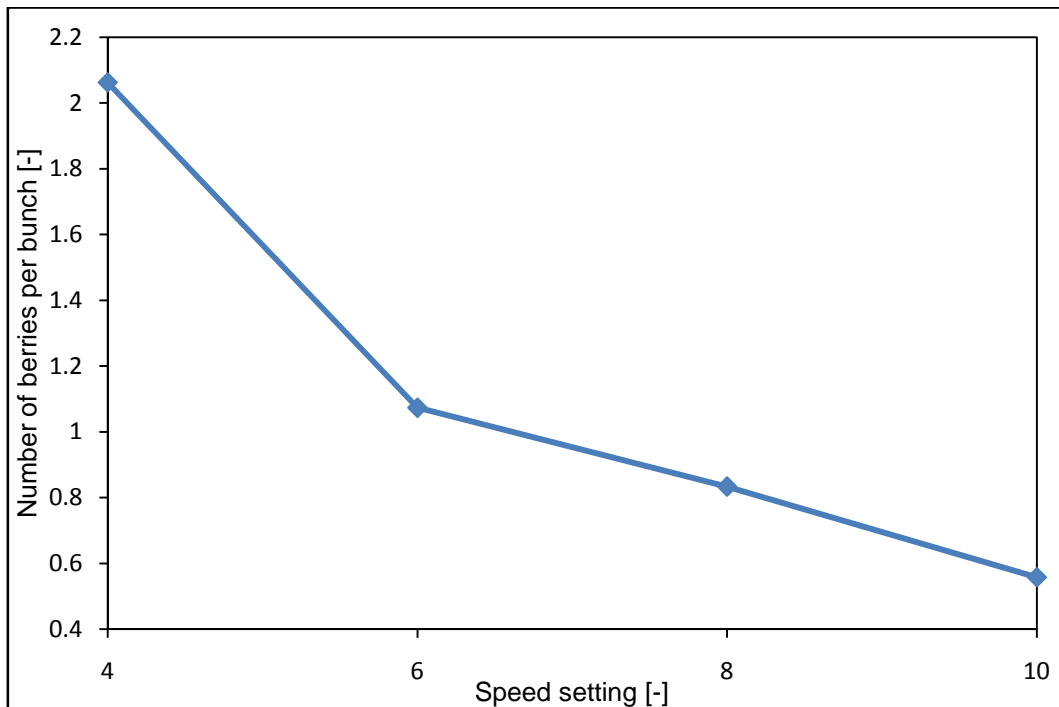
Figure 27 - The number of berries with the stems compared to the speed setting of the destemmer.

Figure 27 shows a sharp decrease in the number of berries as the speed increased. Nearly two berries per bunch exited with the stems at the lowest speed setting. In Figure 28, a decrease in the number of berries can be seen as the feed rate increased. In literature it was mentioned that destemmers perform best when operating at their designed feed rate (Phillips, 2005). The results in Figure 28 confirm this since the number of berries lost with the stems decreases as the feed rate was increased towards the designed feed rate of the destemming machine.
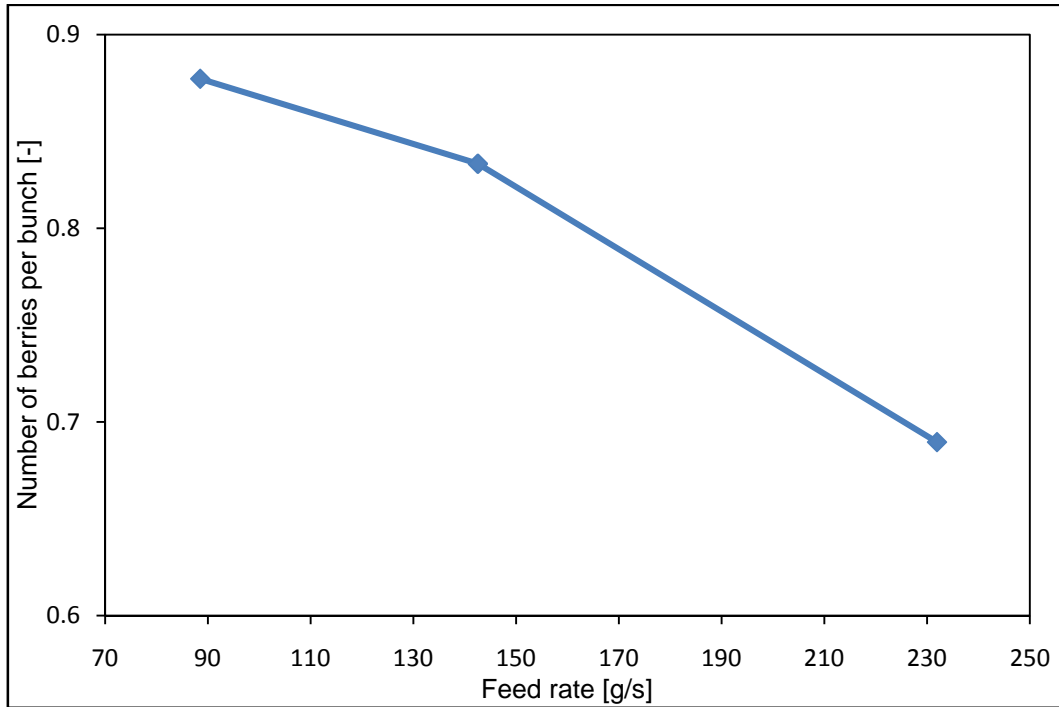
Figure 28 - The number of berries with the stems compared to the feed rate.

3.6. Grape Bunch Shape and Dimensions

The data gathered during the experiments regarding berry size, stem diameter, pedicel length, bunch size, weight of bunch and number of berries per bunch were used to determine average values and to determine if any trends were present in the data.

3.6.1. Berry Size

Two parameters regarding the berry size were recorded. In the density tests, the volume of a specific number of berries was measured and this was used to calculate the average diameter of each berry (also see Section 3.2.). During the berry compression tests and pulling the pedicels from the berries, the diameters of the berries were measured. Since the berries were slightly oval shaped, two diameters were measured, one along the length of the berry (average of 15 mm) and another across the equator of the berry (average of 12.5 mm).

To determine whether the berries are best described by an ellipsoid or a sphere, the volume of the berries was first calculated using the two measured diameters and the formula for the volume of an ellipsoid. The average of the two diameters was then taken and the volume was calculated using the formula for the volume of a sphere. In Table 7 the results are shown and it is clear that the berries' volume is best described by a sphere. Therefore, the average of the two measured diameters was used to represent the diameter of each berry.

31

Table 7 - Average volume of a grape berry.

	Measured	Ellipsoid	Sphere
Volume [ml]	1.33	1.46	1.36

A histogram of these average diameters was drawn up and a normal distribution was applied to the data. As shown in Figure 29, the data fits a normal distribution very well and an average berry diameter of 13.5 mm was calculated. Since the numerical simulation can only simulate spherical particles, this average diameter was used as the berry size in the numerical simulation.
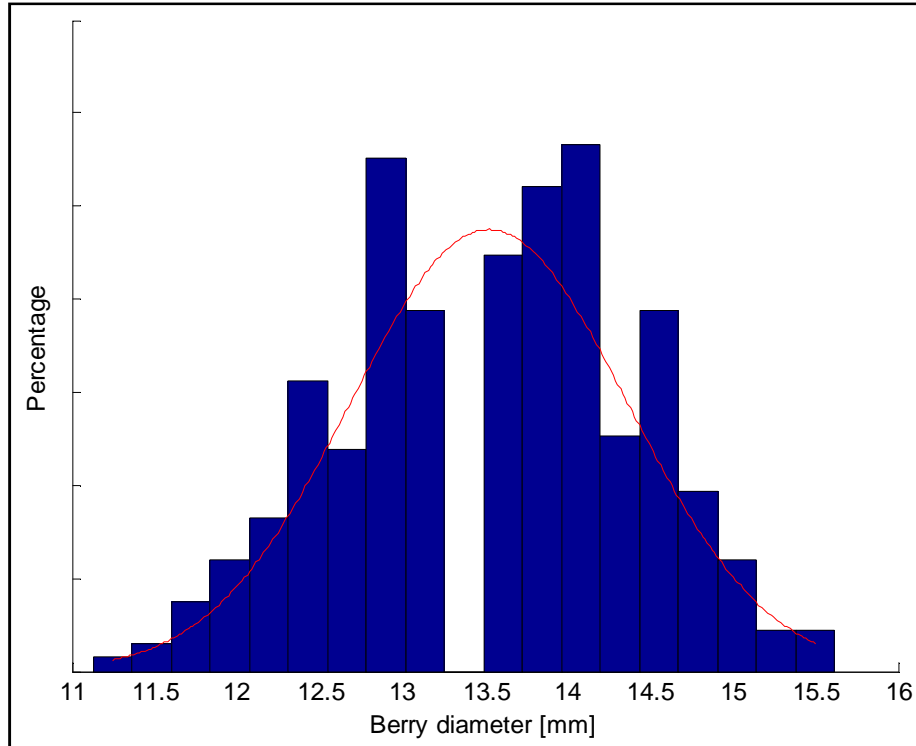
Figure 29 - Histogram and normal distribution of berry diameters.

3.6.2. Pedicel Dimensions

The length of the pedicels was recorded during the tests when they were pulled from the berries. The average length of the pedicels helped to improve the accuracy of the bunch shape when building a bunch in the numerical simulation. The data recorded was used to create a histogram and a normal distribution fitted the data reasonably well (Figure 30a). The average pedicel length was calculated as 6.7 mm.

As mentioned in Section 3.3.4, the diameter of the pedicel was very difficult to measure since it does not have a constant diameter. The minimum diameter was measured and this data was used to determine an average pedicel diameter. A histogram, with a normal distribution fitted to the data, is shown in Figure 30b and the average pedicel diameter used was 1 mm.

(a)   (b)
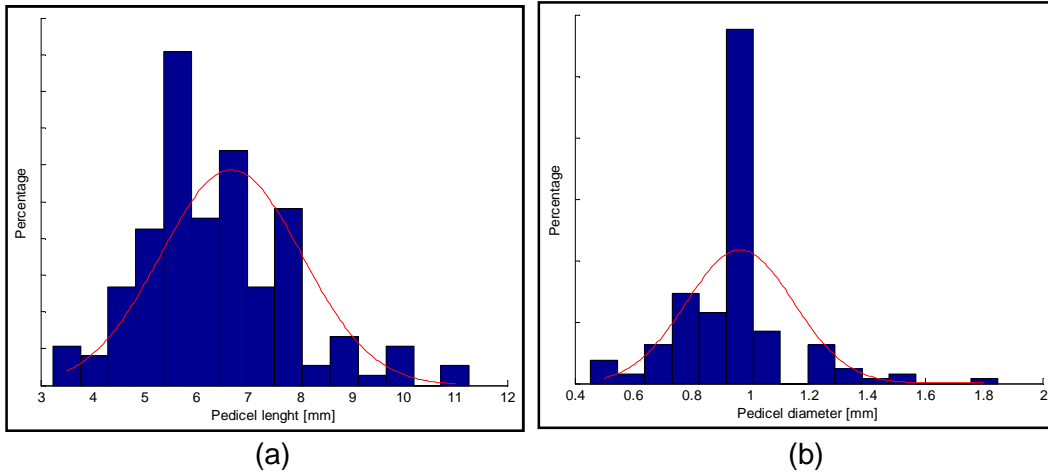
Figure 30 - The histogram with a normal distribution of (a) the pedicel length and (b) the pedicel diameter.

3.6.3. Stem Diameter

The diameters of the main and side stems recorded during the tensile loading of the main stems and the shearing of the side stems were used to determine the average main and side stem diameters. Histograms, with normal distributions fitted to the data, can be seen in Figure 31a and b. The average main stem diameter was calculated as 2 mm and the average side stem diameter also as 2 mm. As mentioned in Section 3.3.6., the measurement of the side stems was very difficult since it did not have a constant diameter. The side stems were measured where they connected to the main stem and this explains why the average diameters of the main and side stems are equal.

(a)   (b)
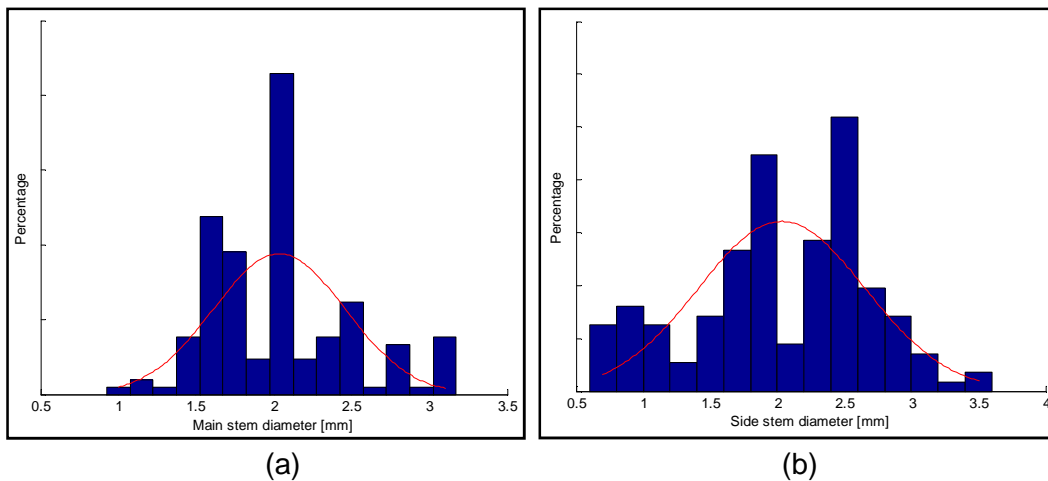
Figure 31 - Histogram and with a normal distribution of (a) the main stem and (b) side stem diameter.

3.6.4. Bunch Overall Dimensions

The weight, length and number of berries of each bunch, recorded during the beater and vibration experiments, were used to compare the weight of the bunch

33

to the number of berries and the length of the bunch. The averages of the number of berries and weight of a bunch were also calculated.

When comparing the number of berries to the weight of the bunch, one would expect a linear relation since the berries represent most of the bunch's weight. In Figure 32 it is clear that there is indeed a close relation. The small deviation that can be seen in the data can be related to the variation in stem lengths and berry diameter which results in a variation in weight.

In the comparison of the length of the bunches to the weight, there was a larger deviation in the data (Figure 33). This can be contributed to how compact the berries were packed in a bunch as well as the size of the shoulders of a bunch. If the berries were packed very tightly in a bunch, it would usually be heavier than a bunch of similar length with berries that were more loosely packed. The same goes for bunches with large shoulders. These bunches had a significant larger weight than a bunch of similar length but with no shoulder (Figure 5). However, a clear trend could still be found in the data. From Figure 34 it can be seen that the average bunch weight was 100 grams and the average number of berries per bunch was 67 berries.
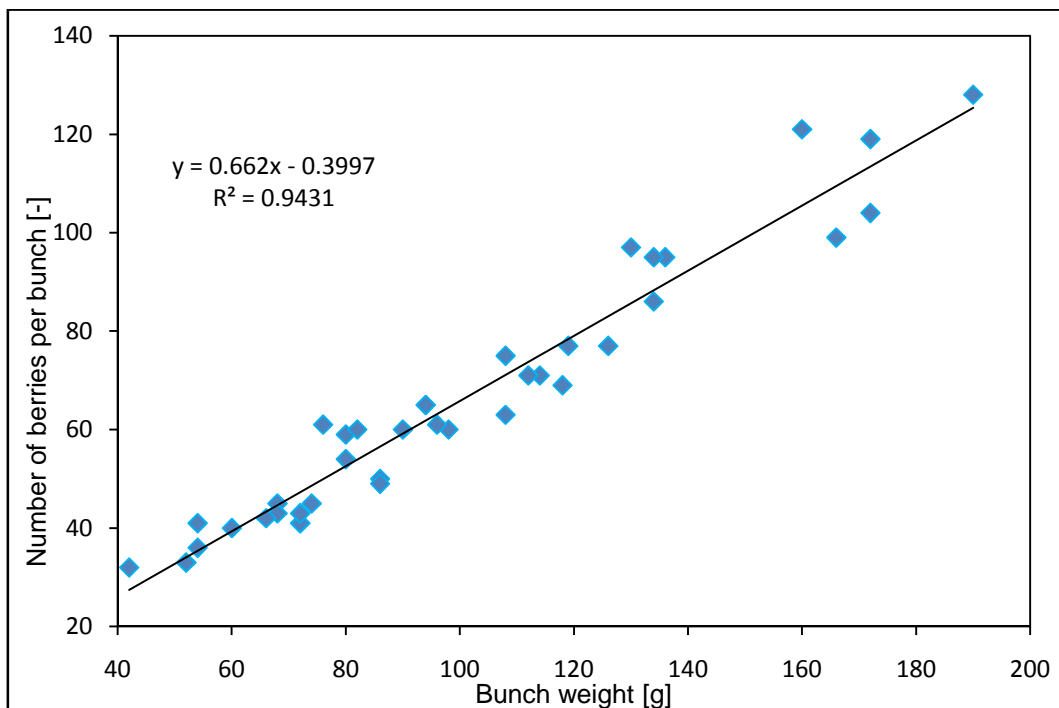
Figure 32 - The number of berries per bunch compared to the weight.

34
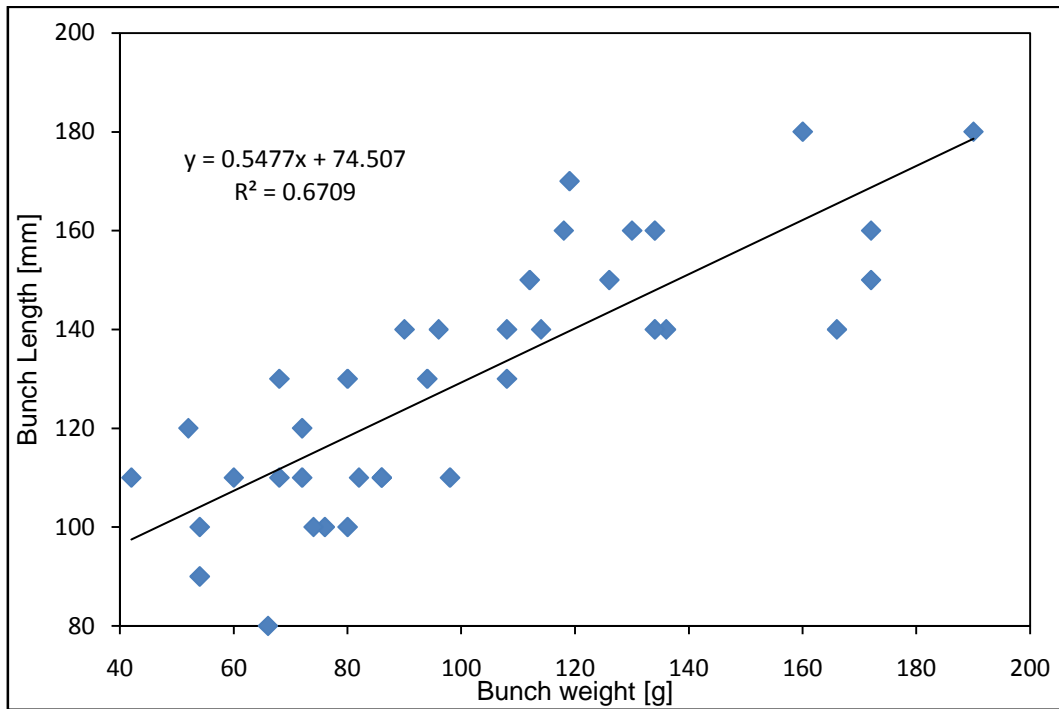
Figure 33 - The length of each bunch compared to the weight.

(a)   (b)
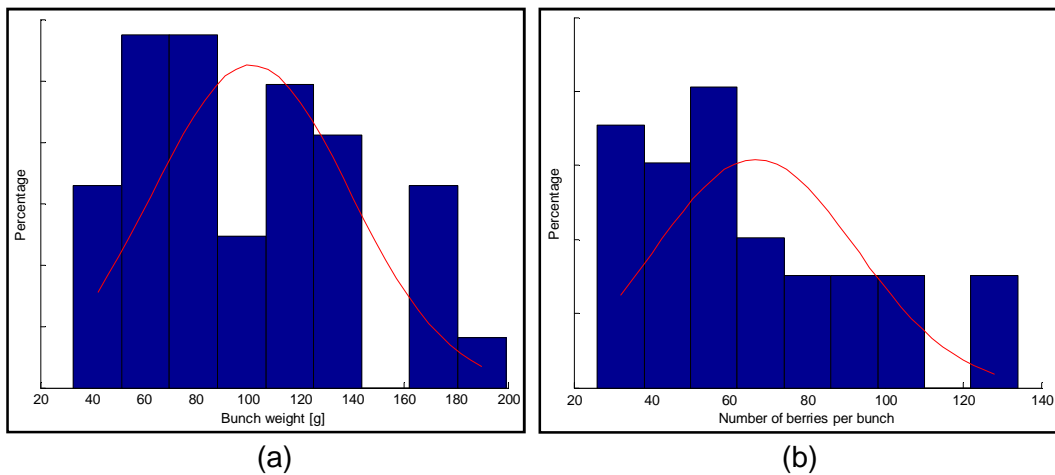
Figure 34 - The histograms, with normal distributions fitted to the data, of (a) the bunch weight and (b) the number of berries per bunch.

3.7. Conclusions

A large scatter in the experimental results was expected, but the results showed reasonable trends that can be used as input parameters to the DEM bunch model. The experimental results can also be used to validate the DEM modelling of the destemming process.

The experiments for determining the material properties of the grape bunches gave good results that are statistically sound and that can be useful in the development and design of destemmers. It is recommended that in future studies

35

a wider speed range is used that involves higher speeds. The failure mechanism involved in the shearing of the side stems should also be further investigated and the experimental procedures adapted accordingly. Since no similar research could be found, the stiffness was calculated in two different ways: force based stiffness and energy based stiffness. It was found that in the experiments that followed a linear relation between the displacement and reaction force, there was only a small difference between the force- and energy based stiffness's. The amount of energy required to reach failure point could also be valuable when designing a destemmer. The failure forces and stiffnesses obtained in the experiments can be used in the DEM model as initial values.

The beater experiment gave good insight into the behaviour of the grape bunch under destemming condition through the photos taken by the high speed camera. Valuable data was collected regarding the relation between the number of berries removed from the bunch, the weight of the bunch and the rotation speed of the beaters. It was found that the data fitted a bi-linear plot very well. This data can be of great value during the design of destemmers. Since a good trend could be found regarding the removal of the berries, it could be of great benefit to conduct experiments using higher beater speeds to investigate stem breakage. It is recommended that the stopper bar is replaced by a solid wall to eliminate the effect it had on the grape bunches. The data collected from these experiments can be used to calibrate the DEM model.

No official method could be found for measuring the performance of a detemmer. An experimental setup was designed to test the performance of a commercial destemmer by monitoring the berries at the berry discharge and the stems at the stem discharge. The trends found in the results showed good correlation to the information that was available from literature. It is recommended that a more accurate way of feeding the grapes are used in future experiments and that larger samples are used. This way, stem breakage could be investigated more accurately. The data gathered during the experiments can be used to evaluate the performance and accuracy of the DEM model.

4. DEM Simulations

4.1. Introduction

In the numerical simulations, grape bunches are build from spherical particles and are simulated using the discrete element method (DEM). Using parallel bonds, spheres are bonded together in order to form stems and berries. The stiffnesses and breaking forces between the spheres are specified and the complete bunch is simulated under a series of events that simulate the experiments that were done. The stiffnesses and breaking forces that were obtained from the experiments were all sets of statistical data, but only the averages were used in the numerical simulation. The results from the simulations are compared to the experimental results and adjustments are made to the specified material properties to improve the correlation between the simulations and the experimental results.

4.2. Building a Grape Bunch using DEM

A grape bunch is made up from stems and berries. The stems can be subdivided into main stems, side stems and pedicels. In the numerical simulation the bunch is created by first building the main stem, then the side stems, which are attached to the main stem, and finally the pedicels and berries (Figure 35). The pedicels are built in groups of up to four pedicels with berries. These groups are attached to the main or side stems.
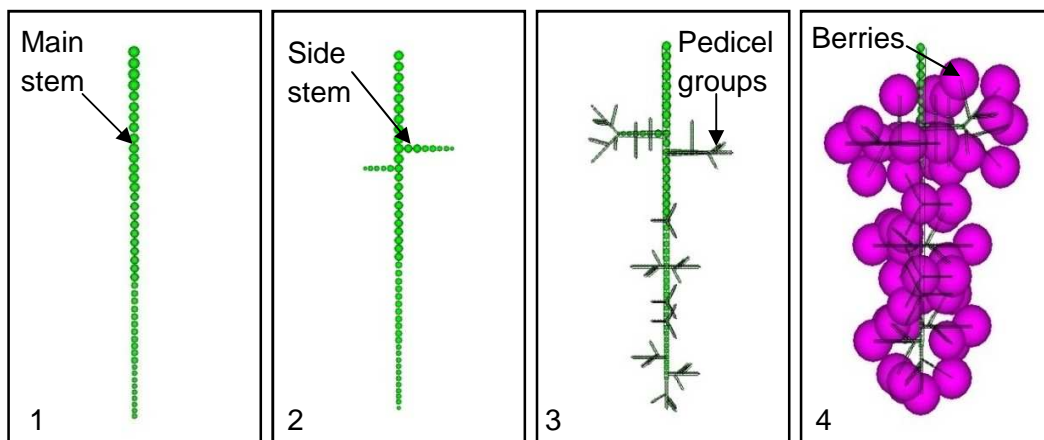
Figure 35 - The four steps in building a grape bunch in DEM.

4.2.1. Building a Single Stem

A stem is build using spherical particles, called balls, which are bonded together using parallel bonds (*Appendix A*). The start co-ordinate and length (*L*), or end co-ordinate, are specified as well as the start (d_s) and end diameter (d_e) of the stem. The stem diameter is assumed to vary linearly along the length (Figure 36) of the stem and the number of balls (*N*) needed to create the specified stem is calculated in equation 1.

$$N = \frac{2*L}{d_s + d_e} \tag{1}$$

Since the value calculated in equation 1 is not always an integer, the number of balls needed to build the stem (*N*) is rounded down to the nearest integer. As a result, the actual length of the stems is not always exactly the same as the specified length. The diameter (d_n) and position (x_n) of each ball in the stem is then calculated as shown in equations 2 and 3 respectively.

$$d_n = d_s - (d_s - d_e)\frac{n}{N-1} \qquad \text{for n = 1, 2, 3,...., N} \tag{2}$$

$$x_n = x_{n-1} + \frac{1}{2}(d_n + d_{n-1}) \tag{3}$$
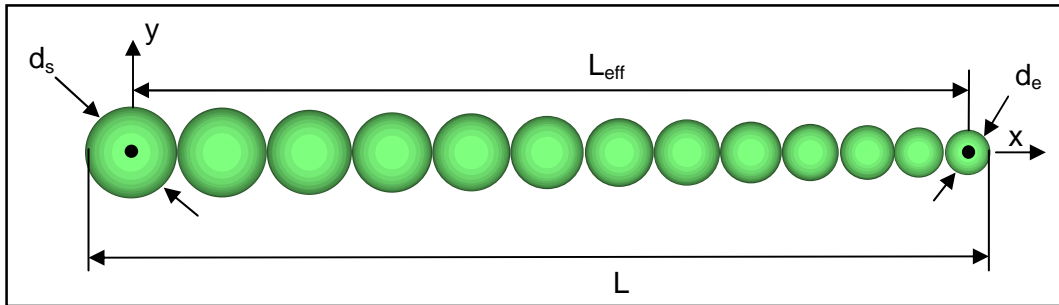
Figure 36 - An example of a tapered stem.

The parallel bonding method used in the simulations, requires the stiffness of the balls and the stiffness of the bond between the balls to be specified. In the simulation of a stem, the stiffness of the bonds will determine the stiffness of the stem under axial tensile loading, bending and torsion. Under these loading conditions, the stiffness of the balls will have no influence on the stiffness of the stem since the balls don't overlap (*Appendix A*). The stiffness of a stem under axial tension is calculated in equation 4 where *A* is the bond area calculated as described in Section A.3.3., k_n^{bond} [Pa/m] is the stiffness of the bonds and $k_n^{stem-bond}$ [N/m] is the stiffness of the stem.

$$k_n^{stem-bond} = \frac{A*k_n^{bond}}{(N-1)} \tag{4}$$

When the stem is under axial compression, the balls overlap and make contact. The stiffness of the balls will have an influence on the overall stiffness of the stem (equation 5) since the stiffness of the bonds and the stiffness of the balls are used to determine the overall stiffness of the stem. These two stiffnesses work in parallel and the resultant stem stiffness is calculated in equation 6.

$$k_n^{stem-contact} = \frac{k_n^{ball}}{2*(N-1)} \tag{5}$$

$$k_n^{stem} = k_n^{stem-contact} + k_n^{stem-bond} \tag{6}$$

The axial stiffness and strength measured in the experiments are used to calculate the stiffness and strength of the bonds in the numerical simulation. The stiffness of the stem as a result of the stiffness of the parallel bonds (equation 4) is compared to a uniform round bar using theory of elasticity in equation 7, where *A* is the cross sectional area, *E* the modulus of elasticity, and L_{eff} the effective length of the bar. The stiffness of the bond is then derived from equation 7 and shown in equation 8.

$$k_n^{stem-bond} = \frac{A*k_n^{bond}}{(N-1)} = \frac{A*E}{L_{eff}} \tag{7}$$

$$k_n^{bond} = \frac{E*(N-1)}{L_{eff}} \tag{8}$$

The stiffness of the balls used in the simulation was half the stiffness of the bonds. It was found that the simulation became unstable when a lower stiffness value was used for the balls.

The breaking strength of the stems in the simulation was set equal to the measured values from the experiments (Section 3.3.5.) and tested in the simulation. The stems were also simulated under axial loading (tension), bending, and torsion and the results showed good correlation under small deflections to the calculated results using beam theory.

The main and side stems were built by specifying the start and end co-ordinates of each stem, as well as the start and end diameters. The bonds between the side and main stems had a different breaking strength to the bonds in the stems themselves. The breaking strength was calculated by using the average stem diameter used in the simulation and the breaking force from the experiments to calculate the maximum tension. The breaking strength and stiffness of these bonds were later fine tuned during the simulation of a grape bunch.

4.2.2. Building a Group of Pedicels

Figure 37 - A grape stem. Note the groups of pedicels on the stem.

The basic layout of grape bunches was observed while conducting the experiments as well as during several other visits to vineyards and cellars. From

39

the observations it was clear that the berries are attached to the main and side stems via groups of pedicels that vary from one to four or more pedicels with berries (Figure 37).

In order to simplify the building of the stems in the numerical simulation, groups of up to four pedicels with berries were built. These groups were created by building one main pedicel that was attached to the main or side stem. The position where this main pedicel was attached to the main stem was specified as well as the angle it made with the main stem and the rotation around the main stem. One, two or three pedicels could then be attached to this main pedicel and the positions where they were attached to the main stem, their angle with the main pedicel and the rotation around the main pedicel were specified. The length, start and end diameter of each pedicel were also specified. Figure 38 shows a group of four pedicels with berries.
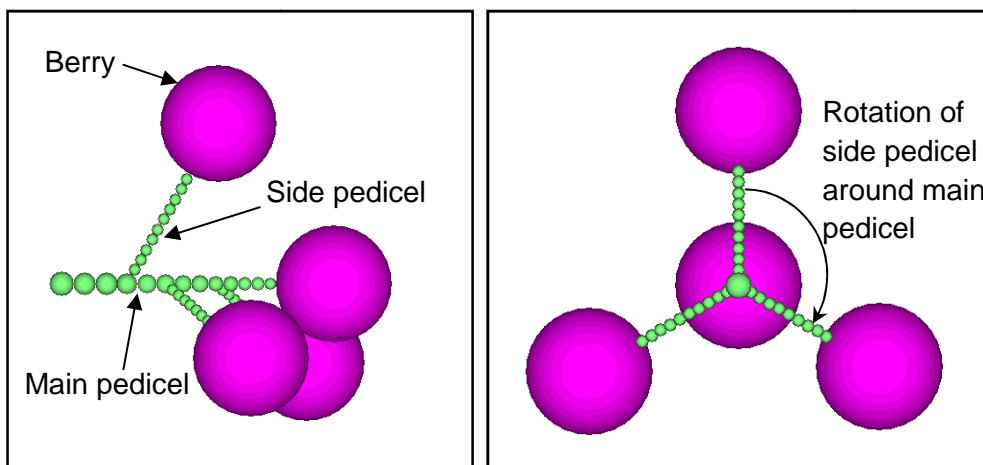
Figure 38 - An example of a group of four pedicels and berries in the numerical simulation.

The measurement of the pedicel diameter was very difficult since they did not have a constant diameter (Section 3.3.6.). The average minimum diameter of the pedicels measured during the experiments (1 mm) was used in the simulation and a constant diameter was used. The average length of the pedicels was measured as 6.7 mm (Section 3.7.2.) during the experiments and the length of the pedicels in the numerical simulation was specified as 7 mm.

The stiffness and breaking tension values of the pedicels in the numerical simulation were set equal to the values used for the stems in the numerical simulation. The stiffness and breaking force between the side and main pedicels, as well as the main pedicels and the main stem, were set equal the value obtain from the shearing of the side stems. Since the pedicel diameter could not be measured accurately in the experiments, the breaking tension between the pedicel and the berry was calculated using the stem diameter from the simulation.

40

4.2.3. Simulating a Grape Berry

During the experiments a single berry was placed between two flat surfaces and compressed. The displacement and reaction force experienced by the top surface were measured and recorded, from which the linear stiffness of the berry was calculated (2000 N/m). When duplicating this experiment in the numerical simulation, one should note that the stiffness of a ball is represented by springs that are in contact. As a result, two springs are in series during the compression of a ball between two walls, shown in Figure 39. The stiffness value measured in the experiments should be multiplied by two in order to calculate the stiffness of one spring in the DEM simulation (4000 N/m). Note that in all simulations, the steel walls were given a stiffness of 1e6 N/m.
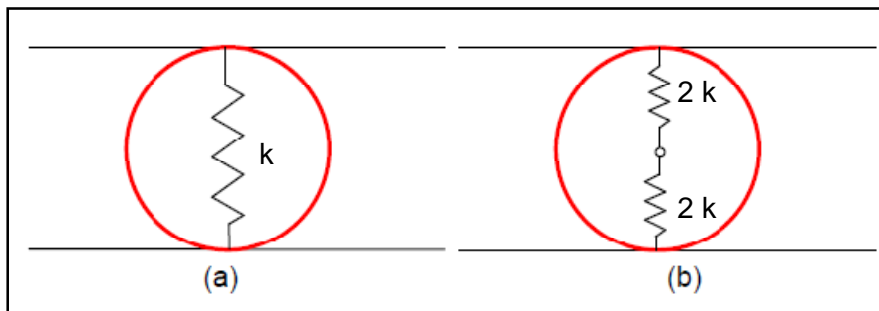
Figure 39 - The measured stiffness of a berry during (a) experiments and (b) the contact model used in DEM.

A single berry (ball) was simulated in the numerical simulation under compression between two walls (Figure 40). When comparing the results from the experiments to those from the numerical simulation, the reaction force over the average maximum displacement (3.5 mm) is more or less the same for the simulation and the experimental results (Figure 41). This is achieved when using a linear contact model with stiffness of 4000 N/m as measured in the experiments.
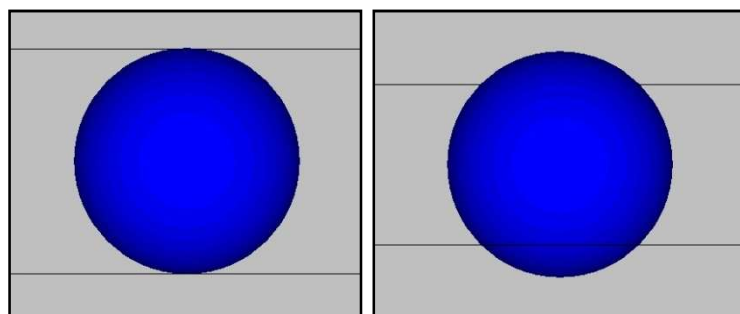
Figure 40 - Compression of a ball between two walls in the DEM simulation.

41
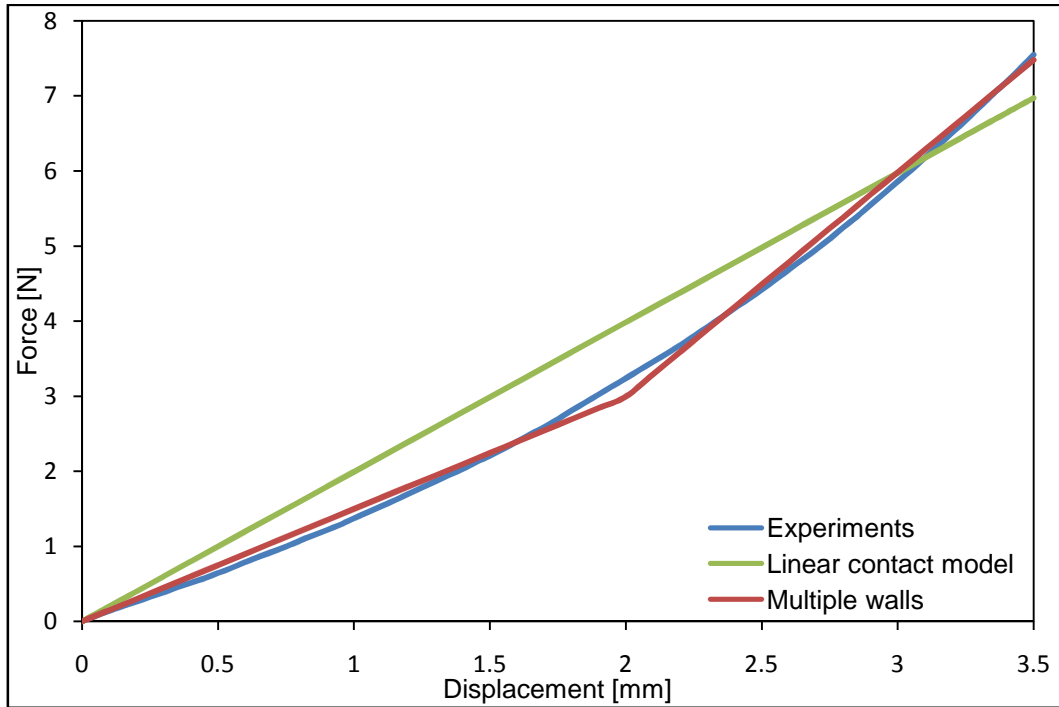
Figure 41 - Force-displacement comparison of the experimental data of the compression of a berry compared to a linear contact model and to using multiple walls in DEM.
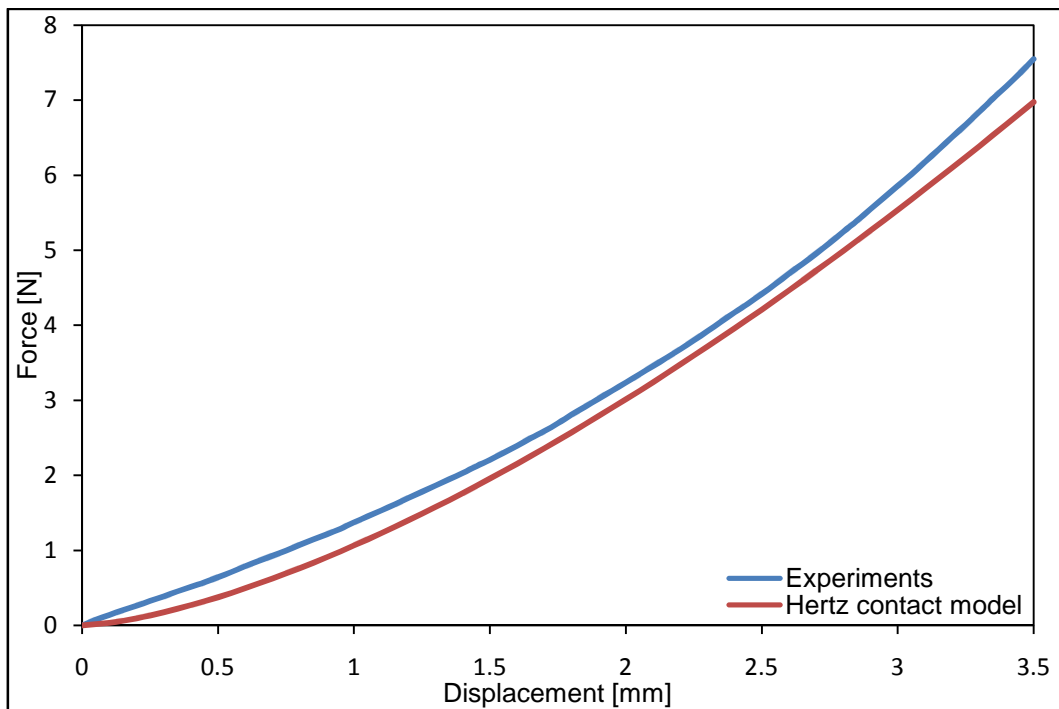
Figure 42 - Force-displacement comparison of the experimental data of the compression of a berry compared to a Hertz contact model used in DEM.

A Hertz-Mindlin contact model, which is a more computational intensive non-linear contact model, was then used to simulate the compression of a berry

42

between two walls. This showed a very good correlation with the experimental results (Figure 42). The shear stiffness (G) used in the Hertz model was 300 kPa with a Poisson's ratio of 0.35. Although the Hertz-Mindlin contact model clearly models the berry more accurately, it could not be used in modelling the complete bunch. In the software used, it was found that when modelling an entire bunch with the Hertz-Mindlin model in combination with parallel bonds, the simulation becomes unstable. The reason for this is unknown and outside the control of the user.

During the simulation of the beater experiment (Section 4.4.) it was found that under high ball-wall contact forces, the deformation of the ball was more than its radius and could move through the wall when using the linear contact model and the stiffness calculated in the experiments. The stiffness of the balls was increased but this influenced the response of the bunches negatively. In a contact, the wall and ball stiffness act in series. The ball stiffness could not be increased significantly, but the wall stiffness could. But since they act in series, the combined stiffness reaches the asymptotic value of k_n^{ball} quickly and increasing the wall stiffness further showed no improvement. Multiple walls were then used to increase the contact force between the ball and the wall (Also see *Appendix E*). Additional walls were placed on the inside of the original wall and when a ball overlapped with the first wall, it made contact with the second wall and another ball-wall contact was formed (Figure 43). These contact forces act in parallel on the ball and thus results in an increase in the resultant force. In this way the resultant force on the ball was increased. Four layers of walls were used.
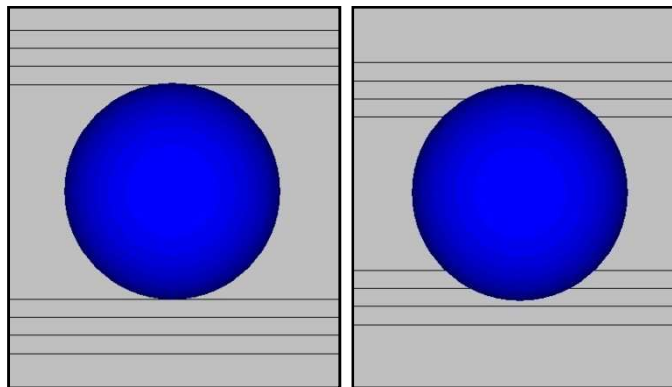
Figure 43 - Compression of a ball in the DEM simulation using multiple walls.

The spacing of the walls resulted in only the first and second wall being in contact with the ball by the time the average maximum displacement was reached. The resultant force-displacement graph was a bi-linear graph that followed the experimental data much closer than the linear contact model, using only one wall. However, since the contact force increased as the number of walls in contact increased, the contact force was much higher than the experimental results when using a ball stiffness of 4000 N/m. In order to ensure that the force displacement graph of the multiple wall contact model followed the experimental results more

43

closely, the ball stiffness was decreased to 3000 N/m (Figure 41). Not only did this solve the problem of the balls moving through the walls, but also modelled the non-linear effect more closely without the use of the Hertz-Mindlin model.

4.2.4. Building a Grape Bunch

The main and side stems of a grape bunch are built by defining the start and end diameter and the start and end co-ordinates. The groups of pedicels are then added by specifying the position and orientation and a berry is added at the end of each pedicel. All the geometric data are stored together with the stiffness, breaking force and friction settings in a set of texts files. These files are imported into PFC^{3D} and the bunch is built.

Each stem in the bunch is assigned a unique number and the bunch is divided into five groups: the main stem, side stems, the main pedicel, side pedicels and berries. The data text files are divided into two groups, one group to store all the data of the main and side stems and one group to store all the data of the pedicels and berries. The group that contains the data of the main and side stems is further subdivided into three groups containing information regarding the geometric layout, the ball and bond properties of the stems, and the bond properties of the connection between the side and main stem. The group containing the data regarding the pedicels and berries is also subdivided into four subdivisions containing geometric data, ball and bond properties of the main pedicel, ball and bond properties of the other pedicels, and ball and bond properties of the berries. The density and friction coefficients of the balls are also included in these files.

Some small geometric deviations were experienced during the building of the bunches in DEM. As mentioned earlier (Section 4.2.1.) the actual length of the stem can differ from the specified length due to the fact that the sum of the diameters of the balls does not equal the specified length. When bonding side stems, the specified co-ordinates are used and the nearest ball is then found and connected to. This ball's co-ordinates could differ slightly from the specified co-ordinates. All these deviations in the geometry of the bunch result in deformations and overlapping of balls, causing larger forces in the bunch than the specified breaking forces. These forces can cause the stems to break and berries to come off the stems when the bunch is first simulated. To prevent this, the bonding strength in all the bonds in the bunch is increased by a large factor while the bunch is allowed to relax. After the bunch is allowed to relax under gravity, the bond strengths are reduced to the original values.

4.3. Geometric Comparison of Grape Bunches

The geometric layout of the bunches built in DEM was based on actual bunches. The first bunch that was built featured small shoulders and a small cylindrical body (Figure 44 nr 1). The next bunch was larger and featured four large shoulders with berries tightly packed. The rest of the body of the bunch was long

and cylindrical (Figure 44 nr 2). The third bunch also had a cylindrical body but no shoulders and the berries were also tightly packed (Figure 44 nr 3). The fourth and fifth bunches were based on the second and third bunches respectively (Figure 44 nr 4 and nr 5). It was found that the berries on the second and third bunches were tightly packed and as a result, bunches four and five were built as stretched versions of bunches two and three. The length, number of berries and weight of each bunch are given in Table 8. Also see Section 3.7.4. for experimental data.
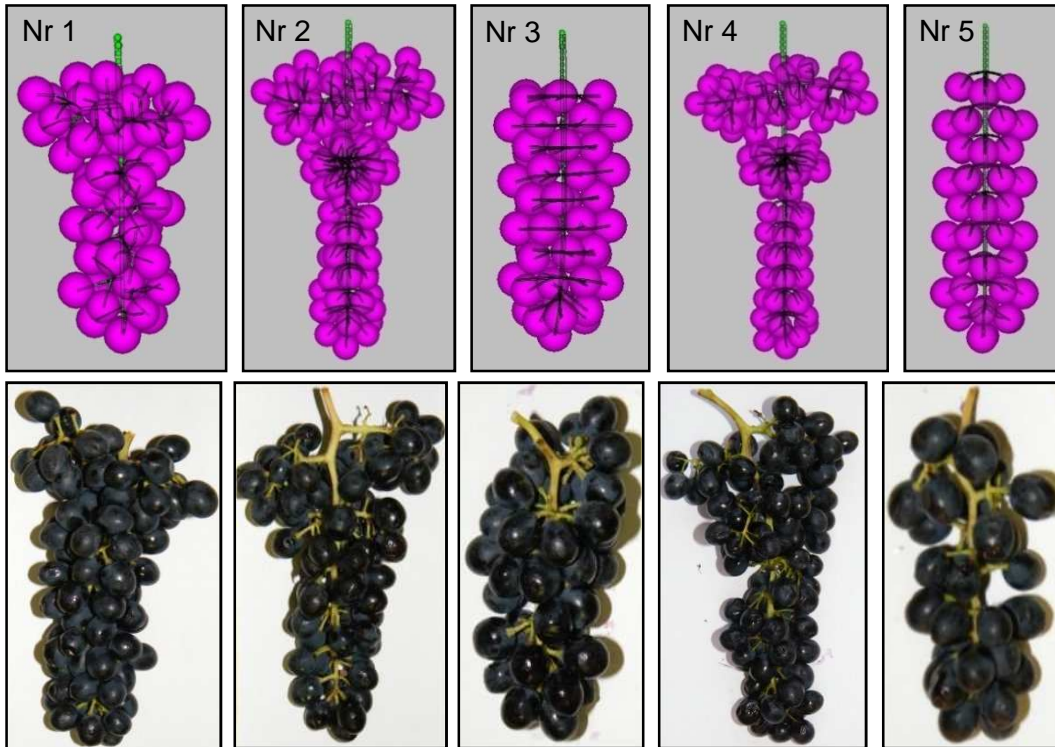
Figure 44 - The grape bunches built in DEM.

Table 8 - Properties of bunches built in DEM.

Bunch Number	Number of Berries	Weight [g]	Length [mm]
1	61	89	100
2	110	160.7	145
3	56	80.5	100
4	110	160.9	160
5	56	80.7	120
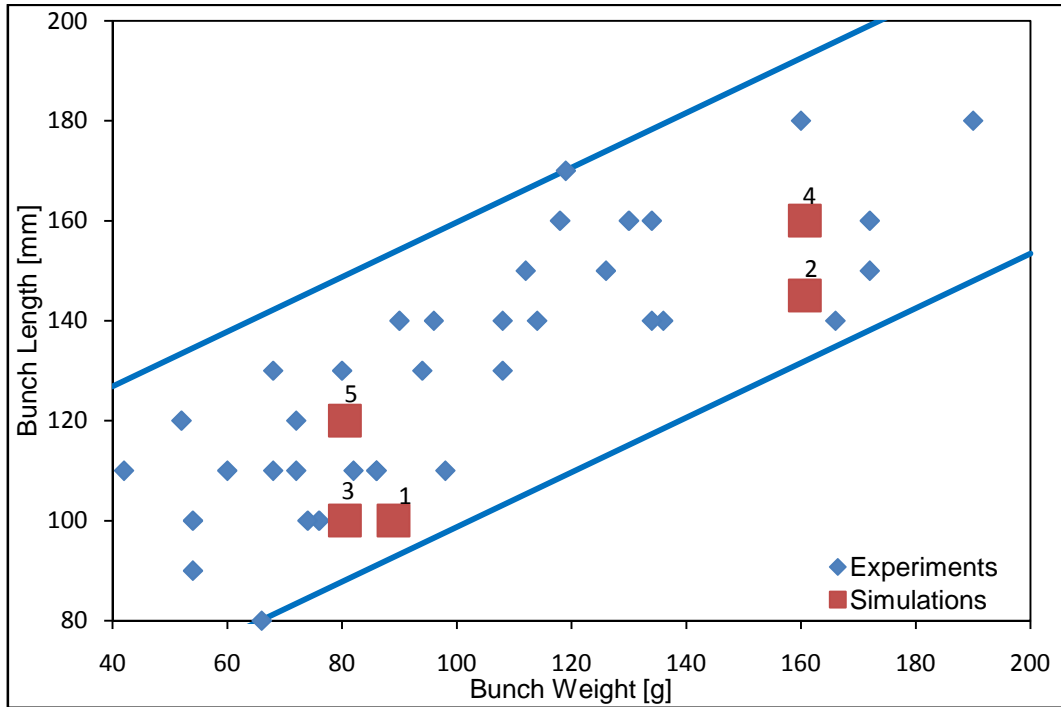
Figure 45 - Comparing the bunch length to the bunch weight.
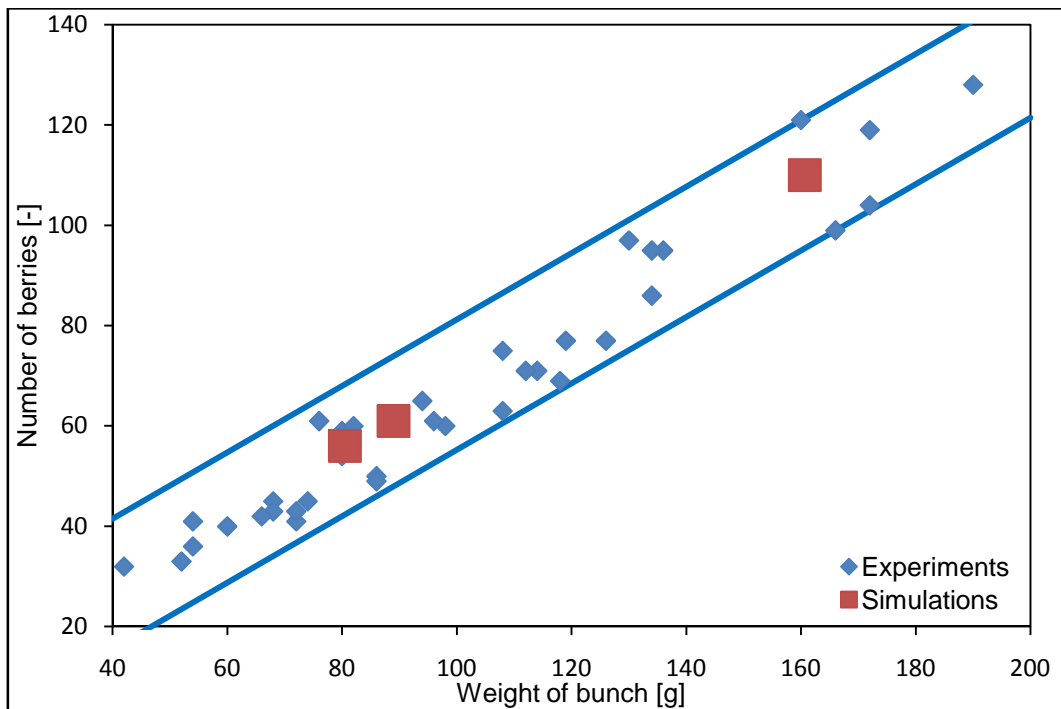
Figure 46 - Comparing the number of berries to the bunch.

When comparing the length, weight and number of berries of the bunches to the experimental data, all the bunches fall within the experimental range. Figure 45 shows the length of the bunches compared to the weight of the bunches for both the experiments and the simulations. The bunch numbers are included for the

46

simulation data. Note how bunch numbers 2 and 4 and bunch numbers 3 and 5 have equal weight but different lengths due to the fact that the berries were packed less tightly. When comparing bunches 1 and 3, one can see that both bunches have equal length but due to the shoulders of bunch 1, it has a larger weight. Please note that in order to make the graphs more clear, the experimental range is shown by the two blue lines in the graphs. The gradient of the trendline from the experimental data was used and manually offset to include all the experimental data between the two lines.

Figure 46 shows the number of berries compared to the weight of the bunch for both the experiments and the simulations. Only three data points from the simulations are visible due to the fact that bunches 2 and 4 and bunches 3 and 5 have very similar weight. All the bunches from the simulations fall in the same data range as the bunches measured in the experiments.

4.4. Beater Simulation

4.4.1. Setup
The beater experiment was simulated in order to investigate the possibility of simulating a grape bunch under destemming conditions, as well as to act as a calibration method of the bunch material properties. The geometrical layout of the beater bars, the stopper bar and the outside walls were taken from the experimental setup and replicated in the simulation. All the walls replicating the experiment were built first, followed by the building of the bunch in a position similar to that in the experiments. The position of the bunch was determined by specifying the co-ordinates of the top ball of the main stem, which was then fixed in that position. The bunch was then allowed to relax and hang under gravity. After the bunch came to rest, the rotation of the beaters was started and the fixed top ball was released.

4.4.2. Running of Simulations
During the running of the simulation, the breaking of bonds was constantly monitored. When a bond broke, the time, co-ordinates of the bond, the breaking stress, type of failure (normal or shear) as well as the type of balls (main stem, side stem, pedicel, berry) between which the bond failed was recorded. This could then be used to determine how many berries were removed from the stem, how many stems broke off and which type of stems broke off.

For visual comparison purposes, pictures were created at every 1/1000 second intervals. To further improve the understanding of the destemming process through visual interpretation, the colour of the balls between which a bond broke was immediately changed to red (Figure 47). This improved the visualisation of where and how the berries were removed from the stems. These pictures were also used for visual comparison with the pictures taken by the high speed camera during the experiments. The rotation speed of the beaters in the experiments

ranged from 400 to 550 rpm and the simulations were done at increments of 50 rpm over this range.
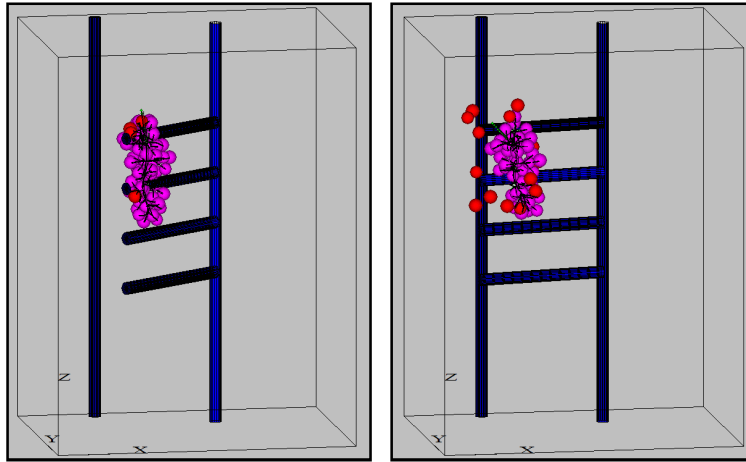
Figure 47 - Picture created in the simulations. Pictures showed at intervals of 8/1000 s.

From the data recorded during the experiments, it could be seen that the beaters showed a backlash effect when hitting the stopper bar. This backlash involved the beaters jumping back a little after hitting the stopper bar and hitting the bunch again, but this time at a much lower speed. To ensure the accuracy of the simulations, this backlash effect was included in the simulations by reversing the rotation of the beaters for about 30°, once it reac hed the stopper bar. When the rotation was reversed, the rotation speed was also decreased by a factor of 3. The rotation of the beaters were then reversed again (to its first direction), the speed reduced by a factor of 4 and rotated until it reached the stopper bar again.

From the pictures taken by the high speed camera during the experiments, as well as from the pictures created during the simulations, it was observed that the position in which the bunch hit the stopper bar, had an influence on the results. Some of the berries were removed when the bunch was hit by the beaters. The rest of the bunch was then accelerated to the rotation speed of the beaters. When the whole bunch hit the stopper bar, the bunch experienced a large deceleration, which resulted in a large number of berries being removed. When only half or part of the bunch hit the stopper bar, fewer berries were removed. During the simulations it was also observed that as the rotation speed of the beaters varied, the slippage of the bunch along the beaters varied slightly and as a result the orientation of the bunch relative to the stopper bar changed.

4.4.3. Calibration of Parameters

After initial calibration of the various bond strengths as well as the bond and ball stiffnesses (Section 4.2.), the grape bunch was modelled in the beater simulation using these values. As mentioned in Section 4.2.*,* the values obtained from the

experiments were adjusted during the beater simulation. This acted as a calibration process for the behaviour of the bunch.

The calibration of the bunch was done by visual comparison of the pictures created during the simulation, with the pictures taken by the high speed camera during the experiments. The data from the simulations was also compared to the experimental data using the same graphs used to present the experimental data (Section 3.4.3.). Please note that in order to make the graphs more clearly in this chapter, the range of the experimental data is shown by the two blue lines in the graphs. The gradient of the trendline from the experimental data was used and manually offset to include all the experimental data points. For clarity, in some of the graphs the experimental data were removed and only the range lines are shown.

It was found that nearly all the parameters in the simulation had an influence on the results. Certain parameters were also influenced when other parameters were changed. The parameters were calibrated by adjusting one parameter at a time. A set of simulations was then run and the results were compared to the results of previous parameter settings and experimental results. The parameter would then be adjusted and the simulations repeated until the results showed a good correlation with the experimental results. The simulations were computationally very intensive and took several hours to complete. As a result, the number of simulations that could be done in the allowable time for this study was limited.
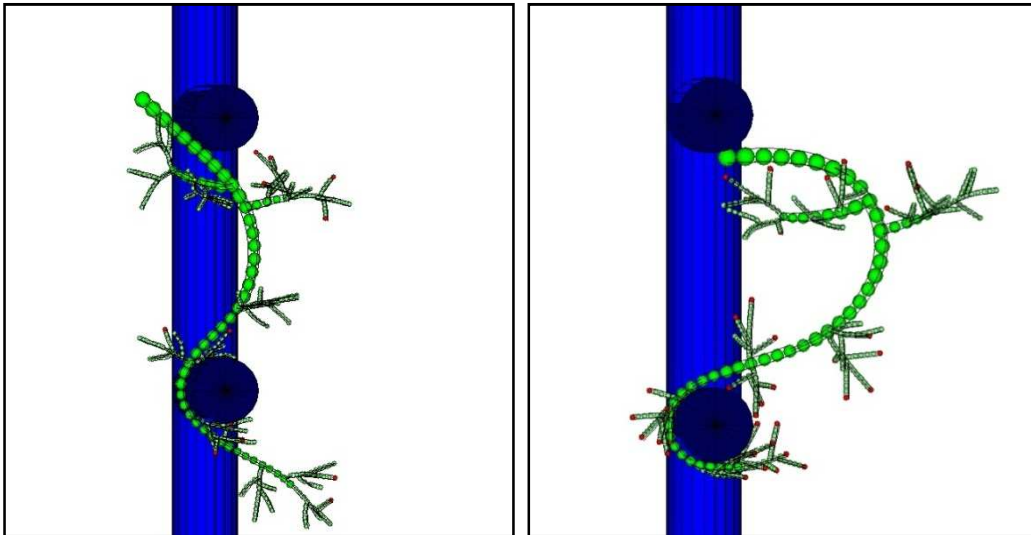
Figure 48 - Bunches shown with high stem stiffness (left) and low stem stiffness (right). Berries not shown in pictures.

First, the bond strength of the stems was adjusted. During the first simulations, using the measured values, it was found that the bond strengths of the stems were too low. After increasing the bond strength, the bond stiffness was

increased. The stiffness of the stems appeared to be too low under bending when it was hit by the beaters (Figure 48). As the stiffness of the stems was increased, the breaking force needed to be adjusted again, since the large deflections and increased stiffness resulted in higher stress values. After various combinations of bond strengths and stiffnesses were tested, the final stem stiffness (modulus of elasticity) used in the simulations was 500 MPa, roughly 5 time higher that the measured stiffness of 95 MPa. The final stem strength used was 100 MPa, 10 times higher than the measured strength of 10 MPa. The strength and stiffness of the bond connecting the side stems to the main stem, were given these same values.

The bond strength of the pedicels was also found to be too low. When using the measured results, nearly all the pedicels broke off. The final strength used for all the bonds involving the pedicels was 50 MPa while the stiffness was left at the measured value of 95 MPa.

PFC^{3D} offers two types of damping for the contact model used, namely, contact viscous damping and local damping, as explained in (*Appendix A*). Local damping was used while the bunch was allowed to relax and settle while hanging. Local damping was then switched off and contact viscous damping was used during the rest of the simulation where the bunch was hit by the beaters. Contact viscous damping uses a viscous damping model for ball-ball and ball-wall contact. Simulations were run with and without contact viscous damping and the results are shown in Figure 49. It was found that as the contact viscous damping was increased, the gradient of the trendline fitted to the simulation data increased and tended towards the gradient of the trendline fitted to the experimental data. The data shown did not fit the experimental data very well since more calibration still had to be done. The results were only included to show the increase in the gradient of the trendline as the contact viscous damping was increased. Contact viscous damping was set to a factor of 0.9, where 1.0 equals critical damping and 0.0 is no damping.

The parameter that had the biggest influence on the results was the bond strength between the berries and the pedicels. The value obtained from the experiments, 2 MPa, was found to be too low and too many berries were removed. Bond strengths between 3.5 MPa and 6 MPa were tested at 0.5 MPa intervals. The results are shown in Figure 50, Figure 51 and Figure 52. In these figures one can clearly see how the number and percentage of berries removed increased as the bond strength decreased. It was found that a bond strength of 4.5 MPa gave the best results. A trendline was fitted to this data and is shown in the figures.
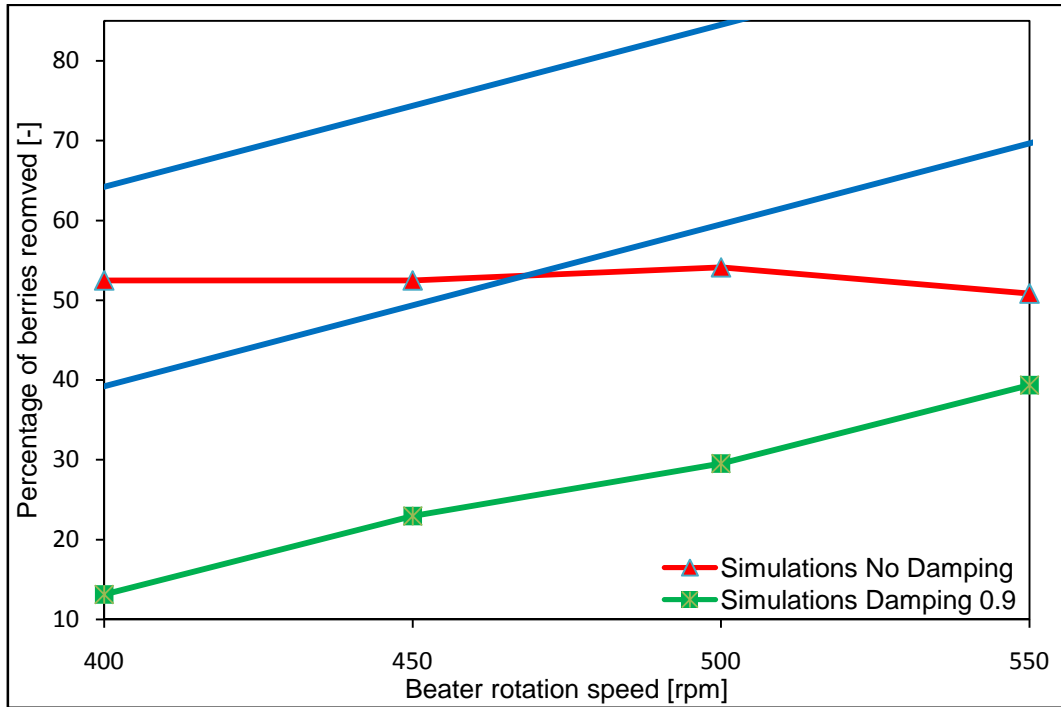
Figure 49 - The effect of contact viscous damping in the simulations when comparing the percentage of berries removed to the beater rotation speed.
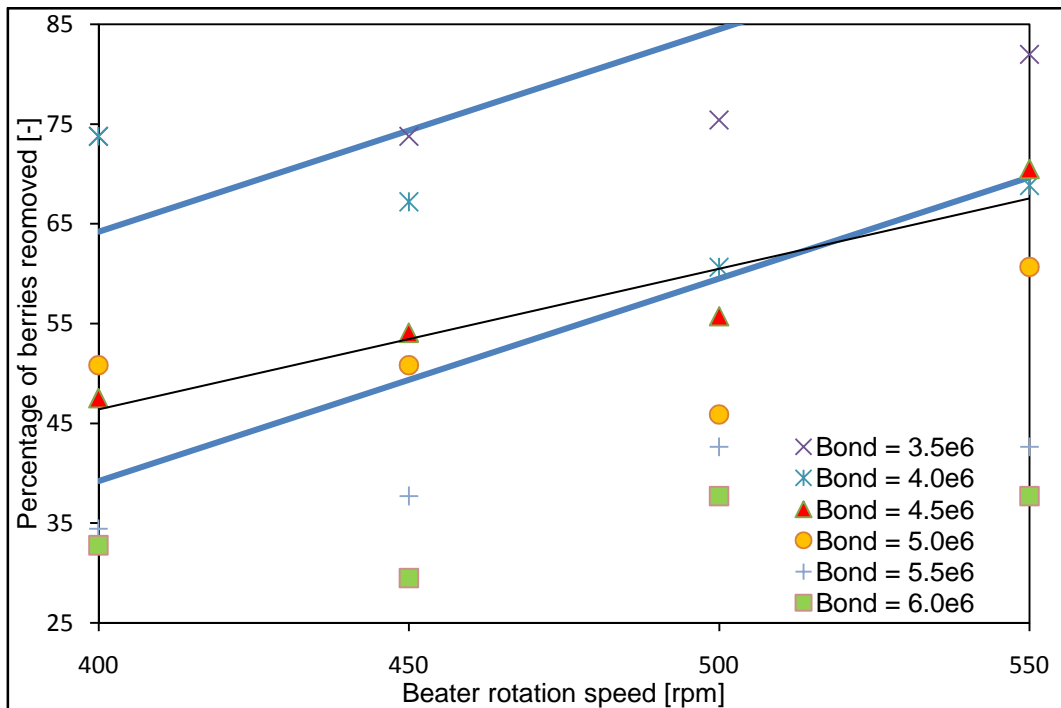
Figure 50 - Influence of the berry bond strength when comparing the percentage of berries removed to the rotation speed of the beaters.

51
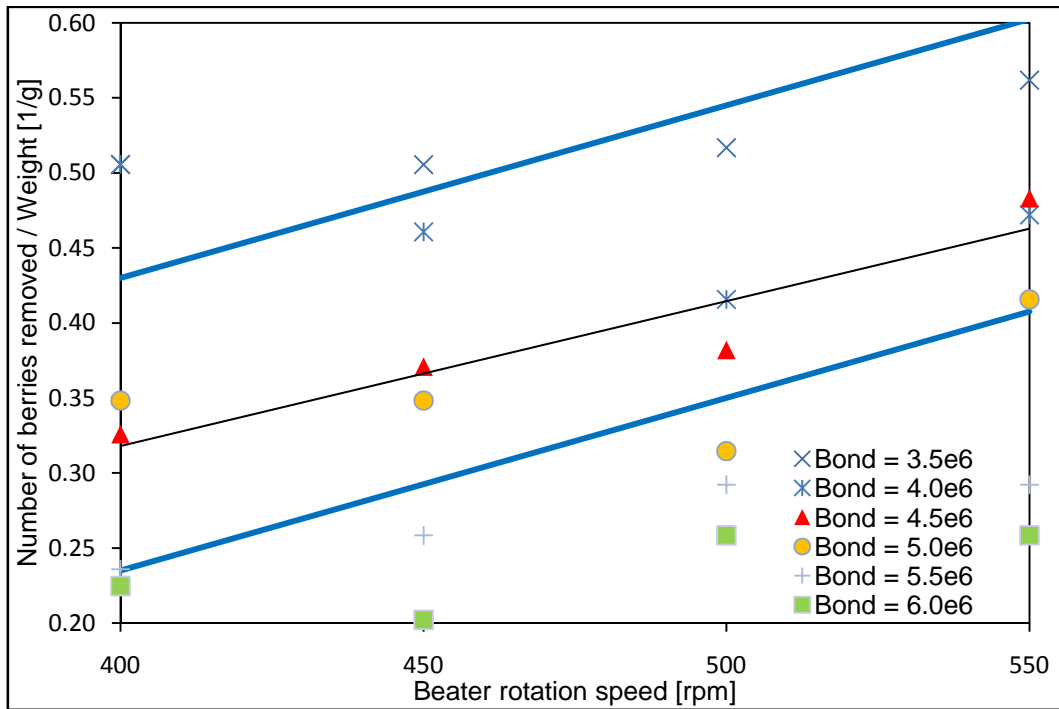
Figure 51 - Influence of the berry bond strength when comparing the number of berries removed, divided by the weight of the bunch, to the rotation speed of the beaters.
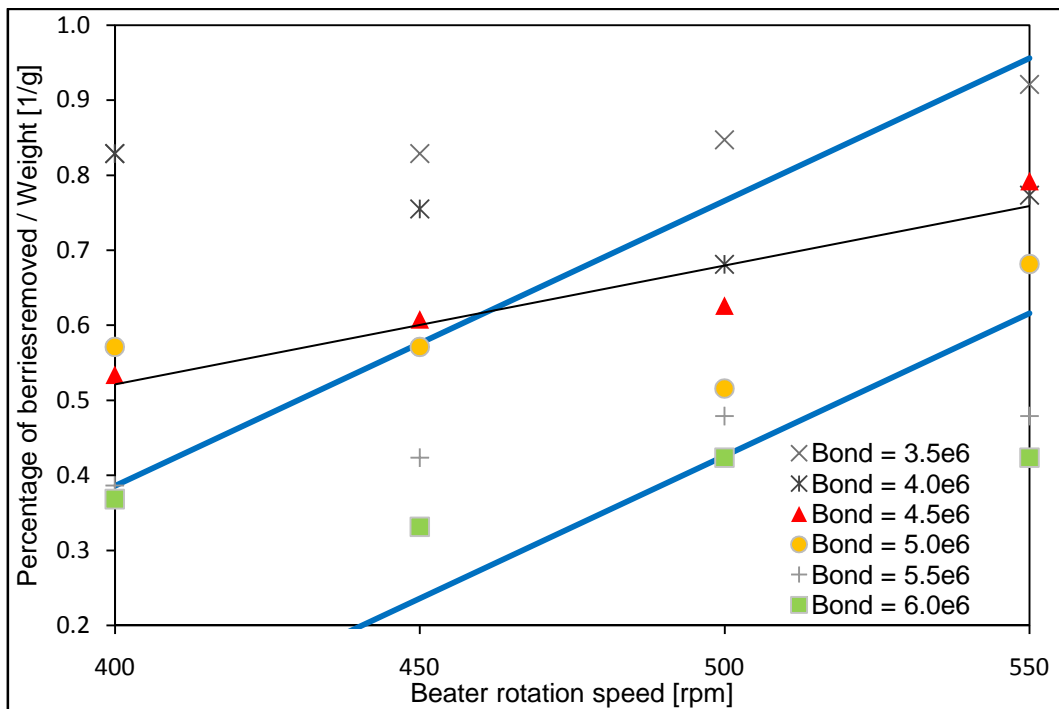
Figure 52 - Influence of the berry bond strength when comparing the percentage of berries removed, divided by the weight of the bunch, to the rotation speed of the beaters.

52

The berry linear stiffness was measured as 4000 N/m and this value was used in the initial simulations. However, it was found that the balls can pass through the walls at high contact force scenarios. To prevent this, multiple walls were used as described in Section 4.2.3. When using multiple walls, the ball-wall contact stiffness increased as the deflection of the ball increased. In order for the simulated results to correlate with the experimental results (Figure 41), the ball stiffness was lowered to 3000 N/m.

A berry friction coefficient of 0.1 and 0.5 was tested while using single and multiple walls. The change in the friction coefficient had no significant effect on the results in any of the comparisons and a friction coefficient of 0.1 was used in all further simulations.

All these calibration adjustments were done using only the first bunch. After the results from the simulations of this bunch correlated well with the experimental results, the other four bunches were built. The parameters used in the first bunch were used in all the other bunches and no adjustments were made. This was done to investigate the consistency of the model parameters and the applicability of these parameters to various bunches.

Table 9 shows the material properties as measured in the experiments and the final properties used in the simulations after calibration. The material properties of the berry, the berry-pedicel bond, and the pedicel stiffness needed the least adjustment, while all the stem properties needed larger adjustments. The reason why the measured properties had to be adjusted to achieve accurate beater results might be attributed to the following factors. It is well known that biological material does not behave linearly but rather non-linearly. The behaviour of the material also tends to be speed dependant and a non-linear visco-elastic model seems to describe the general behaviour more accurately (Raji & Favier, 2004b). Due to software limitations, a linear contact model and a linear bond model were used in the study. The material properties were measured under quasi-static conditions with speeds of up to 2.4 mm/s. Higher speeds could not be used due to equipment limitations. During the beater experiment and simulations, the beater tip speeds were up to 7.5 m/s. Since the linear models used in the simulation could not take the speed effect into account, this might be one of the reasons why the material properties had to be adjusted.

The stem stiffness was only measured under axial loading. The modelled stem was then set to have the same axial stiffness. The stems could not be tested under bending due to the rather small forces and large displacements under bending. In the model, the stem axial behaviour is governed by the bond normal stiffness, k_n^{bond}, while the bending behaviour is governed by the bond shear (tangential) stiffness, k_s^{bond}. Since the bending stiffness could not be measured, the bond shear stiffness was set equal to the bond normal stiffness. In future, the

53

bending stiffness of the stems should be measured and different values for the bond normal and shear stiffness could be specified.

Table 9 - Comparison of the calibrated values of parameters used in the simulation to the values measured in the experiments.

	Parameter	Measured	Simulations
Material Properties			
Main Stem	Bond Stiffness	95 MPa	500 MPa
	Bond Strength	11.6 MPa	100 MPa
Side Stem	Bond Stiffness	95 MPa	500 MPa
	Bond Strength	11.6 MPa	100 MPa
Pedicels	Bond Stiffness	95 MPa	95 MPa
	Bond Strength	11.6 MPa	50 MPa
Berries	Ball Stiffness	4000 N/m	3000 N/m
Connection Properties			
Main-Side Stem	Bond Stiffness	14 MPa	100 MPa
	Bond Strength	3.4 MPa	50 MPa
Stem-Pedicel	Bond Stiffness	14 MPa	95 MPa
	Bond Strength	3.4 MPa	50 MPa
Main Pedicel-Pedicel	Bond Stiffness	14 MPa	95 MPa
	Bond Strength	3.4 MPa	50 MPa
Pedicel-Berry	Bond Stiffness	8.6 MPa	9 MPa
	Bond Strength	2 MPa	4.5 MPa
Other Parameters			
Density	Berries	1130 kg/m^3	1110 kg/m^3
	Stems	1110 kg/m^3	1110 kg/m^3
Friction	Berries	-	0.1
	Stems	-	0.1

4.4.4. Results

All five bunches were simulated at beater speeds of 400, 450, 500 and 550 rpm. The results from these five bunches were then processed in a similar way as the experimental results. The results from all five bunches are shown in Figure 53 to Figure 56 and a trendline was fitted to the data. The results from the simulations can now be compared to the experimental upper and lower bounds.

When comparing the number of berries removed to the weight of the bunch (for all beater speeds), the majority of the simulation results fall inside the experimental bounds (Figure 53). Only one point is located outside but is still very close to the experimental range. The trendline fitted to the simulated data shows a good correlation with the experimental gradient.

When comparing the percentage of berries removed to the weight of the bunch (for all beater speeds), the results from the simulations do not compare as well to

the experimental data (Figure 54). Less than half of the data points are located inside the experimental bounds with points both above and below these limits. When a trendline is fitted to the data, the gradient of the trendline does not correlate well with the trend, as seen in the experiments.
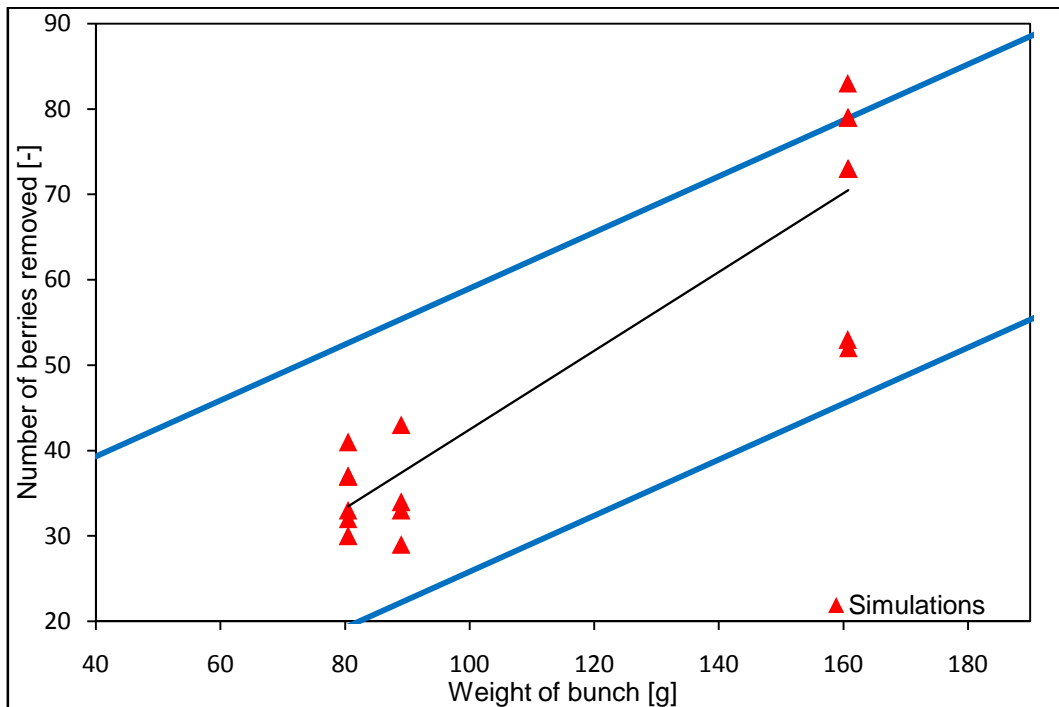
Figure 53 - Simulation results for comparison of the number of berries removed to the weight of the bunch.

A good correlation can be seen between the experimental and simulated data when comparing the percentage of berries removed to the rotation speed of the beaters, for all weights (Figure 55). Only two of the twenty data points are not located inside the experimental bounds and can be found very close to the lower boundary. It seems that there is a trend that the simulated data deviates more from the experimental data with an increase in the beater speed. This again confirms that the model cannot model the rate dependant effect very accurately and a visco-elastic contact and bond model might provide better results.

The comparison of the number of berries removed, divided by the weight, to the rotation speed of the beaters, gave the best correlation of all the graphs used for comparison (Figure 56). All the data points from the simulation are well inside the experimental bounds. The simulation results are also well grouped and form a range that is smaller than the experimental range. The trendline fitted to the simulation data fits the experimental range extremely well and is located almost exactly midway between the upper and lower bounds with a gradient nearly equal to the experimental trend.
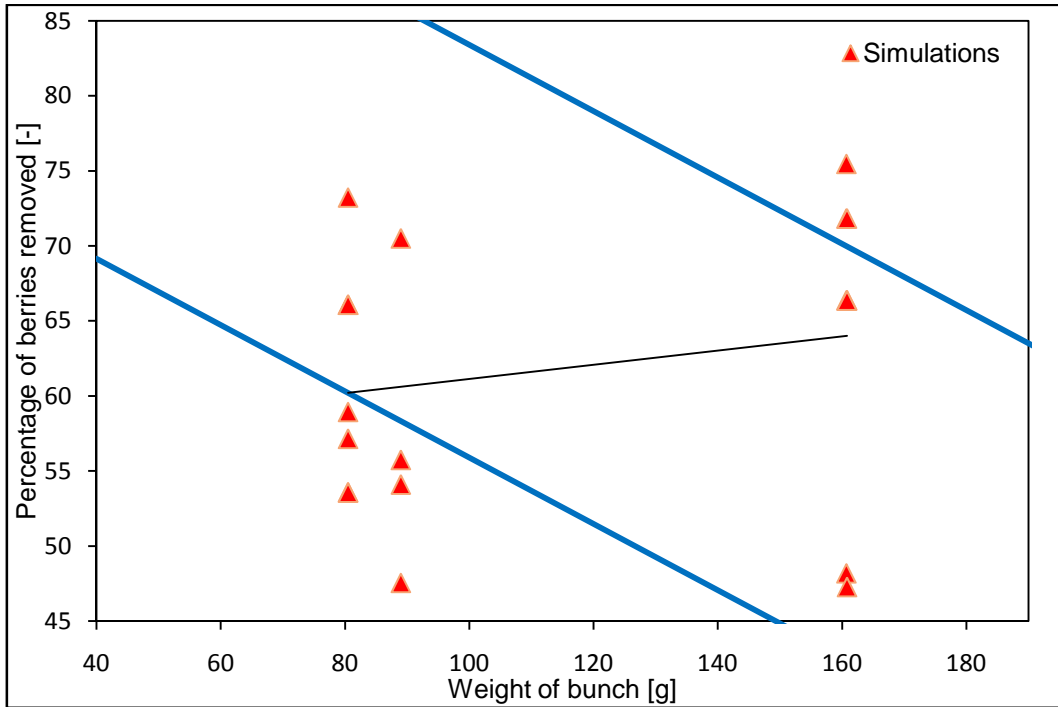
Figure 54 - Simulation results for comparison of the percentage of berries removed to the weight of the bunch.
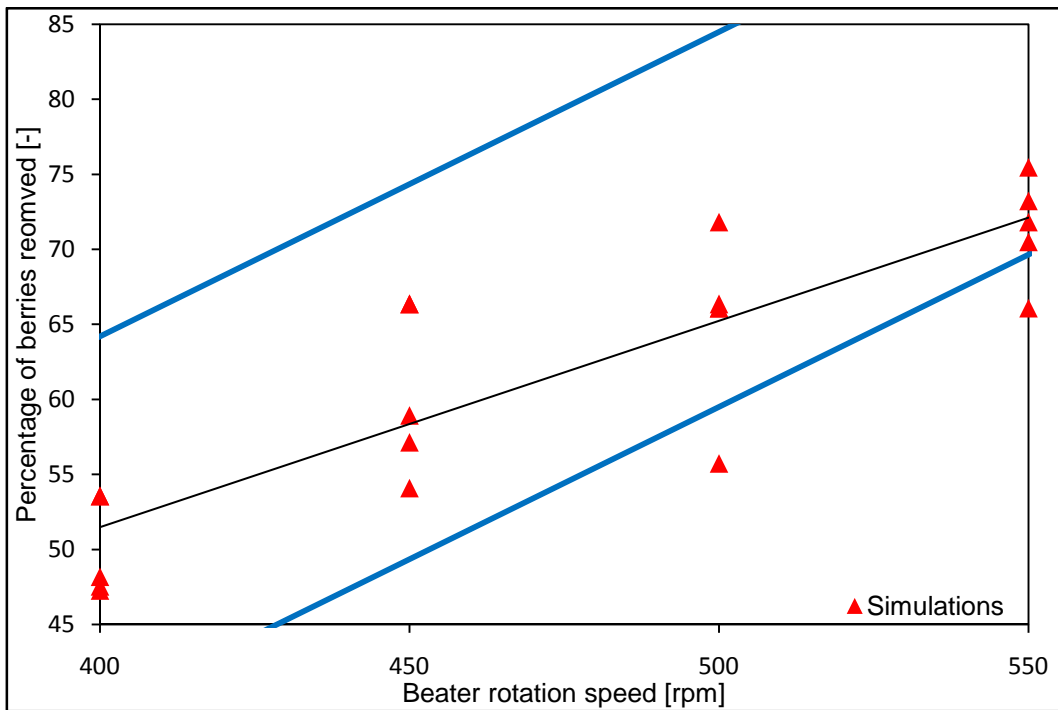
Figure 55 - Simulation results for comparison of the percentage of berries removed to the rotation speed of the beaters.
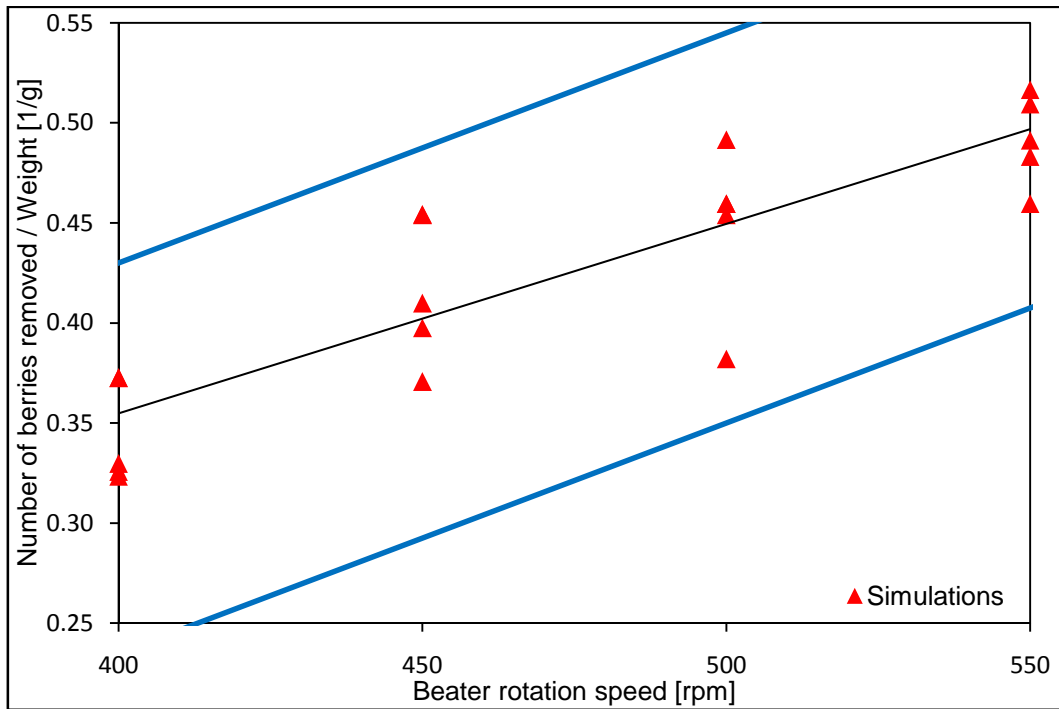
Figure 56 - Simulation results for comparison of the number of berries removed, divided by the weight of the bunch, to the rotation speed of the beaters.

The bunches that were built in the simulations consisted of one small shouldered bunch (bunch 1), two large shouldered bunches (bunches 2 and 4) and two smaller cylindrical shaped bunches (bunches 3 and 5). The influence of the bunch shape on the results is shown in Figure 57, Figure 58 and Figure 59. By comparing the results from the two large shouldered bunches (green in graphs) to the two smaller cylindrical bunches (red in graphs), the effect of bunch size and shape can be seen.

Figure 57 shows the four bunches when comparing the percentage of berries removed to the rotation speed of the beaters. Although the results of the four bunches are very closely spaced, one can see the correlation between the two smaller and larger bunches. Very similar results can be seen in Figure 58.

A more clear distinction can be made between the two types of bunches in Figure 59 where the percentage of berries removed, divided by the weight of the bunch, is compared to the rotation speed of the beaters. The two types of bunches are completely separated, but follow a similar trend. From the graph, it can be seen that the smaller cylindrical bunches loose a higher percentage of berries per bunch weight, than the larger bunches. A possible explanation for this is that when the bunch hits the stopper bar, after being hit by the beaters, the stopper bar has contact with a larger percentage of berries in the case of the smaller bunches, which could result in higher percentage of berry loss. When the larger bunches hits the stopper bar, the shoulders have very little contact with the stopper bar.

57
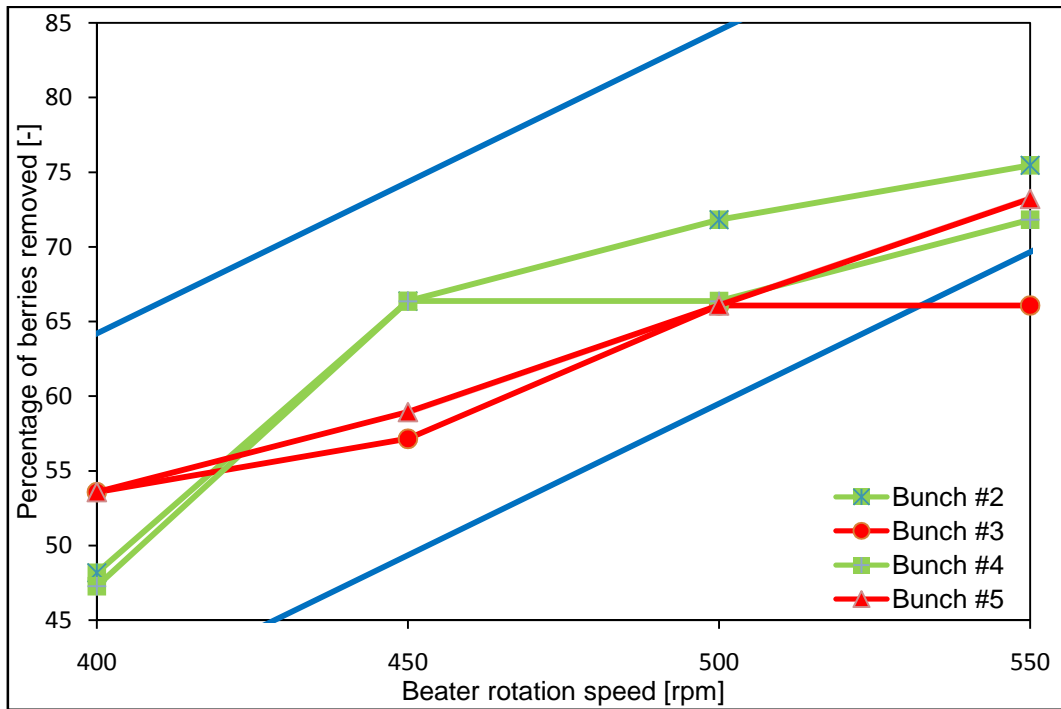
Figure 57 - Comparison of large shouldered and small cylindrical bunches when comparing the percentage of berries removed to the rotation speed of the beaters.
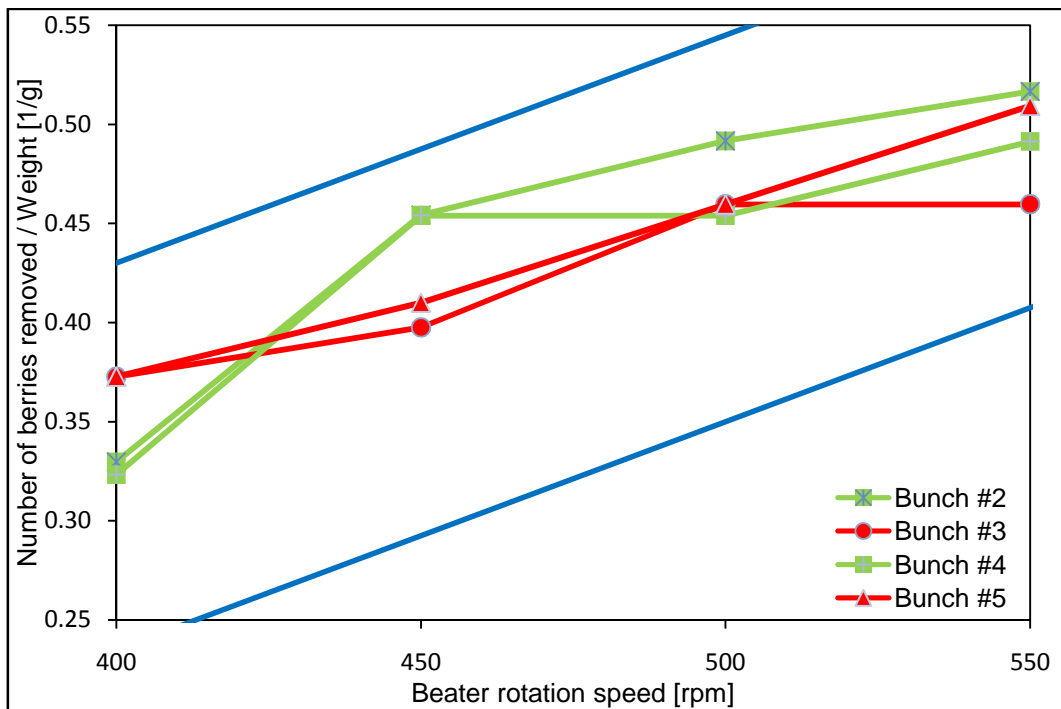
Figure 58 - Comparison of large shouldered and small cylindrical bunches when comparing the number of berries removed, divided by the weight, to the rotation speed of the beaters.
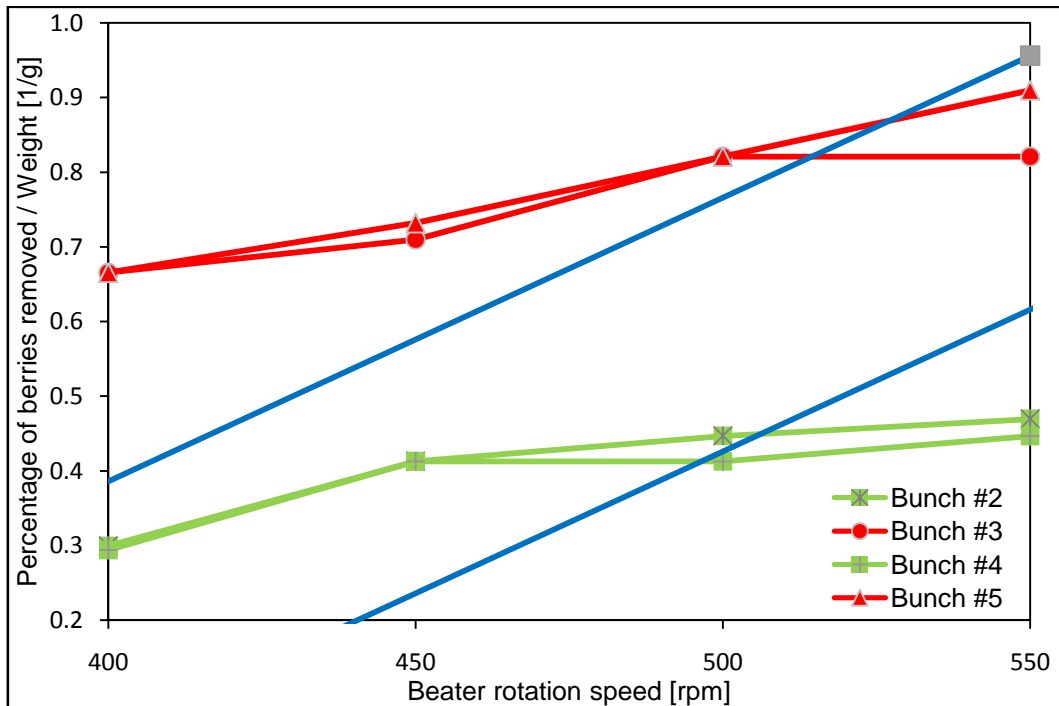
Figure 59 - Comparison of large shouldered and small cylindrical bunches when comparing the percentage of berries removed, divided by the weight, to the rotation speed of the beaters.

When comparing the pictures taken by the high speed camera and the pictures created by the simulation, one can see a very good comparison. When looking at the series of pictures in Figure 60, one can see how the bunch behaves similarly when it is hit by the beaters. The removal of the berries from the stem when the bunch hits the stopper bar is also very clear. It does seem however that the bunch behaves more rigidly in the experiments when struck by the beaters than in the simulations. During calibration, the stem was made more rigid by increasing the stem stiffness and this resulted in an improvement in the behaviour of the stem, as shown in Figure 48. Since the stem stiffness used in the final simulations was already 5 times the value that was recorded during the experiments, the stem stiffness was not increased further.

The data from the simulations were used and a bi-linear fit was done to the data. A bi-linear equation was fitted to the weight of the bunch, the rotation speed of the beaters and the number of berries removed (Figure 61). A good correlation coefficient (R^2) of 0,97 was obtained. From the plot one can see how the number of berries that was removed increased as the beater rotation speed and weight of the bunch increased. The graph suggests that the weight of the bunch had the biggest influence on the number of berries being removed. When comparing the experimental results (Figure 62) to the results from the simulations (Figure 61), one can see that the results compare very well.

59
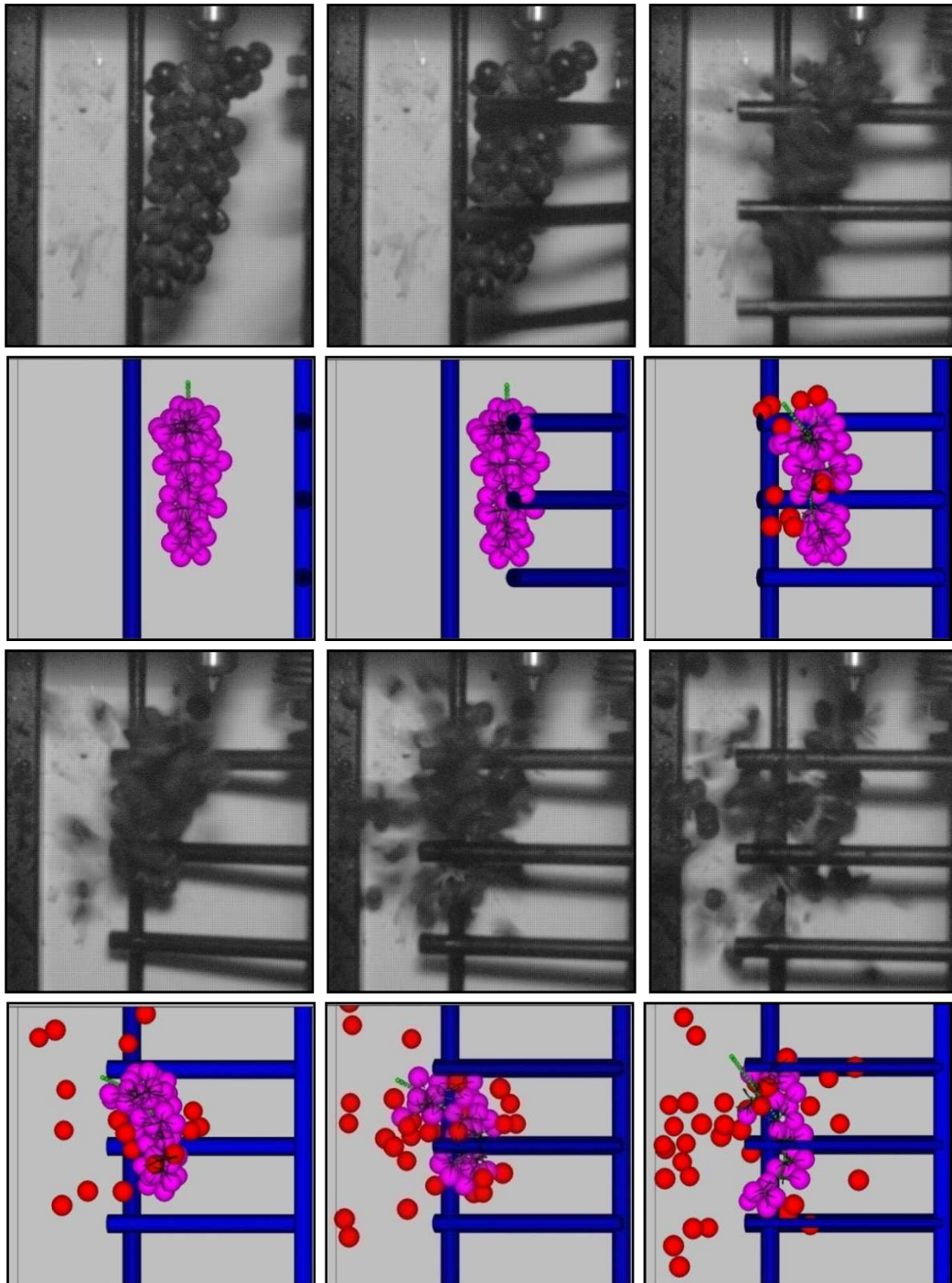
Figure 60 - Visual comparison of beater experiments and simulations. Pictures at intervals of 1/100 s.
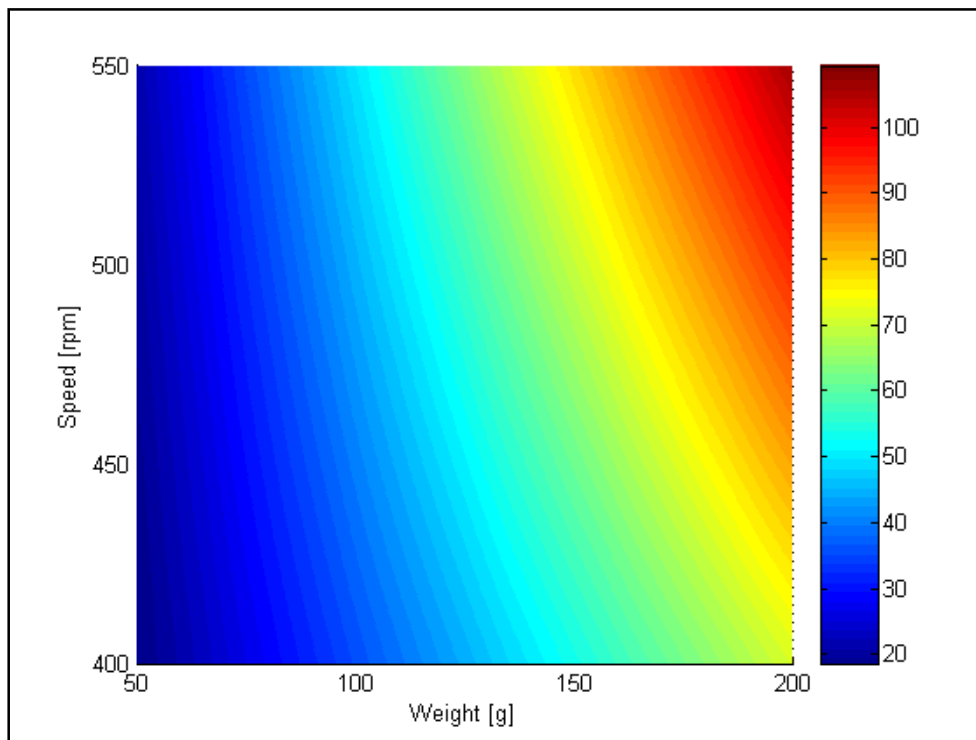
Figure 61 - A contour plot of the simulation results. The contours indicate the number of berries removed.
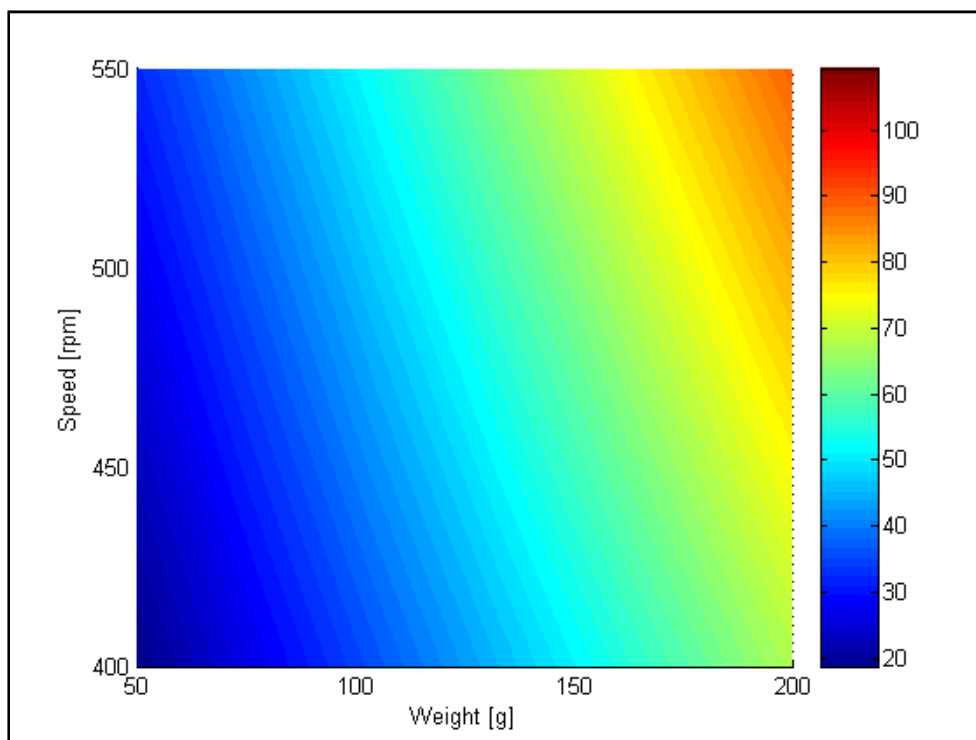
Figure 62 - A contour plot of the experimental results. The contours indicate the number of berries removed.

The general conclusion was that the model could simulate the experiments well. Good comparisons could be seen between almost all the graphs that were used for evaluating the experimental and simulation results. Visual comparison between the simulations and the experiments were very handy for calibration purposes and showed good comparison.

4.5. Destemmer Simulation

4.5.1. DEM Model

Building a destemmer in DEM is very challenging since a large number of walls are needed to model all the components of the destemmer. The geometric layout of the drum and beater shaft is very complex and is difficult to model in DEM. Simplifications to the model were kept to a minimum, especially to the components involved before and during the destemming process. In Figure 63, the DEM model of the destemmer and the destemmer used in the experiments are shown.
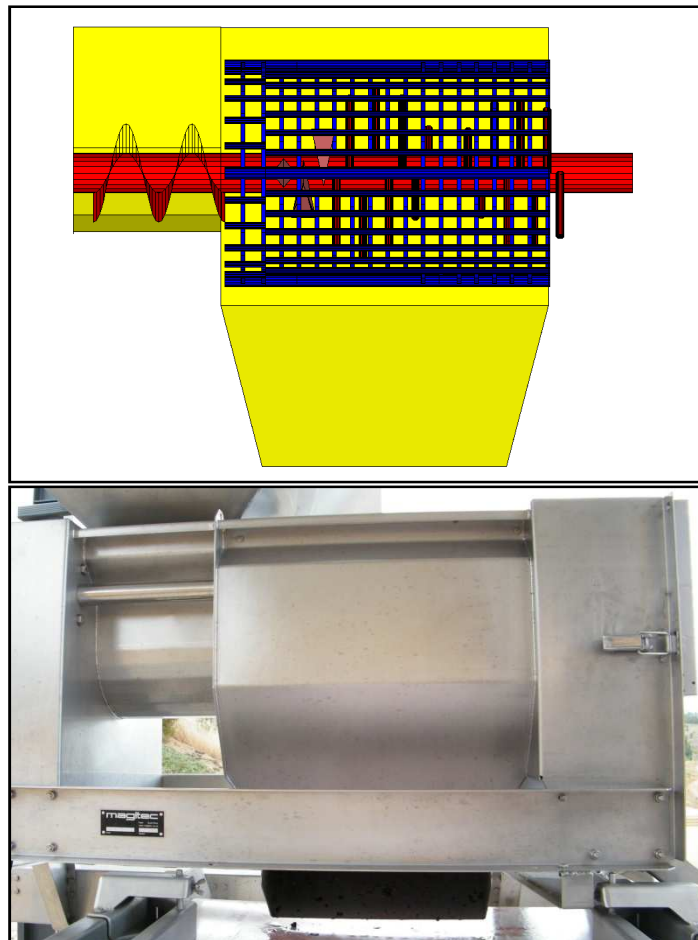
Figure 63 - A comparison of the model of the destemmer built in DEM to a photo of the destemmer.

During the beater simulations, it was found that under high ball-wall contact forces, the balls can move through the walls. To prevent this, all the beaters and beater pins were created with multiple walls at an offset of 1 mm. The beater shaft of the machine used in the experiments, had two rows of rubber beaters where the grapes entered the machine (Figure 64). On the rest of the beater shaft it used stainless steel pins. The destemmer used a small screw conveyor to feed the grapes into the drum and onto the rubber beaters.
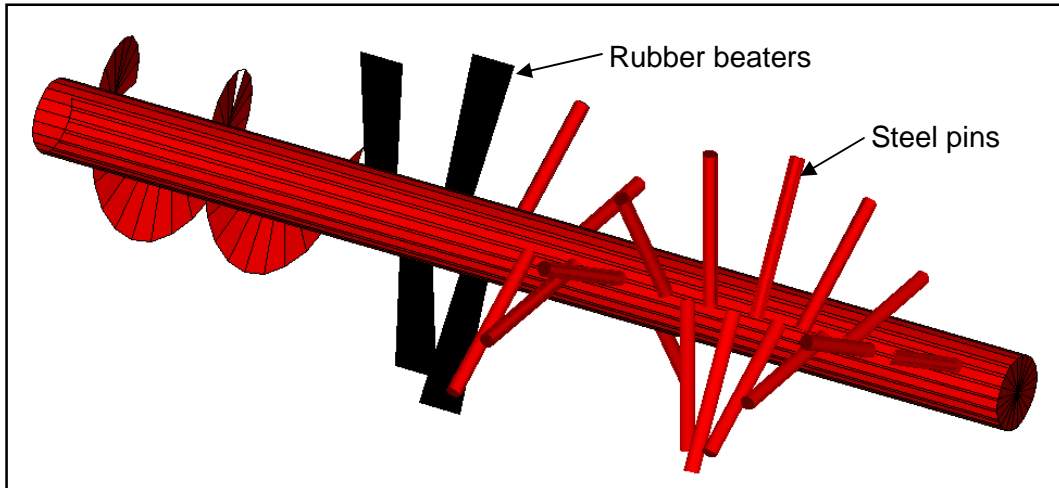
Figure 64 - The beater shaft of the destemmer showed in DEM. Note that some of the components are not showed correctly due to a graphics problem in PFC^{3D}.
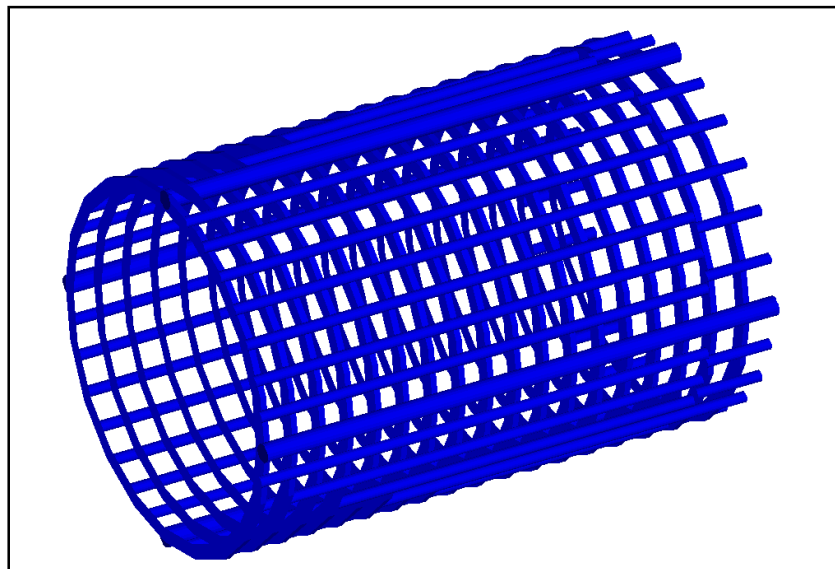
Figure 65 - The drum of the destemmer in the DEM model.

Building the drum posed the biggest challenge since its geometry is very complex. The drum used in the destemmer during the experiments was built from a number of circular aluminium castings (Figure 66). The castings consisted of pins that formed the square holes when assembled, assembly pins which are

63

larger than the normal pins, and a ring onto which the pins are mounted. It was found that the DEM model became too complex when each segment was built individually. Instead, a drum was built using long cylinders, that represented the entire row of pins from all the segments in the drum, and circular disks that represented the ring onto which the pins were mounted (Figure 65). The drum of the destemmer used two different segments with a different number of pins and pin lengths to create larger or smaller holes where the grapes could pass through. Two larger segments were used in the first part of the drum where the grapes entered the machine. The reason for this is explained in (Section 2.4.3.). The segments also had two small cams on the inside, located at 180° offset, which was not included in the DEM model in order to improve the computational efficiency of the model.
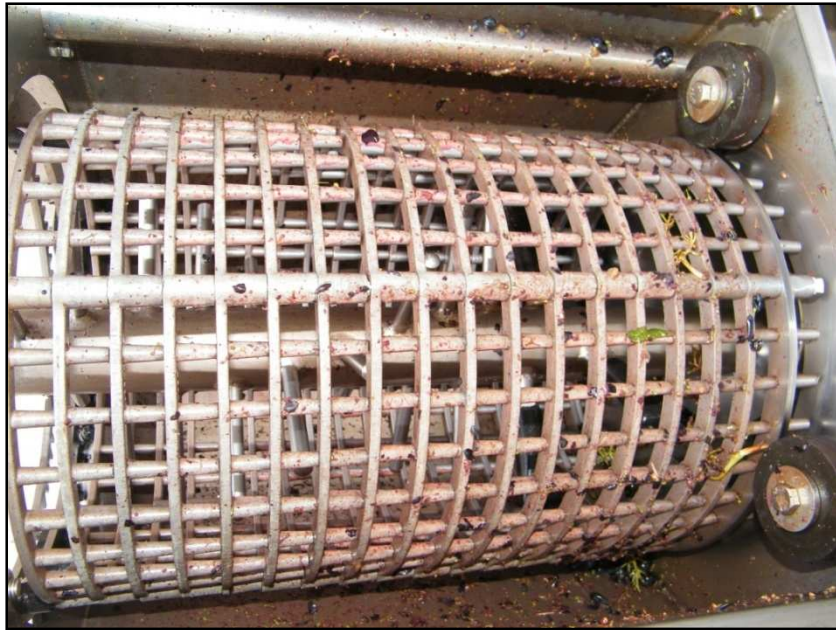
Figure 66 - The drum of the destemmer used in the experiments, shown here installed in the machine, with the grapes being fed into the machine from the right hand side.

All the dimensions and geometry of the important components of the destemmer were built exactly according to the destemmer that was used. These components included the feedtrough, entry and exit openings. For the rest of the components, some simplifications were used (Figure 63).

4.5.2. Running of Simulations

The DEM program used for the simulations, PFC^{3D}, allows models to be saved and restored again, but does not allow for two models to be incorporated into each other. As a result, all the bunches that would be simulated in the destemmer, had to be built at the start of the simulation. The bunches could not be built while the simulation was already running since the bunches must first be allowed to relax and bond strengths had to be adjusted.

The first step of the simulation was to build the destemmer model. The bunches that would be used in the simulation were then created on top of each other, at a constant offset, above the feedtrough. The bunches were allowed to relax, and the bond strengths were reset, after which the bunches were allowed to settle further.

To control the feed rate, the downward velocity of the first ball in the main stem of all the bunches was set to a calculated downward velocity. This velocity was calculated using the total weight of all the bunches, the feed rate specified and the position of the bunches. As soon as the bunches reached a specified height above the feedtrough, the specified constant velocity of the first ball in the main stem was removed and the bunch was allowed to fall freely under the influence of gravity. After the downward velocity of the bunches was set, the rotation of the beater shaft and drum was set.

The destemmed berries were collected in a collection bin similar to that used in the experiments. The bin was located beneath the destemmer body and had five separate sections. The stems were collected at the stem discharge in an enclosed collection bin. The data was obtained by weighing the berries and stems in the collection bins and comparing it to the experimental data.

4.5.3. Results
The grape bunches were fed into the destemmer at approximately 200 g/s, but it was difficult to determine the feed rate of the simulation. Since only five bunches were used in the simulation, there were no constant flow of grapes through the machine as in the experiments. All the grapes entered the destemmer quickly and were then destemmed. In the experiment, more grapes were fed over a longer time duration and there were a constant flow of grapes through the machine.

The rotation speed of the machine in the simulation was set equal to speed setting number 8 in the experiments. The distribution of the berries as it exits the destemmer was recorded in the simulation, like in the experiments (Figure 68) and the percentage of berries in each subdivision was calculated. These results are compared to experimental results where the grapes were fed at a rate of 230 g/s at rotation speed setting 8. These conditions are nearly identical to the simulated conditions.

The resultant distribution of the simulation compared very well to the applicable experiment, shown in Figure 67. Not only did the simulated results show a similar distribution of the berries, but the concentration of the berries was also very similar.
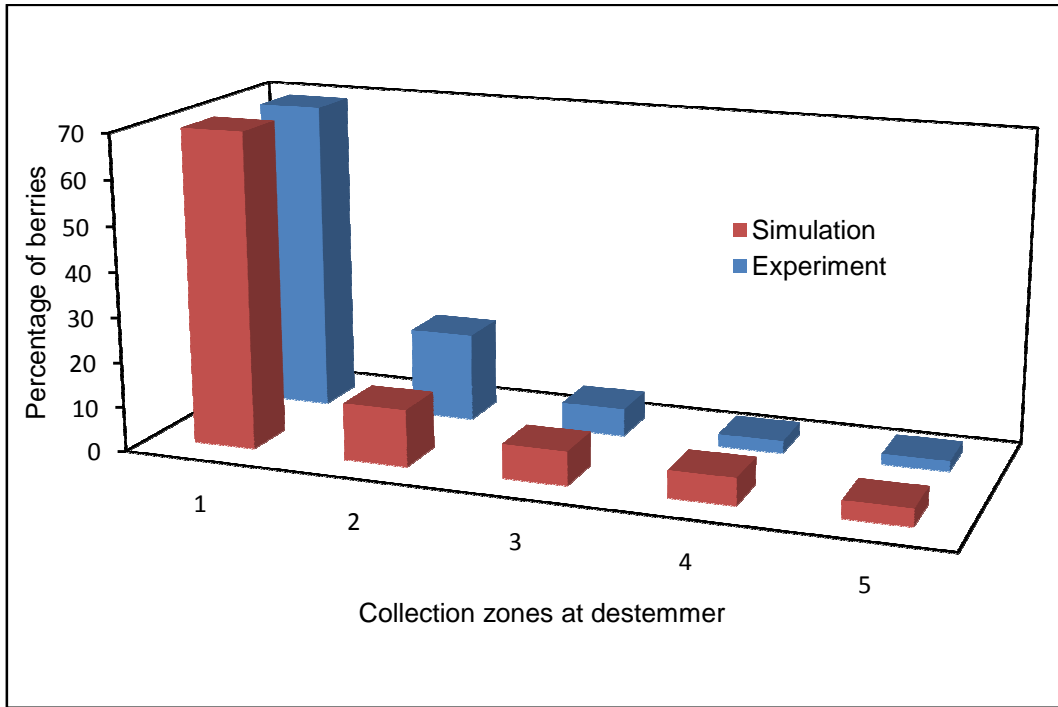
Figure 67 - Simulation and experimental results for the berry distribution from the destemmer.
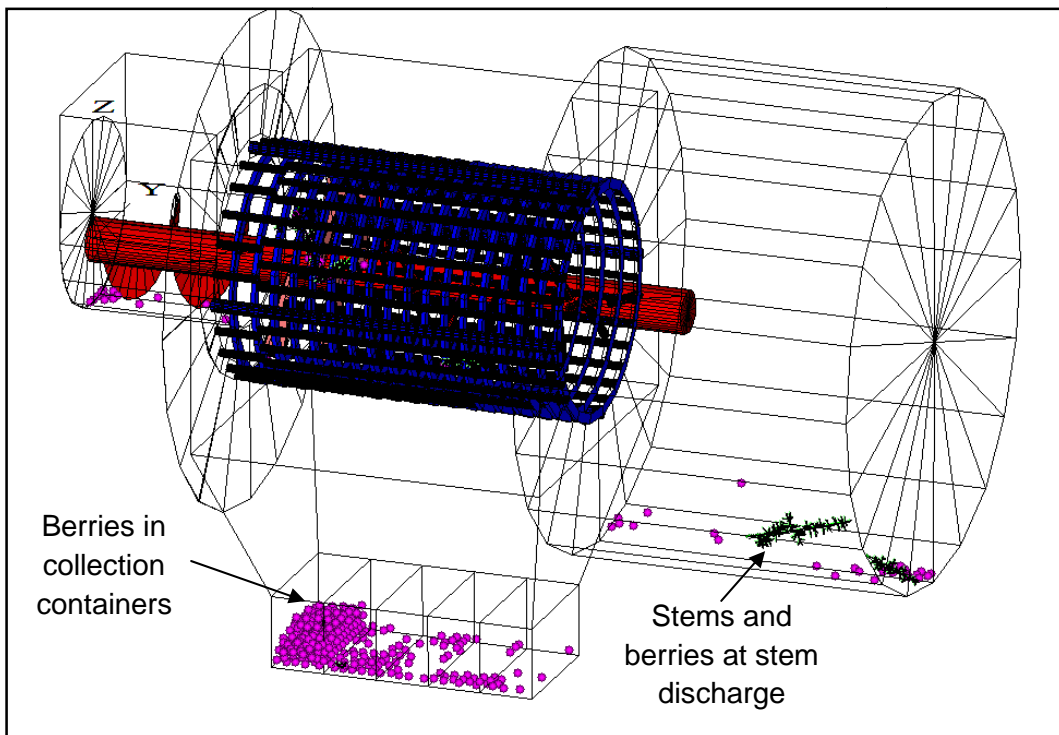
Figure 68 - A view of the DEM model of the destemmer at the end of the simulation. The beater shaft and drum are shown while all the other components are transparent.

66

The visual results obtained from the simulation also gave good insight into the destemming process. The removal of the berries from the stems and the separation of the berries from the stems could be tracked closely by using the visual results. The movement of the stems through the machine could also be studied and two of the five stems exited the machine at the stem discharge during the simulated time (Figure 68). The main objective of the simulation was to study the removal and separation of the grapes from the stems. For this reason the simulation was stopped once the majority of the berries had been removed. At that stage, not all the stems exited the machine yet, but the movement of the stems through the machine was very realistic. The total time simulated was 5.4 s.

Also, a small number of berries also exit with the stems at the stem discharge (Figure 68). Like in the experiments, this number of berries was divided by the number of bunches and the result was that 5 berries per bunch exited with the stems.

Figure 69 shows 6 pictures created during the simulation. The drum is not shown in these pictures to study the interaction between the grapes and the beater shaft more closely. The first picture shows the feeding of the bunches into the destemmer. In the second picture, all the bunches have entered the beater shaft and drum section of the destemmer. In this picture the removal of a large number of berries can clearly be seen. Less berries are still connected to the stems in picture 3 and one stem is already starting to move towards the stem discharge. Plenty of berries are still being separated from the stems. The first stem exits the destemmer in picture 4 and the number of berries leaving the machine has also decreased. Picture 5 shows the next stem exiting at the stem discharge and even less berries are exiting the machine. Picture 6 is the last picture of the simulation. No berries are being removed from the stems anymore and the third stem can be seen on its way to the stem discharge.

The results from the destemmer simulation showed very good correlation with the experimental results. The visual results obtained from the simulation showed very realistic behaviour of the grapes during the destemming process and compared well to the observed working of the destemmer during the experiments.
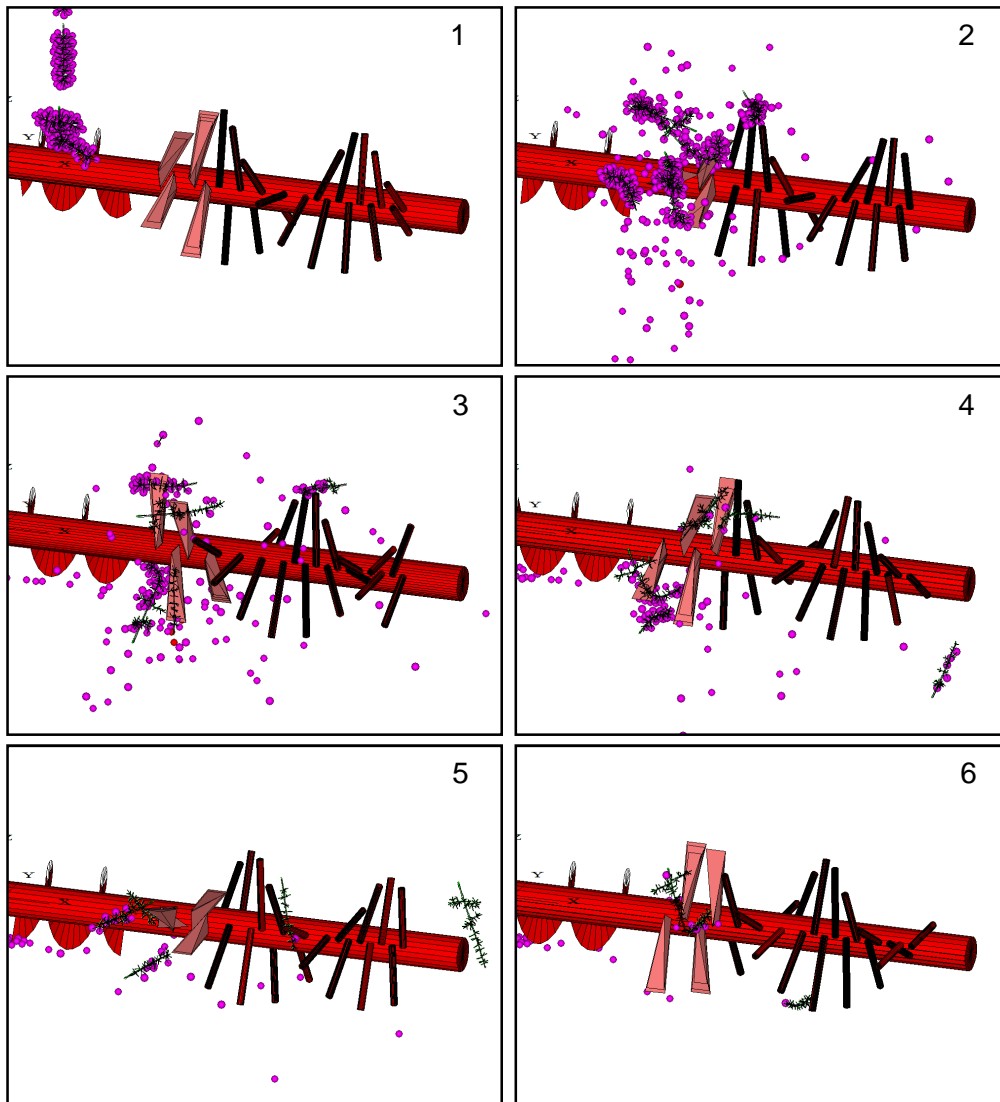
Figure 69 - The DEM simulation of the destemmer. Pictures are shown at intervals of 1 second.

4.6. Conclusions

It was shown that it is possible to build a grape bunch using only balls in DEM. The bunches were build in four basic steps: first the main stem, secondly the side stems, third the groups of pedicels and finally the berries. Before the bunches could be used for simulation of the destemming process, the bond strengths were increased and the bunches were allowed to relax under gravity. This step should be seen as part of the building process of the bunches. The dimensions and layout of the bunches created in the simulation compared very well to the grape bunches used in the experiments. The material properties that were determined experimentally were used as initial values for the bunch properties.

The simulation of the beater experiment was used as a calibration method of the bunches under destemming conditions. This was necessary since the initial

material properties of the bunches were determined at low speeds and the beater experiment were conducted at higher speeds. Due to the visco-elastic behaviour of bio-materials that was suggested in literature (Raji & Favier, 2004b), the bond strengths and stiffnesses had to be adjusted in the beater simulation to compensate for the visco-elastic effect. The material properties were basically adjusted to be accurate at the higher contact speeds. When the bunch properties had been calibrated, the behaviour of the grape bunch under destemming conditions could be simulated with good success and with good correlation to the experimental results.

A numerical model of the destemmer used in the experiments was build to investigate the ability of DEM to simulate an entire destemmer. The material properties of the grapes, as calibrated in the beater simulation, were used in the destemmer simulation. The results showed very good correlation to the experiments and a conclusion can be drawn that it is possible to simulate the destemming process using DEM. Further research should include the breaking of the stems and the amounts of stems ending up with the berries. As mentioned earlier, more research has first to be done to investigate the breaking mechanism of the side stems. In order to investigate stem breakage, more experimental data would also be required.

The lack of a visco-elastic contact and bond model in the DEM model hampered the simulations. The inclusion of such a model could further improve the correlation between the simulation results and the experimental results. The simulation could also be further improved by developing a special contact and bond model for the stems. Such a model would require more research into the behaviour of the stems.

5. Conclusions

The objectives of this study were to gain insight into the current destemming process, and the mechanics involved in the destemming of grapes through experiments and DEM simulations. Also, to investigate the ability of DEM to simulate the behaviour of grapes during the destemming process.

The material properties of the grapes were determined experimentally and the physical dimensions of the bunches, the stems and the berries were measured. An experimental setup of a simplified destemmer (beater experiment) was designed. The behaviour of the grapes during the destemming process could be observed from the captured high speed pictures and also by counting the number of berries removed from the stems. Good correlations were found between the number of berries removed, the weight of the bunch and the rotation speed of the beaters. It was found that with an increase in the bunch weight, the number of berries removed increased, while the percentage of berries removed decreased. With an increase in the beater speed, both the number and the percentage of berries removed increased.

Field tests on a commercial destemmer were conducted under various operating conditions. Different feed rates and rotation speeds were investigated. It was found that with an increase in feed rate and an increase in speed, more berries were accurately separated from the stems. It was also found that an average of 70% of the berries was removed in the first half of the machine. Only one batch of grapes was used and should data be needed for further research or commercial purposes, it is recommended that more samples be tested.

More research is needed regarding the behaviour of the stem under bending as well as a more accurate way of measuring the shearing of the side stems. The material properties should also be determined using higher speeds. The material properties of green-, rotten- and sunburnt-berries could also be a valuable addition to the current data. During the simplified destemmer experiments, it was observed that the stopper bar had a profound influence on the behaviour of the bunch. Replacing the stopper bar with a solid wall might eliminate this effect and improve the results from the experiments. The results from testing the commercial destemmer gave a good indication of the machine's performance, but more tests should be done using a wider range of feed rates. Also, an automated feeding mechanism should be used to achieve accurate feed rates. It is further recommended that larger test samples should be used to investigate stem breakage more accurately.

Five bunches were successfully built in DEM using the measured dimensions and shapes. The material properties measured during the experiments were all statistical data sets and only average values were used in the numerical model. Furthermore, the material properties were done at low speeds and the beater experiment involved higher speeds and as a result, the DEM material properties

70

had to be adjusted during the beater simulations. After the material properties were calibrated and multiple walls were implemented, the numerical results showed a good correlation with the experimental results and all trends could be modelled. During the calibration process of the bunch, the influence of various parameters on the bunch could be investigated. Finally, a numerical model of a commercial destemming machine was built. The model showed very realistic results and compared very well with the field measurements. In future, the model can be used to gain further understanding of the destemming process. Further development of the model, as well as more experimental data, is still necessary to accurately simulate stem breakage.

Due to the implementation of the contact model and the bond model in the software used, the stem's stiffness was higher under axial compression then under tension. Although the development of a special bond- and contact-model could improve the numerical results, such a model would be more computationally intensive. This, however, was not part of the objectives of this study. Since the current model is already very computationally intensive, it might be more practical to develop the current model further. Also, no data was available for the stem under bending conditions and as a result the stem could not be calibrated under bending.

The presence of visco-elastic behaviour was suggested by literature and various results indicated that including the visco-elastic effect in the numerical model could improve results even further. A visco-elastic bond model was not available and the development of such a model was outside the scope of this project. To further improve the model, green-, rotten- and sunburnt-berries could also be included.

The DEM model developed in this study can be used to further investigate the destemming process as well as new destemming methods. It is suggested that calibration and validation tests be done first since the model has not been tested under other destemming conditions. The model could also be of value when evaluating sorting methods. It is recommended that cohesion is included in the model when evaluating sorting methods. The cohesion will model the "sticky" effect of the juice. s

Appendix A: DEM Background and Theory

In this section the background and theory of DEM as implemented in PFC^{3D}, are discussed. It closely follows the PFC^{3D} manual (Itasca, 2003). The focus is on contact and damping models that were used in the simulations done during this study.

A.1. PFC^{3D} Particle Model

The particle model used in PFC^{3D} is also known as a soft contact model. Unlike other mechanical systems, the particles occupy a finite amount of space and are not only a point in space. The model consists of distinct particles that displace independently from each other and interact only at contact between particles. A finite stiffness is used to describe the measurable stiffness that exists at the contact, even though the particles are assumed to be rigid bodies. This is known as a soft contact. When most of the deformation in a physical system is accounted for by movements along the interfaces, assuming rigid particles is a good assumption. The mechanical behaviour of a system is described by the movement and interaction between the discrete particles and the inter-particle forces involved. To describe the motion and forces between the particles, Newton's laws of motion are used.

By allowing particles to be bonded together, more complex systems can be modelled. The bonds allow the formation of tensile forces between the particles. The model used in PFC^{3D} further assumes that contact occurs over a vanishingly small point and that particles are allowed to overlap one another at contact points. The force displacement law is used to relate the magnitude of the overlap to the contact force and all overlaps are assumed to be small. All particles are spherical.

In PFC^{3D} the particles are referred to as "balls" and PFC^{3D} also includes "walls". The walls act by defining velocity boundary conditions for the balls. The interaction between balls and walls is defined by the forces that arise from the contact between them. Although the equations of motion are satisfied for each ball, it is not satisfied for any of the walls. The motion of the walls remains constant regardless of forces acting upon it and no contact forces are formed between walls.

A.2. Equations of Motion

The equations of motion of discrete elements will be discussed in two parts: first the force displacement relation, followed by the laws of motion.

A.2.1. Force-Displacement Relation

The force displacement law describes the relation between the deformation of a body and the force related to that deformation. This deformation occurs at a contact point and the force related to that deformation is also known as the

contact force. The contact point ($x_i^{[C]}$) lies on a contact plane and is defined by a unit normal vector (n_i). This contact point is located inside the defined volume of a ball. For ball-ball contact, the contact point will be located on the line between the two ball centres, while for ball-wall contact, the contact point will be located on the line that defines the shortest distance between the ball centre and the surface of the wall.

The force is described using two components: the normal and shear components. The normal force component is inline with the normal vector of the contact plane while the shear force component is inline with the contact plane and acts at the contact point. These two force components are used in the force displacement law to determine the relative displacements by using the normal and shear stiffnesses. The notation for ball-ball contact is shown in Figure 70.
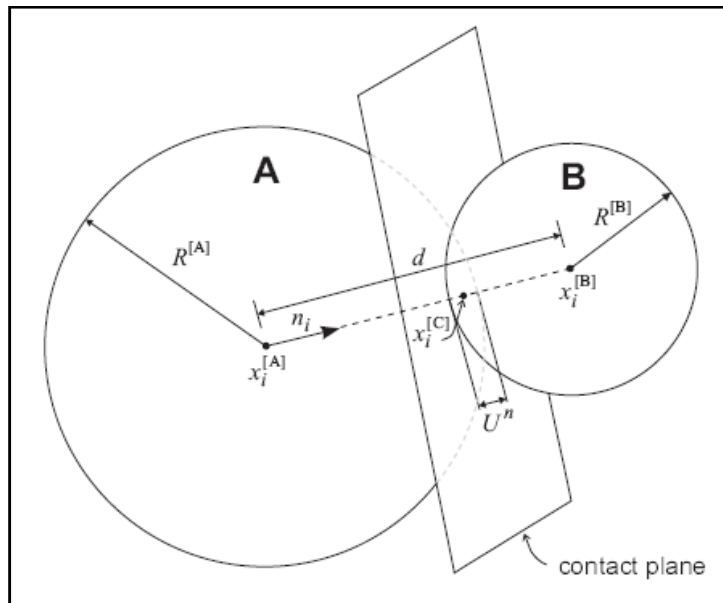
Figure 70 - Ball-ball contact, showing the notation used.

The unit normal vector used to define the contact plane during ball-ball contact, is given in equation 9 where ($x_i^{[A]}$) and ($x_i^{[B]}$) are the position vectors of balls A and B and d is the distance between their centres.

$$n_i = \frac{x_i^{[B]} - x_i^{[A]}}{d} \tag{9}$$

The distance between the centres of the balls (ball-ball contact only) is shown in equation 10.

$$d = \left| x_i^{[B]} - x_i^{[A]} \right| = \sqrt{\left(x_i^{[B]} - x_i^{[A]} \right)^2} \tag{10}$$

For ball-wall contact, the shortest distance between the centre of the ball and the wall is determined. If this distance is smaller than the radius of the ball, the

particular ball is in contact with the wall. The general notation used for ball-wall contact is shown in Figure 71
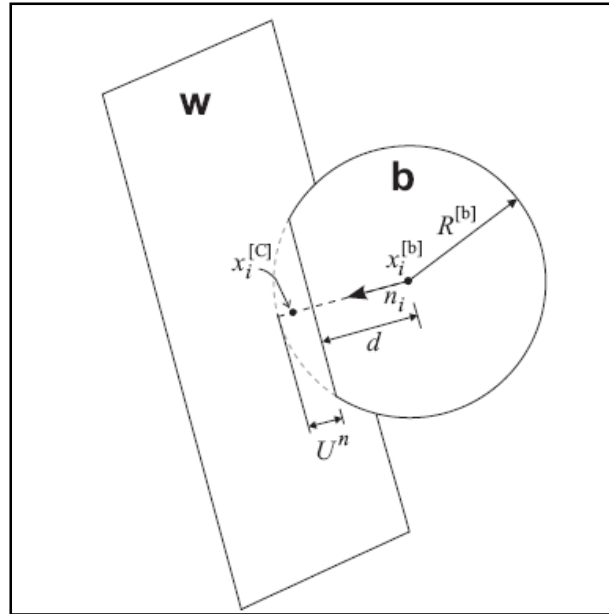
Figure 71 - Ball-wall contact, showing the notation used.

To determine the overlap (U^n) during a contact, the relative displacement at the contact point in the normal direction is calculated for ball-ball and ball-wall respectively. This is shown in equation 11.

$$U^n = \begin{cases} R^{[A]} + R^{[B]} - d & ball - ball \\ R^{[b]} - d & ball - wall \end{cases}$$

(11)

The location of the contact point can be given by equation 12 for ball-ball and ball-wall respectively.

$$x_i^{[C]} = \begin{cases} x_i^{[A]} + \left(R^{[A]} - \frac{1}{2}U^n \right) n_j & (ball - ball) \\ x_i^{[B]} + \left(R^{[B]} - \frac{1}{2}U^n \right) n_j & (ball - wall) \end{cases}$$

(12)

The contact force vector that represents the action that ball A has on ball B during a ball-ball contact, or the action that ball b has on the wall during a ball-wall contact is given by F_i. This force vector is divided in two components, a normal and a shear component, with respect to the contact plane as can be seen in equation 13 (F_i^n and F_i^s represent the normal and the shear components respectively).

$$F_i = F_i^n + F_i^s$$

(13)

Calculation of the normal contact force is shown in equation 14 where K^n represents the normal stiffness of the specific contact.

$$F_i^n = K^n U^n n_i \tag{14}$$

It should be noted that the normal stiffness (K^n) relates total displacement and force as opposed to the shear stiffness (K^s) that relates incremental displacement and force. The shear contact force is computed using the incremental method.

The computation of the shear contact force starts by initializing the shear contact force to zero at the start of contact. With each relative shear displacement increment that results in an increment of elastic shear force, this increment is added to the current value. Throughout the procedure, the motion of the contact should be considered. This is done by updating n_i and $x_i^{[C]}$ at every timestep. Since F_i^s is used to determine the contact force vector, F_i^s must also be updated at every timestep. Updating required the calculation of the rotation about the line common to the old and new contact plane as well as calculating the rotation about the new normal direction. The calculation of these two rotations is given in equation 15 and 16 respectively and it is assumed that the rotations are small.

$$\{F_i^s\}_{rot.1} = F_j^s \left(\delta_{ij} - e_{ijk} e_{kmn} n_m^{[old]} n_n \right) \tag{15}$$

$$\{F_i^s\}_{rot.2} = \{F_j^s\}_{rot.1} \left(\delta_{ij} - e_{ijk} \langle \omega_k \rangle \Delta t \right) \tag{16}$$

In equation 15, $n_m^{[old]}$ is the old unit normal to the contact plane. $\langle \omega_k \rangle$ represents the average angular velocity of the two contacting entities about the new normal direction and is given below in equation 17 where $\omega_i^{[\Phi j]}$ is the rotational velocity.

$$\langle \omega_j \rangle = \frac{1}{2} \left(\omega_j^{[\Phi 1]} + \omega_j^{[\Phi 2]} \right) n_j n_i \tag{17}$$

The relative velocity between ball A and ball B at the point of contact, in a ball-ball contact, is known as the contact velocity. For ball-wall contact, the contact velocity is defined by the relative velocity between the ball and the wall at the point of contact. The contact velocity is calculated in equation 18.

$$V_i = \left(\dot{x}_i^{[C]} \right)_{\Phi 2} - \left(\dot{x}_i^{[C]} \right)_{\Phi 1}$$

$$= \left(\dot{x}_i^{[\Phi 2]} + e_{ijk} \omega_j^{[\Phi 2]} \left(x_k^{[C]} - x_k^{[\Phi 2]} \right) \right) - \left(\dot{x}_i^{[\Phi 1]} + e_{ijk} \omega_j^{[\Phi 1]} \left(x_k^{[C]} - x_k^{[\Phi 1]} \right) \right) \tag{18}$$

Just like the contact forces, the contact velocity is resolved into the normal and shear components with respect to the contact plane. V_i^n and V_i^s are used for the normal and shear components respectively. The shear velocity is shown in equation 19.

$$V_i^s = V_i - V_i^n = V_i - V_j n_j n_i \tag{19}$$

In order to calculate the shear elastic force-increment vector (equation 21), the shear component of the contact displacement-increment vector that occurs over

a timestep of Δt, is first calculated (equation 20). In equation 21, k^s is the shear stiffness at the contact.

$$\Delta U_i^s = V_i^s \Delta t \tag{20}$$

$$\Delta F_i^s = -k^s \Delta U_i^s \tag{21}$$

To find the new shear contact force, the old shear contact force existing at the beginning of the timestep and the shear elastic force-increment is added as shown in equation 22. The old shear force vector at the beginning of the timestep is first rotated, to account for the motion of the contact plane, before the shear elastic force-increment is added.

$$F_i^s = \{F_i^s\}_{rot.2} + \Delta F_i^s \tag{22}$$

In order to satisfy the contact constitutive relations, the values of the normal and shear contact forces in equations 14 and 22 are modified. The contribution of the final contact force to the resultant force and moment in contact is given in equation 23 to 26. In these equations, $F_i^{[\Phi]}$ and $M_i^{[\Phi]}$ indicate the force and moment sums for entity Φ^j.

$$F_i^{[\Phi^1]} \leftarrow F_i^{[\Phi^1]} - F_i \tag{23}$$

$$F_i^{[\Phi^2]} \leftarrow F_i^{[\Phi^2]} - F_i \tag{24}$$

$$M_i^{[\Phi^1]} \leftarrow M_i^{[\Phi^1]} - e_{ijk}\left(x_j^{[C]} - x_j^{[\Phi^1]}\right)F_k \tag{25}$$

$$M_i^{[\Phi^2]} \leftarrow M_i^{[\Phi^2]} - e_{ijk}\left(x_j^{[C]} - x_j^{[\Phi^2]}\right)F_k \tag{26}$$

A.2.2. Law of Motion

A single rigid particle's motion is determined by the resultant force and moment vectors that act upon it and this motion can then be described as the translational movement of a single point and the rotational motion of the particle. The point that is used to describe the translational movement is the centre of mass of the particle. In DEM, this is also the geometric centre of the particle. The translational motion of this point can be described by the position (x_i), velocity ($\dot{x}_i$) and acceleration ($\ddot{x}_i$). The rotational motion of the particle is described by the angular velocity (ω_i) and angular acceleration ($\dot{\omega}_i$).

The equation of motion can be divided in to two vector equations: 1) The relation between the resultant forces and the translational motion, and 2) the relation between the resultant moments and the rotational motion. These two equations are given in equations 27 and 28 respectively, where F_i is the resultant force that acts on the particle, m is the mass of the particle, g is gravity, M_i is the resulting moment acting on the particle and H_i the angular momentum of the particle.

$$F_i = m(\ddot{x}_i - g_i) \tag{27}$$

$$M_i = \dot{H}_i \tag{28}$$

If the rotations of the particle are aligned with the principal axis, then equation 28 reduces to Euler's equation of motion as shown in equation 29, 30 and 31. In these equations I_1, I_2 and I_3 represent the principle moments of inertia, ω_1, ω_2 and ω_3 the angular accelerations about the principle axis and M_1, M_2 and M_3 the components of the resultant moment referred to the principle axis.

$$M_1 = I_1\dot{\omega}_1 + (I_3 - I_2)\omega_3\omega_2 \tag{29}$$

$$M_2 = I_2\dot{\omega}_2 + (I_1 - I_3)\omega_1\omega_3 \tag{30}$$

$$M_3 = I_3\dot{\omega}_3 + (I_2 - I_1)\omega_2\omega_1 \tag{31}$$

Since the centre of mass coincides with the centre of mass of the particles (spheres), any local axial system attached to the centre of mass is a principle-axis system and, as a result, the three principle moments of inertia are equal. This simplifies equations 29, 30 and 31 to equation 32.

$$M_i = I\dot{\omega}_i = \left(\frac{2}{5}mR^2\right)\dot{\omega}_i \tag{32}$$

Equations 28 and 32 are integrated by using a centred finite difference involving a timestep Δt. Velocity and angular velocity are calculated at mid-intervals of $t \pm n\Delta t/2$. Position, acceleration, angular acceleration and the resultant force and moment are calculated at primary intervals of $t \pm n\Delta t$.

The translational and rotational accelerations at time t are described in terms of the velocity values at mid-intervals in equations 33 and 34.

$$\ddot{x}_i^{(t)} = \frac{1}{\Delta t}\left(\dot{x}_i^{(t+\frac{\Delta t}{2})} - \dot{x}_i^{(t-\frac{\Delta t}{2})}\right) \tag{33}$$

$$\dot{\omega}_i^{(t)} = \frac{1}{\Delta t}\left(\omega_i^{(t+\frac{\Delta t}{2})} - \omega_i^{(t-\frac{\Delta t}{2})}\right) \tag{34}$$

When equations 33 and 34 are inserted into equations 27 and 32, the velocities can be solved at time $t + \Delta t/2$, as shown in equations 35 and 36.

$$\dot{x}_i^{(t+\frac{\Delta t}{2})} = \dot{x}_i^{(t-\frac{\Delta t}{2})} + \left(\frac{F_i^{(t)}}{m} + g_i\right)\Delta t \tag{35}$$

$$\omega_i^{(t+\frac{\Delta t}{2})} = \omega_i^{(t-\frac{\Delta t}{2})} + \left(\frac{M_i^{(t)}}{m}\right)\Delta t \tag{36}$$

These calculated velocities are used in equation 37 to update the position of the particle centre.

$$x_i^{(t+\Delta t)} = x_i^t + \dot{x}_i^{(t+\frac{\Delta t}{2})}\Delta t \tag{37}$$

A.3. Contact Models

A contact model consists of three models, namely the slip model, the stiffness model and the bonding model. The slip model specifies the equivalent DEM model the relation between the shear and normal contact forces when two balls, or a ball and a wall, are in contact and this will determine the slip between the two balls, or the ball and the wall. The stiffness model provides an elastic relation between the contact force and the relative displacement. The third model, the bonding model, uses bond strength limits to limit the maximum normal and shear forces in a contact.

A.3.1. Contact Stiffness Models

PFC^{3D} provides two types of contact stiffness models: a linear model and a simplified Hertz-Mindlin model. Contact between these two models is undefined and as a result, such contact is not allowed. Bonding is also not allowed when using the Hertz model since it is undefined under tensile forces.

The contact stiffness model relates the contact force and relative displacement in the normal and shear direction using equations 38 and 39 respectively.

$$F_i^n = K^n U^n n_i \tag{38}$$

$$\Delta F_i^s = -k^s \Delta U_i^s \tag{39}$$

Since the normal stiffness relates the normal force to the normal displacement, it is a secant stiffness. The shear stiffness relates the increment of shear force to the increment of shear displacement and as a result is a tangent stiffness. Both these stiffnesses are assigned different values depending on the contact stiffness model used.

<u>Linear Contact Model</u>

The normal and shear stiffnesses of the contacting entities are specified separately in the linear contact model. The contact stiffnesses are computed by assuming that the stiffnesses of the contacting entities act in series. The contact normal secant stiffness and contact shear stiffness are given in equations 40 and 41 respectively, where [A] and [B] denotes to the two contacting entities.

$$K^n = \frac{k_n^{[A]}k_n^{[B]}}{k_n^{[A]}+k_n^{[B]}} \tag{40}$$

$$k^s = \frac{k_s^{[A]} k_s^{[B]}}{k_s^{[A]} + k_s^{[B]}} \tag{41}$$

In the linear contact model, the normal secant stiffness (k_n) is equal to the normal tangent stiffness, as shown in equation 42.

$$k^n \equiv \frac{dF^n}{dU^n} = \frac{d(K^n U^n)}{dU^n} = K^n \tag{42}$$

Hertz-Mindlin Contact Model

The Hertz-Mindlin contact model is based on an approximation of the theory of Mindlin and Deresiewicz and is a non-linear contact model. Two parameters are defined to determine the contact stiffness, namely: the shear modulus [G] and Poisson's ratio [v].

The contact normal secant stiffness and the contact shear tangent stiffness in the Hertz-Mindlin contact model are given in equations 43 and 44 respectively.

$$K^n = \left(\frac{2\langle G \rangle \sqrt{2\tilde{R}}}{3(1 - \langle v \rangle)} \right) \sqrt{U^n} \tag{43}$$

$$k^s = \left(\frac{2\left(\langle G \rangle^2 3(1 - \langle v \rangle)\tilde{R}\right)^{1/3}}{2 - \langle v \rangle} \right) |F_i^n|^{1/3} \tag{44}$$

It is important to note that during ball-ball contacts, the elastic properties are taken as mean values and during ball-wall contact, the wall is treated as rigid and the elastic properties of the ball are used. In equation 43 and 44, the multipliers are a function of the material and geometric properties of the two contacting entities. For ball-ball contact, the multipliers are given by equations 45, 46 and 47, and for ball-wall contact, the multipliers are given by equations 48, 49 and 50. In all these equations R represents the ball radius.

$$\tilde{R} = \frac{2R^{[A]} R^{[B]}}{R^{[A]} + R^{[B]}} \tag{45}$$

$$\langle G \rangle = \frac{1}{2}\left(G^{[A]} + G^{[B]} \right) \tag{46}$$

$$\langle v \rangle = \frac{1}{2}\left(v^{[A]} + v^{[B]} \right) \tag{47}$$

$$\tilde{R} = R^{[ball]} \tag{48}$$

$$\langle G \rangle = G^{[ball]} \tag{49}$$

$$\langle v \rangle = v^{[ball]} \tag{50}$$

In the Hertz-Mindlin contact model, the normal secant stiffness (k_n) is equal to the normal tangent stiffness, as shown in equation 51.

$$k^n \equiv \frac{dF^n}{dU^n} = \frac{2}{3}K^n \tag{51}$$

A.3.2. Slip Model

The slip model is an intrinsic property if the two contacting entities allow slip to occur by limiting the shear force. The slip model provides no normal strength and is always active, except when a contact bond is present, which supersedes the slip model. A parallel bond and the slip model can be active simultaneously.

The slip model is defined by the friction coefficient (μ) at the contact. This friction coefficient is taken to be the minimum friction coefficient between the two contacting entities. The first step in the slip model is to check the overlap between two balls or between a ball and a wall. If the overlap is less or equal to zero, there is no contact and the no-normal strength criterion is enforced by setting the normal and shear forces to zero. If contact is detected, the maximum allowable shear contact force is calculated using equation 52.

$$F_{max}^s = \mu |F_i^n| \tag{52}$$

If equation 53 is true, then slip is allowed to occur by equation 54.

$$|F_i^s| > F_{max}^s \tag{53}$$

$$F_i^s \leftarrow F_i^s \left(F_{max}^s \Big/ |F_i^s| \right) \tag{54}$$

A.3.3. Bonding Models

Two bonding models are available in PFC[3D] namely: the contact bond model and the parallel bond model. These bonds can be described as a kind of glue between the particles. These two bonding models differ in the sense that the glue area of the contact bond model is of a vanishingly small size that only acts at the contact point and as a result, it can only transmit a force. The glue area of the parallel bond is of finite size that acts over the circular cross section that lies between the particles and as a result, the parallel bond can transmit a force and a moment.

These two bonding models can be active simultaneously, but it should be noted that the presence of a contact bond overrides the slip model. Bonds can only be formed between particles and not between particles and walls. Once a bond is formed at a contact between two particles, that contact will remain until the bond is broken. The bond will be broken when the normal or shear force in the bond exceed the maximum allowable force.

The Contact Bond Model

A contact bond can be envisioned as either a point of glue, or as a pair of elastic springs with a constant stiffness in both the normal and the shear direction and acting at the contact point. The presence of a contact bond eliminates the possibility of slip occurrence, which means that the shear force can exceed the normal force. Instead, the magnitude of the shear force is limited by the strength of the contact bond in the shear direction. Contact bonds also allow the development of normal tensile forces between bonded particles. The magnitude of this normal tensile force is limited by the strength of the normal contact bond strength.

Only two parameters are defined in the contact bond model. The strength of the contact bond in the normal and shear directions are specified individually. If the magnitude of the normal or shear contact force exceeds the normal or shear contact bond strength respectively, the bond will be broken and both the normal and shear contact forces will be set to zero. However, if the bond fails under shear, the contact forces can remain unchanged if the shear force does not exceed the friction limit.
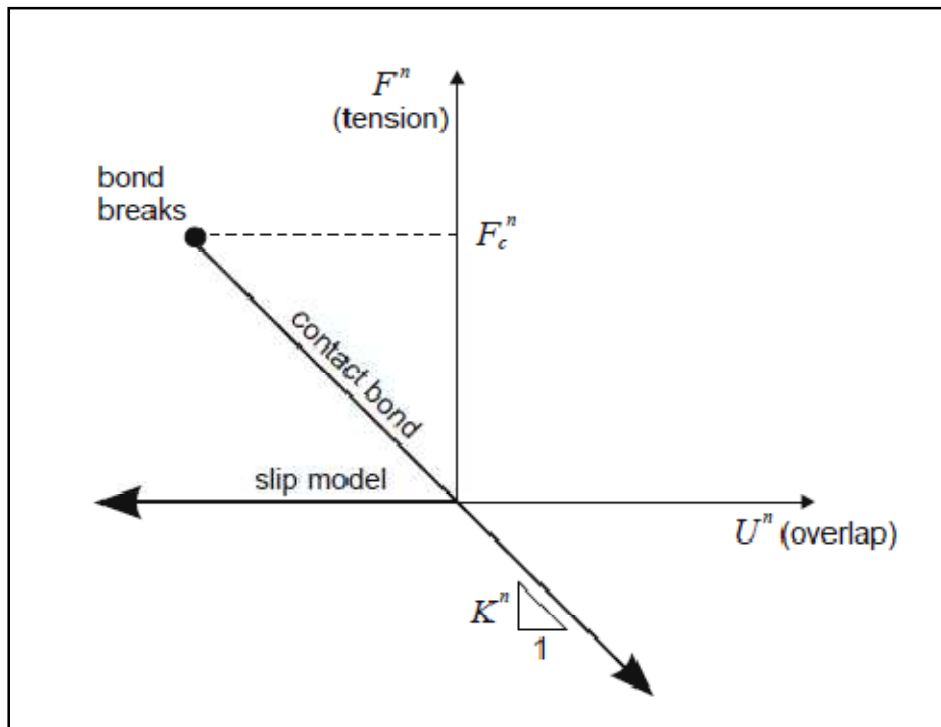

Figure 72 - The constitutive behaviour of the normal component of the contact force at a contact occurring at a point.

The constitutive behaviour relating the normal and shear components of a contact force and relative displacement for particle contact occurring at a point is shown in Figure 72 and Figure 73. Either the contact bond or the slip model is

active at any given time. Tension is indicated when the contact force (F^n) is bigger than zero. An overlap is indicated when the relative normal displacement (U^n) exceeds zero. The shear contact force is shown as F^s and the magnitude of the total shear displacement, measured relative to the location of the contact point when the contact was formed, is given by U^s. If a parallel bond is present, an additional force and moment may also be present.
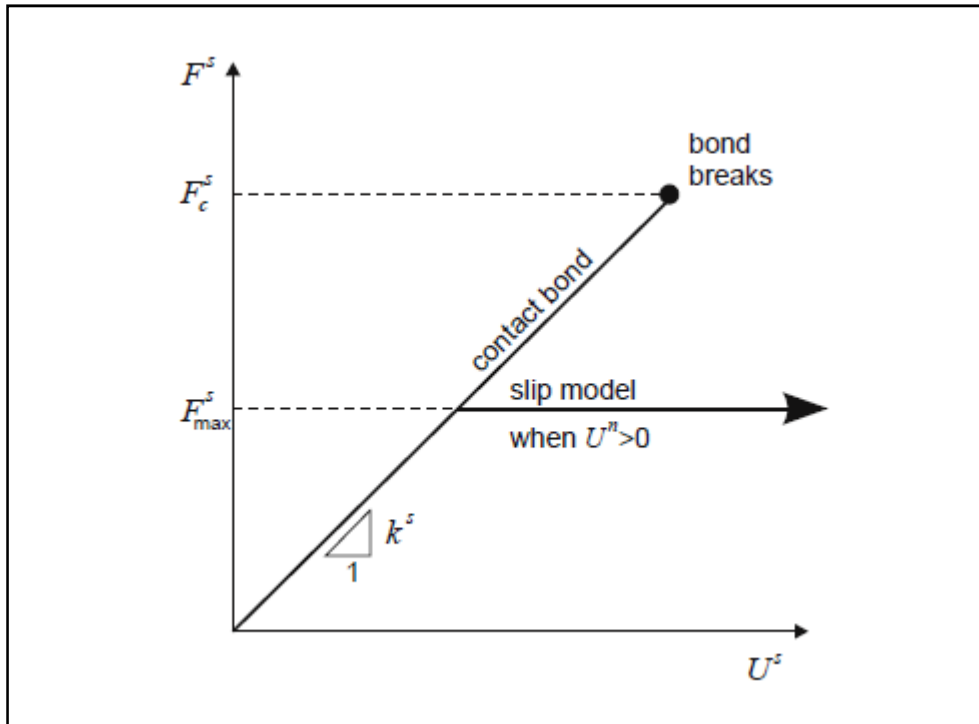

Figure 73 - The constitutive behaviour of the shear component of the contact force at a contact occurring at a point.

The Parallel Bond Model

The parallel bond describes the constitutive behaviour of a finite sized piece of bonding material located between two particles. This bond creates an elastic interaction between particles and acts in parallel with the contact bond and slip models. A parallel bond can transmit both force and moment and does not eliminate the occurrence of slip.

A parallel bond can be envisioned, like a contact bond, as a set of elastic springs with a constant stiffness in both the normal and the shear direction. However, instead of acting at a point like the contact bond, the springs are uniformly distributed over a circular disk lying on the contact plane, centred at the contact point. These springs act in parallel with the point contact springs that models the particle stiffness. The parallel bond stiffness causes a force and moment to develop as a result of relative motion at the contact, which is related to the two bonded particles. If the force in the normal or shear direction exceed the

82

specified maximum force in the normal or shear direction in the parallel bond respectively, the parallel bond will be broken.

Five parameters are used to define a parallel bond namely: the normal $(\overline{k^n})$ and shear stiffness $(\overline{k^s})$, the normal $(\overline{\sigma_c})$ and shear strength $(\overline{\tau_c})$, and the bond disk radius $(\overline{R})$. It is important to note the units in which these parameters are specified. Both stiffnesses are specified as [stress/displacement], both strengths as [stress] and the bond radius is dimensionless since it is only specified as a factor of the diameter of the smallest particle in the bond.
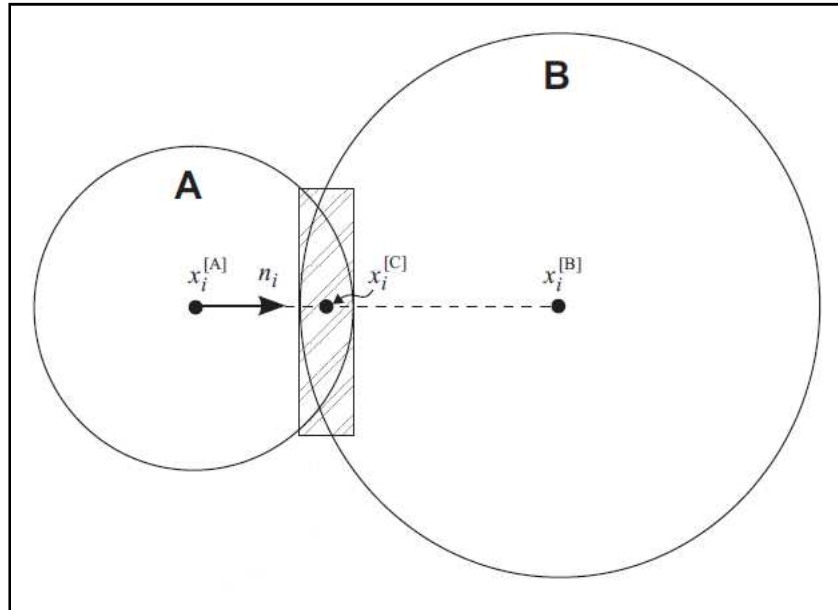

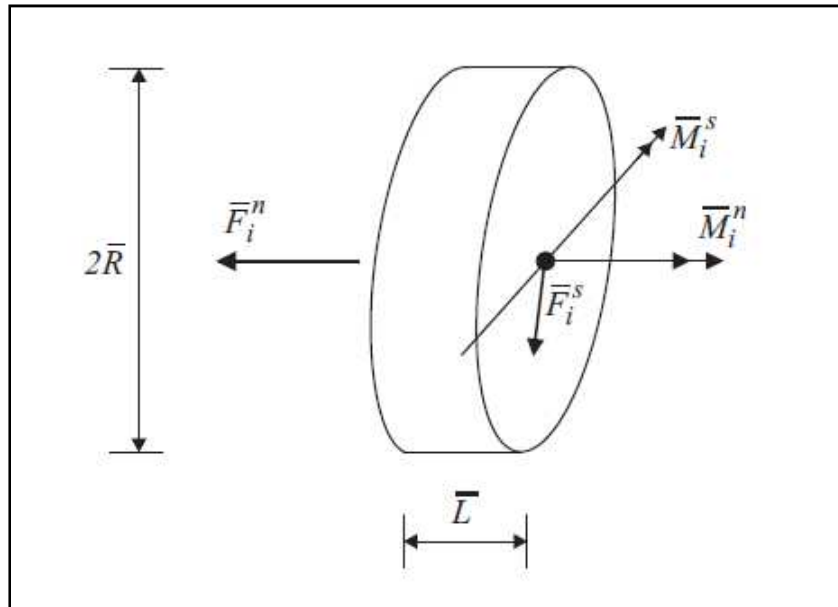Figure 74 - A visualised representation of a parallel bond between two particles.

Figure 75 - A parallel bond visualised as a cylinder of bonding material.

83

Equations 55 and 56 show the force and moment associated with a parallel bond where $\overline{F_i^n}$, $\overline{M_i^n}$ and $\overline{F_i^s}$, $\overline{M_i^s}$ represents the normal and shear component vectors respectively. These vectors are also shown in Figure 75. Here the parallel bond is depicted as a cylinder of elastic material. A convention is used that the force and moment associated with a parallel bond represents the action of the bond on sphere B in Figure 74. Both these vectors can be resolved into normal and shear components with respect to the contact plane.

$$\overline{F_i} = \overline{F_i^n} + \overline{F_i^s} \tag{55}$$

$$\overline{M_i} = \overline{M_i^n} + \overline{M_i^s} \tag{56}$$

The normal component vectors can be expressed as scalar values $\overline{F^n}$ and $\overline{M^n}$ in equations 57 and 58.

$$\overline{F_i^n} = \left(\overline{F_j}n_j\right)n_i = \overline{F^n}n_i \tag{57}$$

$$\overline{M_i^n} = \left(\overline{M_j}n_j\right)n_i = \overline{M^n}n_i \tag{58}$$

When a parallel bond is formed, $\overline{F^n}$ and $\overline{M^n}$ are set to zero. Every relative displacement and rotational increment at the contact results in an increment of the elastic force and moment, which are added to the current values. These elastic increments are calculated every timestep (Δt) as shown in equations 59 to 64.

$$\Delta\overline{F_i^n} = \left(-\overline{k^n}A\Delta U^n\right)n_i \tag{59}$$

$$\Delta\overline{F_i^s} = -\overline{k^s}A\Delta U_i^s \tag{60}$$

with $\Delta U_i = V_i\Delta t$ $\tag{61}$

$$\Delta\overline{M_i^n} = \left(-\overline{k^s}J\Delta\theta^n\right)n_i \tag{62}$$

$$\Delta\overline{M_i^s} = -\overline{k^n}I\Delta\theta_i^s \tag{63}$$

with $\Delta\theta_i = \left(\omega_i^{[B]} - \omega_i^{[A]}\right)\Delta t$ $\tag{64}$

In equations 59 to 64 the contact velocity is given by V_i while the area of the bond disk (A), the polar moment of inertia of the cross section of the disk (J), and moment of inertia of the cross section of the disk about an axis through the contact point and in the direction of $\Delta\theta_i^s$, (I), are given in equations 65, 66 and 67.

$$A = \pi\overline{R^2} \tag{65}$$

$$J = \frac{1}{2}\pi\overline{R^4} \tag{66}$$

84

$$I = \frac{1}{4}\pi \overline{R}^4 \tag{67}$$

By adding the elastic force and moment increment vectors to the old force and moment vectors, the new force and moment vectors are found. The new force and moment vectors are shown in equations 68 to 71. In equations 69 and 71 $\{ \quad \}_{rot.2}$ denotes to the update that accounts for the motion of the contact plane.

$$\overline{F}_i^n \leftarrow \overline{F}^n n_i + \Delta \overline{F}_i^n \tag{68}$$

$$\overline{F}_i^s = \left\{ \overline{F}_i^s \right\}_{rot.2} + \Delta \overline{F}_i^s \tag{69}$$

$$\overline{M}_i^n \leftarrow \overline{M}^n n_i + \Delta \overline{M}_i^n \tag{70}$$

$$\overline{M}_i^s = \left\{ \overline{M}_i^s \right\}_{rot.2} + \Delta \overline{M}_i^s \tag{71}$$

Beam theory is used to calculate the maximum tensile and shear stresses acting on the bond. These stresses are calculated in equations 72 and 73.

$$\sigma_{max} = \frac{-\overline{F}^n}{A} + \frac{|\overline{M}_i^s|}{I} \overline{R} \tag{72}$$

$$\tau_{max} = \frac{|\overline{F}_i^s|}{A} + \frac{|\overline{M}^n|}{J} \overline{R} \tag{73}$$

When either equations 74 (normal strength) or 75 (shear strength) are true, the parallel bond will break.

$$\sigma_{max} \geq \overline{\sigma_c} \tag{74}$$

$$\tau_{max} \geq \overline{\tau_c} \tag{75}$$

If the bond does not break and remains intact, the contribution of the final force and moment vectors to the resultant force and contact moment on each of the spheres are given by equations 76 to 79 where $F_i^{[\Phi]}$ and $F_i^{[\Phi]}$ are the sums of the force and moment of sphere Φ.

$$F_i^{[A]} \leftarrow F_i^{[A]} - \overline{F}_i \tag{76}$$

$$F_i^{[B]} \leftarrow F_i^{[B]} - \overline{F}_i \tag{77}$$

$$M_i^{[A]} \leftarrow M_i^{[A]} - e_{ijk}\left(x_j^{[C]} - x_j^{[A]}\right)\overline{F_k} - \overline{M_i} \tag{78}$$

$$M_i^{[B]} \leftarrow M_i^{[B]} - e_{ijk}\left(x_j^{[C]} - x_j^{[B]}\right)\overline{F_k} - \overline{M_i} \tag{79}$$

A.4. Damping Models
The dissipation of energy in a system can be achieved through friction or by using damping. Friction is the most common way of energy dissipation, but when

the friction is not sufficient or not active in a model, damping is used to achieve steady state in a smaller number of cycles.

A.4.1 Non-viscous Local Damping

The local damping in PFC^{3D} works by adding a damping force term to the equations of motion. The damped equations of motion are shown by equations 80 and 81. In these equations, $\mathcal{F}_{(i)}$, $\mathcal{M}_{(i)}$ and $\mathcal{A}_{(i)}$ represents the generalised force, mass and acceleration components respectively. $\mathcal{F}_{(i)}$ includes the contribution of gravity and $F_{(i)}$ is the damping force, as shown in equation 82. Equation 84 shows the generalised velocity used in equation 82.

$$\mathcal{F}_{(i)} + F_{(i)}^d = \mathcal{M}_{(i)}\mathcal{A}_{(i)} \qquad i = 1\dots6 \tag{80}$$

$$\mathcal{M}_{(i)}\mathcal{A}_{(i)} = \begin{cases} m\ddot{x}_{(i)} & for\ i = 1\dots3 \\ I\dot{\omega}_{(i-3)} & for\ i = 4\dots6 \end{cases} \tag{81}$$

$$F_{(i)}^d = -\alpha|\mathcal{F}_{(i)}|sign(\mathcal{V}_{(i)}) \quad i = 1\dots6 \tag{82}$$

$$sign(y) = \begin{cases} +1 & if\ y > 0 \\ -1 & if\ y < 0 \\ 0 & if\ y = 0 \end{cases} \tag{83}$$

$$\mathcal{V}_{(i)} = \begin{cases} \dot{x}_{(i)} & for\ i = 1\dots3 \\ \omega_{(i-3)} & for\ i = 4\dots6 \end{cases} \tag{84}$$

The damping constant (α) controls the damping force. The damping constant is specified separately for each particle. This damping model has the advantage that only the accelerating motion is dampened and therefore no false damping forces arise from the steady state motion. Furthermore, the damping constant is non dimensional and since the damping is not frequency dependant, all the regions are dampened equally using the same damping constant, even if they have different natural frequencies.

A.4.2. Viscous Contact Damping

Normal and shear dashpots are added to each contact when viscous damping is used. The dashpots work in parallel with the contact model used. Figure 76 shows a linear contact model with viscous damping.

The normal and shear components of the damping force (D_i), which are added to the contact force, are shown in equation 85. The subscript i indicates the normal (n) or shear (s) directions, C_i are used for the damping constant and V_i for the relative velocity at the contact.
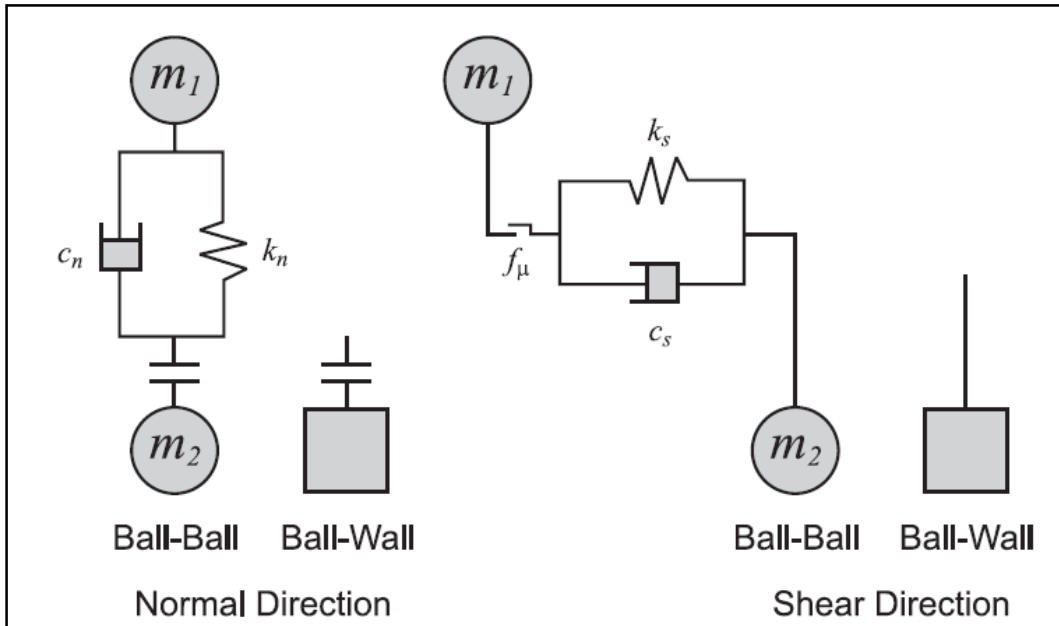
$$D_i = C_i|V_i| \tag{85}$$

Figure 76 - A linear contact model using viscous damping. Contact in the normal and shear directions are shown, as well as ball-ball and ball-wall contact.

Instead of specifying the damping constant directly, the critical damping ratio is specified, which satisfy the damping constants as shown in equation 86. In this equation, C_i^{crit} is the critical damping constant which is given in equation 87.

$$C_i = \beta_i C_i^{crit} \tag{86}$$

$$C_i^{crit} = 2m\omega_i = 2\sqrt{mk_i} \tag{87}$$

In equation 87, the natural frequency of the un-damped system is given by ω, the contact tangent stiffness by k_i, and the effective mass of the system by *m*. During ball-ball contact, the average mass of the two balls are used and in a ball-wall contact, the mass of the ball is used.

Viscous damping is characterised by the critical damping ratio, β. A system is critically damped when β=1. This means that the response decay to zero is at the fastest possible. The transition from oscillatory response to an exponentially decaying response, is also found at β=1. When β<1, the system is under-damped or lightly damped and an oscillatory response will be found. When β>1, the system is over-damped or heavily damped and an exponentially decaying response will be found.

When viscous damping is activated in PFC[3D], the timestep is reduced to ensure stability of the model. The new reduced timestep is calculated using the apparent stiffness, k_i', as shown in equation 88. In this equation, k_i represents the contact stiffness without any damping and the safety factor is given by α. Equation 89 shows the calculation of λ.

$$k_i' = \alpha \frac{k_i}{\left(\sqrt{1+\lambda_i^2} - \lambda_i\right)^2} \tag{88}$$

$$\lambda_i = \frac{c_i}{2k_i \Delta t_0} \tag{89}$$

In equation 89, c_i represents the critical damping, and the timestep, Δt_0, is calculated without viscous damping. The apparent stiffness in the normal and shear directions are used and the minimum timestep calculated is used.

Appendix B: Other Grape Processing Techniques

B.1. Other Types of Destemmers

The destemmers described above are not the only concept used for separating grape berries and stems, but they are used by the majority of wine cellars. Vertical destemmers work on the same basic principle and are also centrifugal type destemmers but the drum and beater shaft are positioned vertically instead of horizontally. These machines are not very popular and currently only one manufacturer, Imma, could be found that builds vertical destemmers (Figure 77).

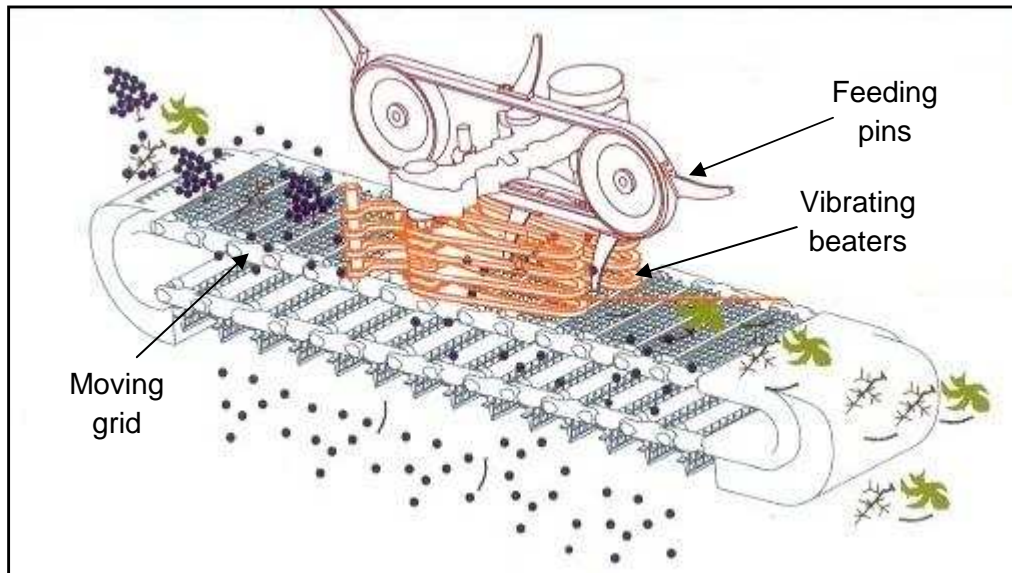Figure 77 - Two vertical destemmers from Imma (Imma, 2010).

Figure 78 - A linear destemmer from Pellenc called Selectiv' Process Winery (Pellenc, 2010).

Linear destemmers (Figure 78) have only recently been introduced and were developed by a company, called Pellenc, which build mechanical grape

harvesters. A linear destemmer can be described as a scaled down, stationary grape harvesting machine since it uses the same basic principles. The grape berries are removed from the stems by two similar sets of vibrating beaters used by mechanical grape harvesting machines (See Section B.3.). The grape bunches are fed through these beaters by a set of feeding pins while a moving grid acts as a conveyor for the grapes (Figure 78). The moving grid also doubles as a sieve to remove the majority of the berries. The remaining berries and all the stems are then separated by two sets of rollers that act as two sieves (Figure 79). The first set of rollers have small gaps to eliminate green berries and small pieces of stems, while the second set of rollers have gaps just large enough for the berries to pass through, but the stems and leaves move over the rollers.

Figure 79 - The two sets of rollers used to separate the stems and berries on the Selectiv' Process Winery (Pellenc, 2010).
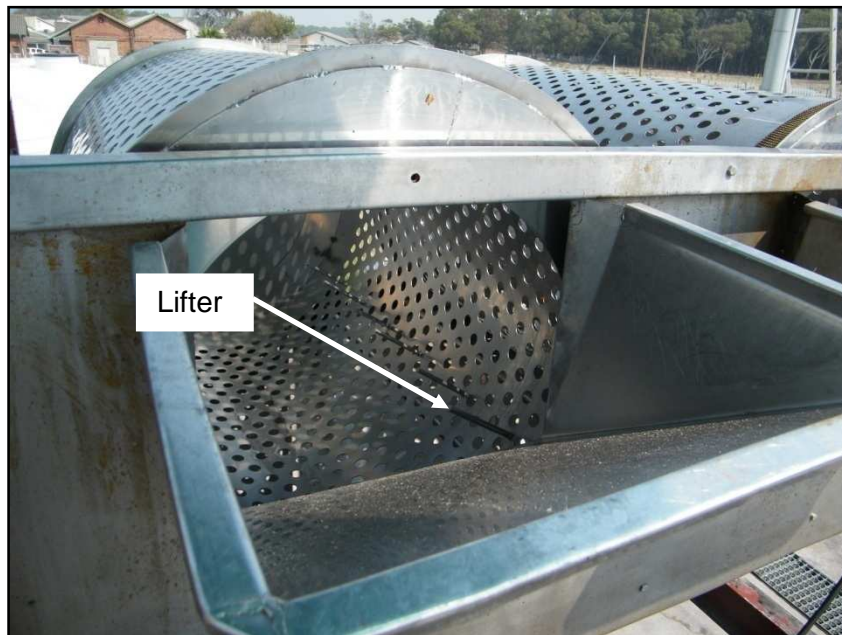

Figure 80 - A typical drum type destemmer as used by Flagstone Winery, South Africa.

90

Some wine cellars use a rotating drum without a beater shaft to separate the grape berries and stems (Figure 80). These machines look and work like an ore-mill used by mines to mill ore. Grape bunches are fed into the drum which is then rotated at a much slower speed than the drum of a traditional destemmer, while lifters on the inside of the drum lift the grape bunches. These drums also have holes in them to act like a sieve but are larger that the drums found in traditional destemmers. The berries are removed from the stem as the grape bunches are milled inside the drum and the berries are then separated from the stems through the holes in the drum. Removing the stems from the drum is a problem - these machines are usually filled with a certain amount of grapes, rotated until the berries are removed and then stopped to remove the stems before filling it with grapes again. As a result, these machines have a low processing rate and are only used for very low production volumes.

Figure 81 - The EuroSelect destemmer from Scharfenberger (Scharfenberger, 2010).

Scharfenberger recently introduced an entire new type of destemmer called the EuroSelect destemmer (Figure 81). It works on the same principal as the onboard destemmer offered by New Holland on their mechanical grape harvesting machine (See Section B.3.). Grapes are moved on a grid conveyor and the removal of the berries from the stems is done by four rows of beaters. These beaters differ from normal destemmers in the sense that they are flexible rubber "fingers" (Phillips, 2005). The speed of each row of beaters can be adjusted individually and in this way the winemaker can control which berries are removed and which are left on the stems. For example, green berries will be removed at a different speed to the ripe berries, and by setting the rotation speeds of each row of beaters correctly, it is possible to remove only the ripe

berries and leave the unwanted green berries attached to the stems. The berries are then separated from the stems by falling through the grid conveyor. These machines are only capable of handling small quantities of grapes (8 tons per hour) and are aimed at more specialised, high quality wineries (Scharfenberger, 2010).
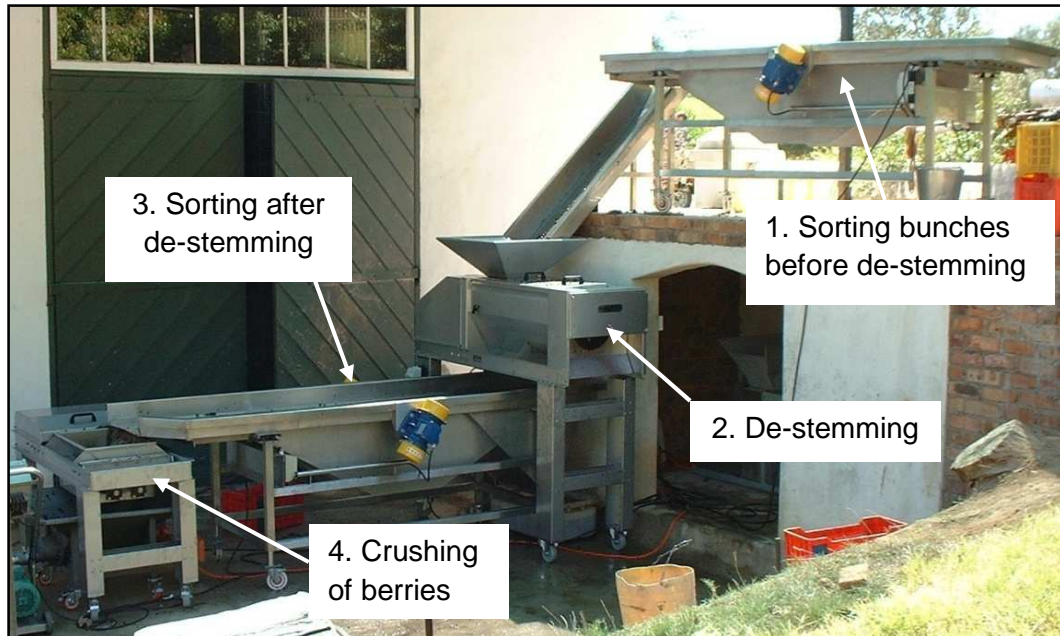
B.2. Post Processing and Sorting

Figure 82 - A typical setup at a cellar where grapes are sorted by hand before and after de-stemming (Amos, 2009).

Figure 83 - Grapes being sorted by hand (Amos, 2009).

92

Where grapes are processed in small volumes (less than 15 tons per hour), the grapes are often sorted by hand before and/or after de-stemming (Figure 82). A conveyor belt or vibration table is usually used to sort the grapes after de-stemming. This is done to remove any stems, leaves or other foreign objects from the berries, including raisins, rotten or green berries which can influence the wine negatively. Bad bunches (green or rotten) are removed by sorting the grape bunches before de-stemming. This very labour intensive process can be seen in Figure 83.

Mechanical grape sorting machines offer an alternative to manual sorting. The grapes are basically sorted by two sieving processes. A mechanical grape sorting machine called the Tommy, manufactured by C.M.A. has grapes enter on a vibration table with small holes where the juice is drained and small unripe berries and small pieces of broken stems are removed (Figure 84). The grapes are then fed onto a grid conveyor (Tommy belt) which is slightly vibrated to improve separation. The holes in the grid conveyor are just large enough for the berries to pass through while all the leaves and stems are removed by the grid conveyor (Prospero Equipment, 2010).
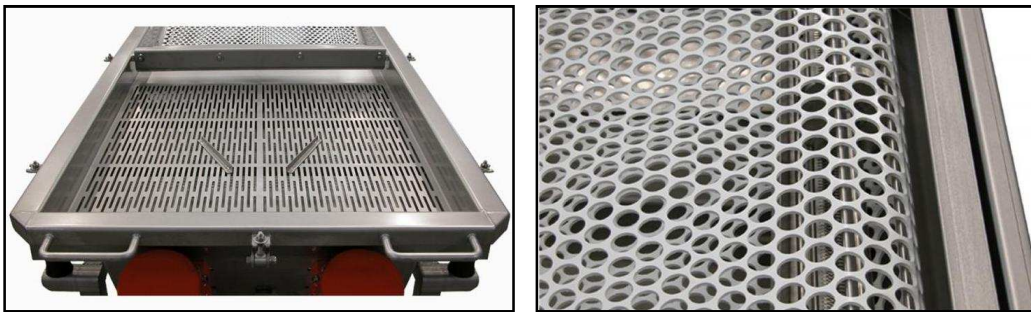

Figure 84 - The vibration table (left) and the grid conveyor (right) used on the Tommy mechanical grape sorter from C.M.A. (Prospero Equipment, 2010).

Recently machines have been developed that can sort the de-stemmed grapes optically by distinguishing between difference in shape and colour. Similar machines have been used in the separation of plastics, rice, beans and various other biomaterials including cherries, strawberries and Lingonberries (Buhler, 2010). The University of Cambridge used a Sortex optical colour sorter to sort various red and white cultivars. Using colour and shape to sort the de-stemmed grapes, they could remove up to 95% of all unwanted objects from the grapes (Falconer, 2006). The advantage when using colour sorting is that green and rotten berries can be removed as well. The Sortex machine used in these tests was an industrial optical colour sorter (Figure 85) but recently cellar equipment manufacturers have been developing optical colour sorting machines and software exclusively for the sorting of de-stemmed grapes. Optical automated sorting makes it possible to sort grapes to a degree that is not practical with hand sorting (Falconer et al., 2006). The colour of grapes that gets rejected or

accepted can be applied to a much closer tolerance and foreign objects mixed with the grape berries are rejected at higher level of reliability.
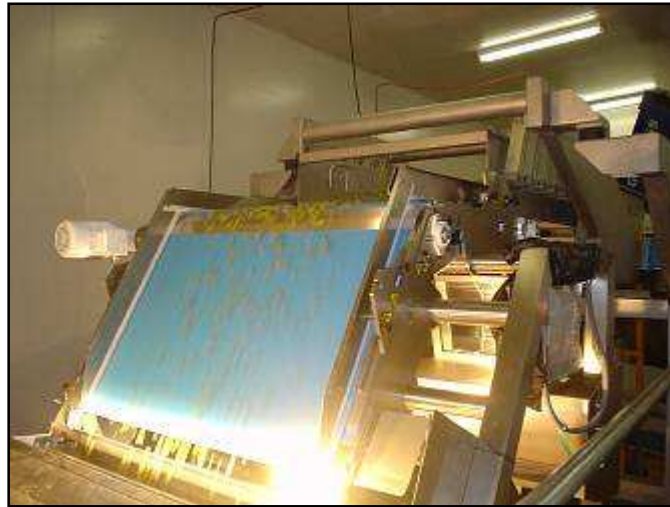

Figure 85 - The Sortex colour sorter processing Chardonnay grapes during tests done by Falconer (2006).
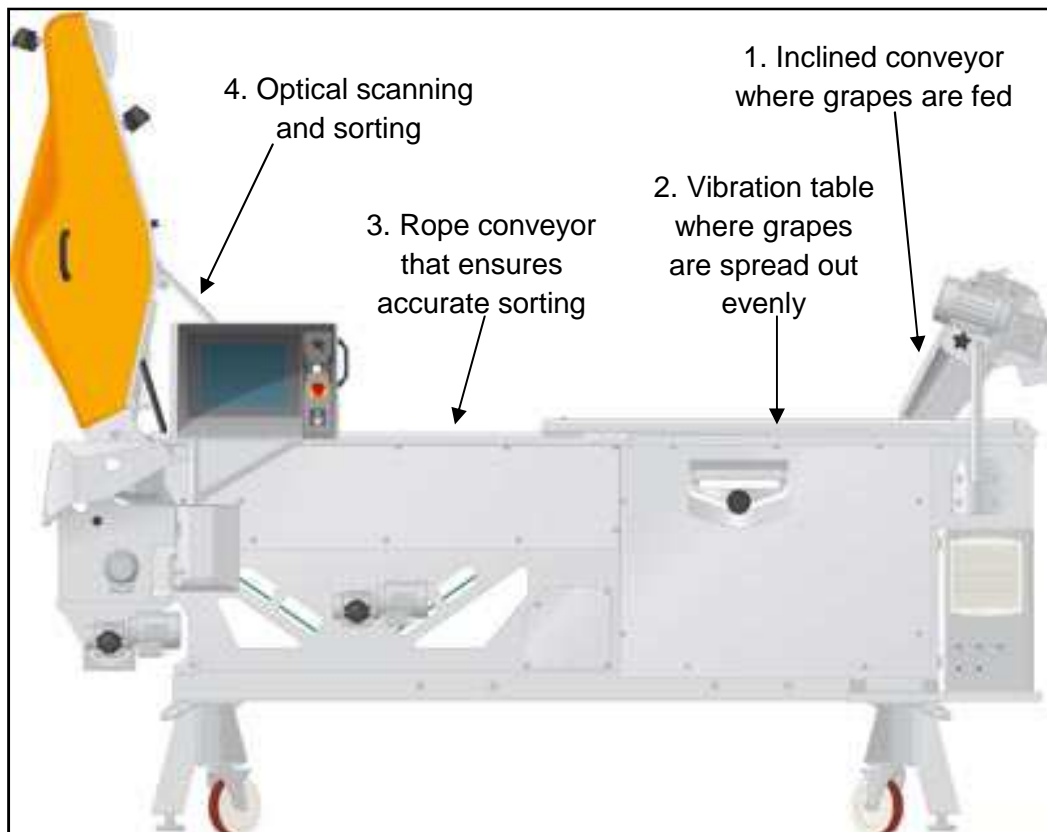

Figure 86 - The basic layout of the Selectiv' Process Vision optical sorter from Pellenc (Pellenc, 2010).

Since this is still a relatively new technology in the wine industry, only three optical sorting machines are currently available that are purpose built for grape

94

sorting: the Selectiv' Process Vision from Pellenc, the Vistalys Delta R2 from Bucher Vaslin, and the X-tri from Defranceschi.

Figure 87 - Inclined conveyor (white), vibration table and rope conveyor (left) on the Selectiv' Process Vision from Pellenc (Pellenc, 2010).
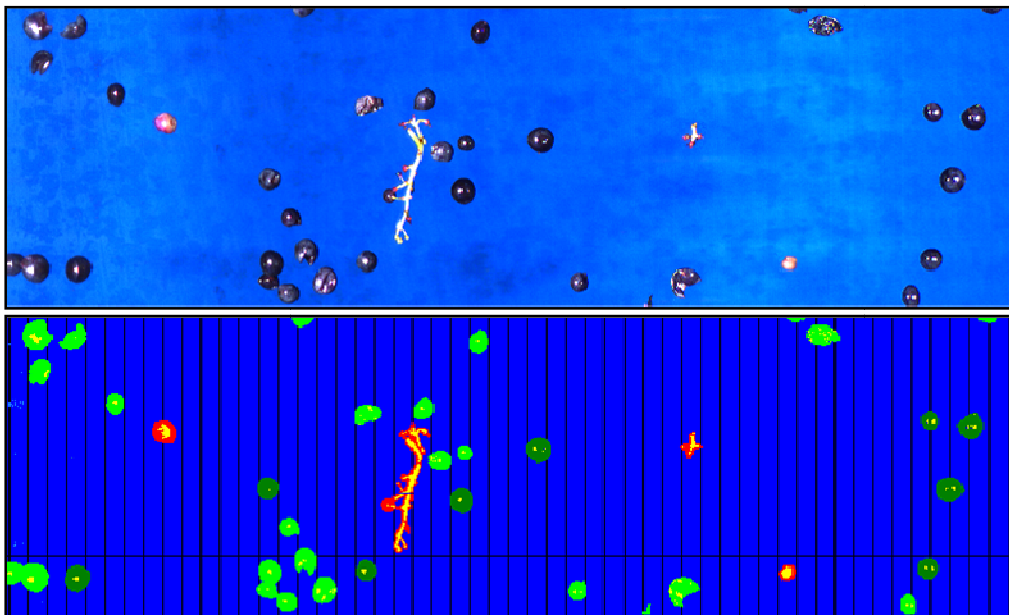

Figure 88 - Raw data from the optical scanner (top) and the processed data (bottom) that is used for the elimination process (Pellenc, 2010).

In the Selective' Process Vision machine, (Figure 86) the grapes enter on an inclined conveyor which moves in opposite direction and helps to eliminate small sticky waste (Figure 87). The grapes are then spread out evenly on a vibration table and are fed onto a rope conveyor (Figure 87). The rope conveyor is designed so that the material movement on the conveyor is limited which ensures

that the scanning and sorting process is done accurately. Figure 88 shows the raw data from the scanner as well as the processed data that is used for the selection process. A row of air nozzles are activated individually to eject the unwanted objects and berries that are identified by the scanning process. The time interval between scanning and ejection is 30 ms while the response time of this machine is rated to be close to 3 ms (Pellenc, 2010). These machines can handle up to 12 tons of grapes per hour.

B.3. Mechanical Grape Harvesters

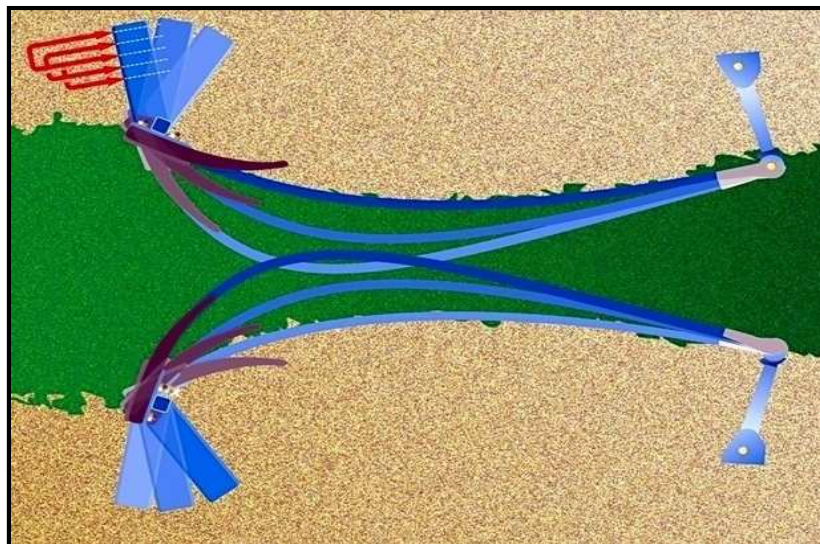Figure 89 - Basic layout of a mechanical grape harvesting machine (Smit, 2009).

Figure 90 - A top view of the working of the beaters of a mechanical grape harvester (Smit, 2009).

96

There are two ways of harvesting grapes, by hand or using a mechanical grape harvester (Figure 89). Harvesting grapes by hand is a labour intensive job and mechanical grape harvesting machines have become increasingly popular. Figure 89 shows the basic layout of a mechanical grape harvesting machine from New Holland. These machines remove the grapes from the vines using vibrating beaters (Figure 90). These beaters not only remove the grapes but also some leaves and twigs by means of a blower (Figure 91). As the grapes are removed from the vines, most of the berries are also removed from the stems. Under the right circumstances, these machines can remove all the grape berries from a vineyard while the stems stay attached to the vines. However, in normal operation, stems and twigs are removed with the grapes and some manufacturers offer a de-stemming attachment on their machines which removes the stems and twigs from the berries.
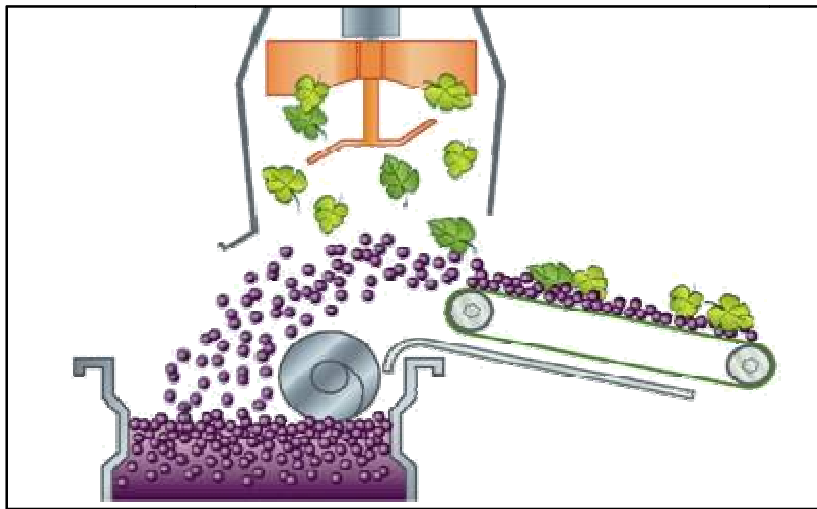

Figure 91 - The removal of leaves from the berries by using a blower (Smit, 2009).

Two of these destemmer attachments from two different manufacturers will be discussed briefly. The first is a destemmer attachment offered by New Holland on their mechanical harvesters (Figure 92). It uses a blower to suck away any leaves, or any other similar foreign objects. A conveyor mat with holes in, which act as a sieve, moves the grapes through three rows of beaters which remove the remaining berries from the stems. The berries go through the conveyor mat and into a collection bin and the stems are dumped back into the vineyard.

The second machine is a destemmer attachment from Pellenc, offered on their mechanical grape harvesters. This destemmer attachment is similar to the linear de-stemming machine from Pellenc, discussed earlier in this chapter. After a bunch has been removed from the vines, it is put through a small linear destemmer (Figure 78). When the berries have been removed from the stems, the berries are separated from the stems using a similar roller system to that shown in Figure 79.
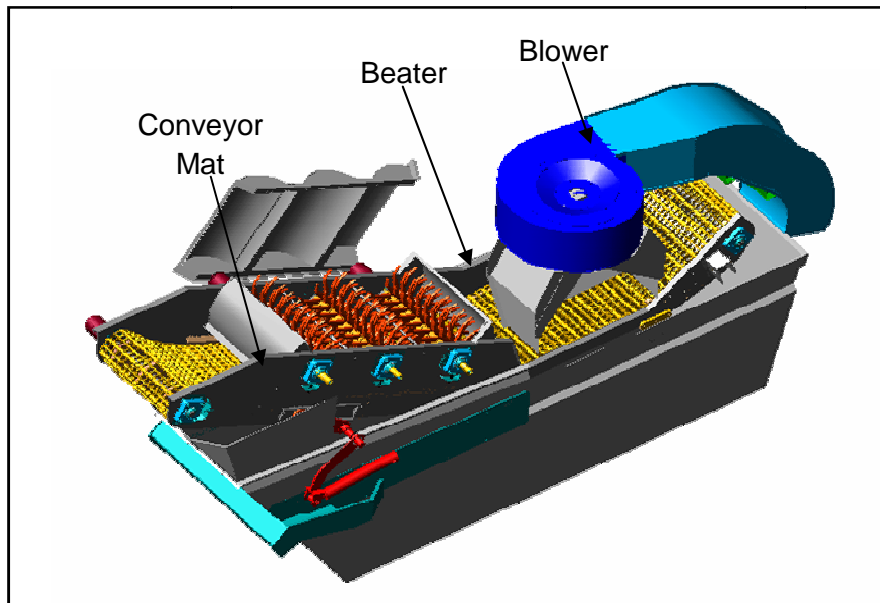
Figure 92 - A destemmer attachment offered by New Holland on their mechanical grape harvesters (Smit, 2009).

Mechanical grape harvesting machines have become increasingly popular in recent years. The increase in popularity can largely be attributed to the development of multifunctional machines. Manufacturers of mechanical grape harvesters have developed machines that can be converted into a wide variety of implements through the use of specially designed attachments. Attachments that are available includes: fertiliser spreader, soil cultivator, hole digger and stake driver, leaf remover, planter, pre-pruner, trimmer and sprayer (Smit, 2009). Mechanical grape harvesters can also be converted for the harvesting of olives, raspberries and blackcurrants.

Appendix C: Angle of Repose

C.1. Experiment

The angle of repose is a common calibration method used in granular mechanics. Although there is no formula to relate the angle of repose to the physical properties of the material, it is usually used on a trial-and-error basis to determine a set of parameters most suitable in the numerical simulation. The angle of repose is not only dependent on the inter-granular friction factor, but it is often used to estimate the friction factor.

The angle of repose is measured by piling up the granular material in question and measuring the angle at which it settles. This is then repeated using the numerical simulation and the parameters of the material in the numerical simulation (usually the friction factor) are adjusted until the granules settle at a similar angle. The main factors that influence the angle of repose in the numerical simulation include: friction factor, rolling resistance of granules, cohesion between granules and the stiffness of the granules.

Measuring the angle of repose of the grape berries was done by filling a rectangular container with approximately 30 kg of grapes berries. The bottom of the container was removed and the container was lifted up slowly. This resulted in an average angle of repose of 42° (Figure 93).

Figure 93 - An example of the measurement of the angle of repose.

C.2. Numerical Simulation

The angle of repose experiment was then simulated using a berry stiffness of 3000 N/m. During the experiments, it was observed that some of the berries were damaged during the destemming process and plenty of grape juice was released. The juice was very sticky and caused cohesion between the berries. Cohesion has an influence on the angle of repose and an increase in cohesion between particles can cause an increase in the angle of repose. However, the cohesion

between the berries only appeared after the destemming process when the grape juice was released. If the angle of repose was measure using berries with no juice, a lower angle of repose could be expected.

The cohesion effect was therefore included in the numerical model during the simulation of the angle of repose. Since the presence of grape juice was limited during the other experiments, it was not included in any of those numerical models because simulating the cohesion decreased the computational efficiency of the numerical model.

Using the weight and volume of the berries that were used in the experiment, it was calculated that more or less 19 500 berries were used in the experiment. To improve the computational efficiency, it was scaled down and 11 000 balls were used in the numerical model. The dimensional ratios of the container used in the experiment were replicated exactly in the numerical model and the floor was modelled by a flat grid of clumped balls. The numerical simulation started by filling the container with the balls and allowing them to settle. The container was then lifted at a similar speed as in the experiments while the balls flowed out of the container and settled in a heap. Once the heap of balls had settled, the angle of repose was measured (Figure 94).
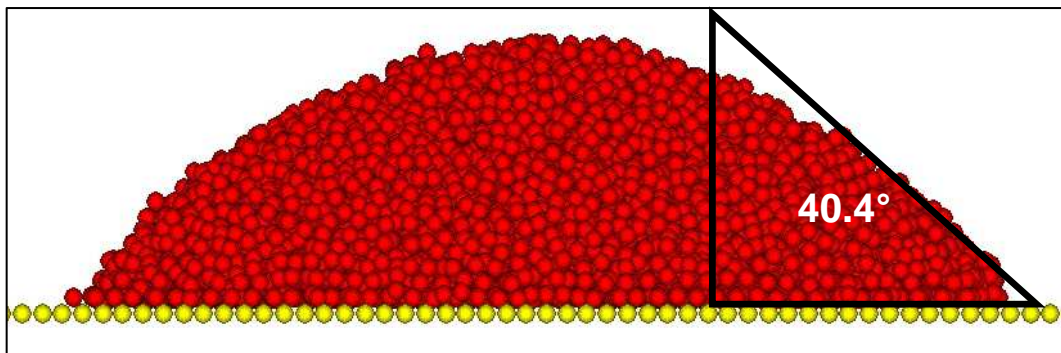

Figure 94 - The angle of repose as simulated in DEM.

The cohesion between the balls was modelled using contact bonds. The strength of the bonds varied from 1e-3 N to 10e-3 N, which was between 5% and 66% of the weight of an average ball. The bonds were constantly set during the simulation and as soon as a bond was broken, new bonds were formed again between balls that were in contact.

Figure 95 shows the effect of the friction coefficient on the angle of repose when using various bond strengths. The red line shows the result from the experiments (42°). Figure 96 shows the effect of the bond stren gth on the angle of repose when using various friction coefficients. Both these two graphs show that as soon as contact bonds were used, there was a steep increase in the angle of repose. As the bonds strengths were increased, the angle of repose increased more gradually. The change in friction coefficient also had a fairly gradual increasing

effect on the angle of repose. These two graphs show that there are various combinations of friction coefficient and bond strength that would result in an angle of repose that is equal to the experimental result of 42°. Figure 94 shows the angle of repose when using a friction coefficient of 0.1 and a bond strength of 5e-3 N. If the angle of repose needs to be modelled accurately, further research is needed to determine the effect of the ball friction alone on the angle of repose and the subsequent effect of the cohesion.
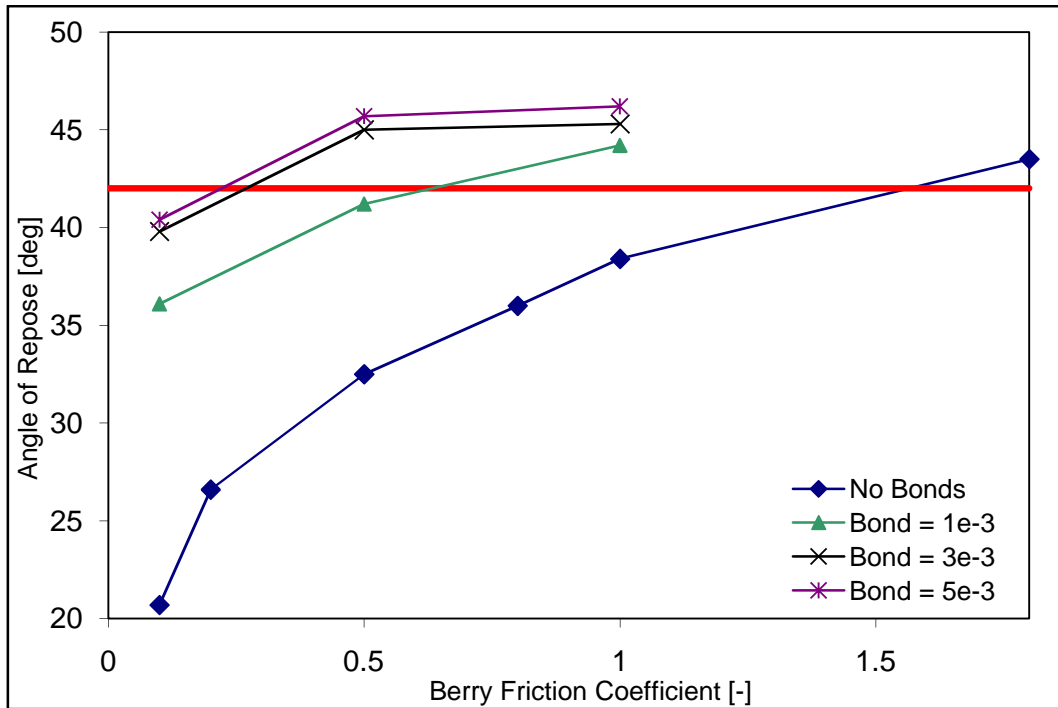

Figure 95 - A comparison of the berry friction coefficient to the angle of repose using various bond strengths.
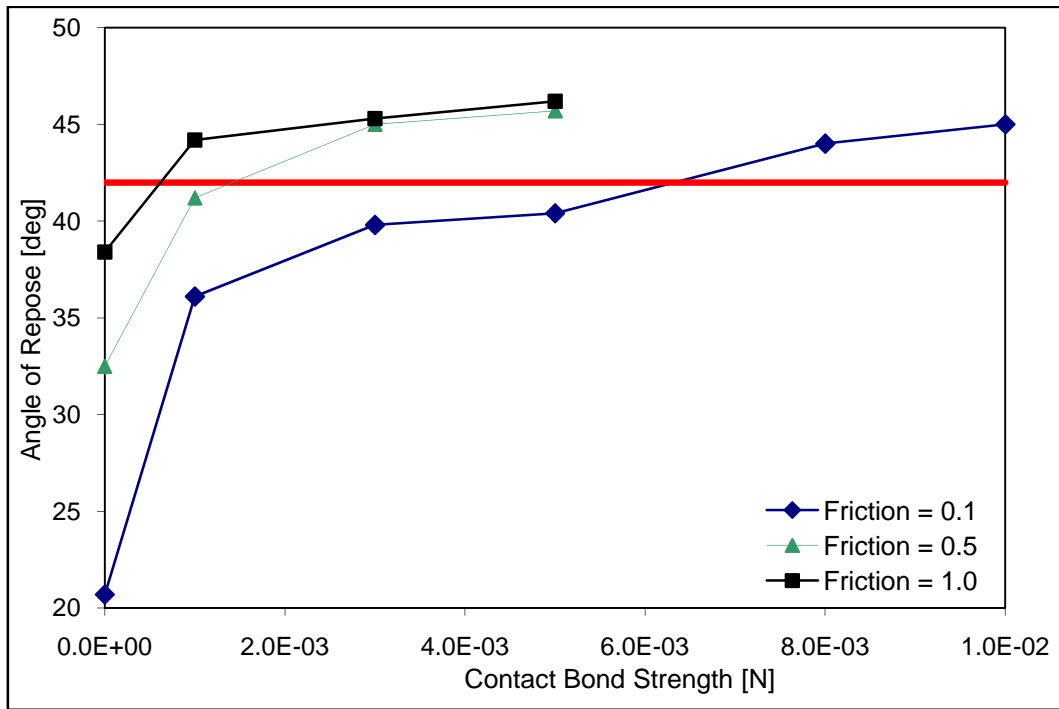
Figure 96 - A comparison of the bond strength to the angle of repose using various friction coefficients.

Appendix D: Vibration of Bunch

Although the destemmers used in this study are the preferred way of destemming grape bunches, another way of destemming was investigated. The removal of the berries from the stems using vibration was briefly investigated and used as a case study to test the application of the numerical model of the bunch when vibrated.

D.1. Experiments

Bunches were clamped at the top of the main stem and vibrated vertically. It was found that the berries were best removed at a frequency of between 17 and 18 Hz. The amplitude that was used varied between 9 and 12 mm and was the maximum amplitude that could be achieved with the tests equipment. A permanent magnet shaker (V555) with a 1 kW linear power amplifier (PA 1000 L), both manufactured by Ling Dynamic Systems, were used to conduct the experiments. It is possible that larger amplitudes could remove the berries faster and more efficiently. A high speed camera was used to capture the behaviour of the bunch at 200 frames per second. The images from the high speed camera were also used afterwards for the calibration of the amplitude (Figure 97).

The bunches were weighed before each test and the number of berries that were removed and the number that were still attached to the stems were recorded. The duration, frequency and amplitude were varied between the tests. The duration of each test was either 30 or 40 seconds.
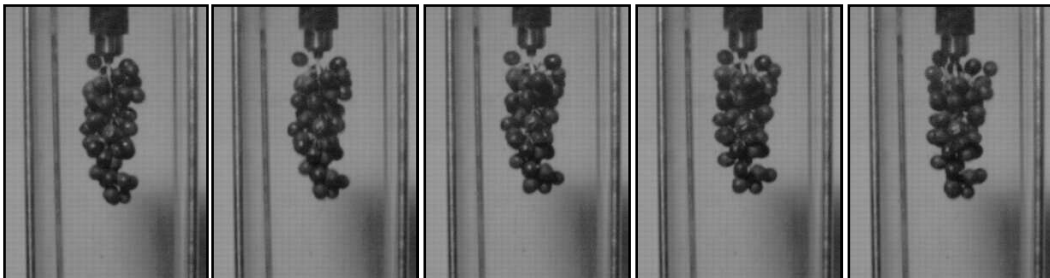

Figure 97 - Vibration of bunch as captured by high speed camera at 200 fps.

It was found that the tests were reasonably repeatable and the general consensus was that more berries were removed at 17 Hz than at 18 Hz. It also appeared that there was little difference between the number of berries removed at 30 seconds and 40 seconds. Since these tests were only done as a case study (for comparison with DEM results) and to investigate the applicability of the removal of berries from the stems by using vibration, only a few tests were conducted. Not enough test data is available to draw any more conclusions.

D.2. DEM Model

To simulate the vibration of the grape bunches, the speed of the first ball of the main stem was constantly adjusted to follow a sinus wave. The bunches were

103

simulated under vibrations with frequencies, amplitudes and time durations that were equal to the settings used during the experiments.

The bunches were built in the same way as in all the other simulations. A box was built around the bunch to collect the berries that broke from the stems. Pictures of the bunch under vibration were created at a rate that equals more or less 10 pictures per vibration cycle. These pictures were then used afterwards for visual comparison to the pictures that were recorded during the experiments by the high speed camera. All the bonds were constantly monitored and all bonds that broke were recorded together with the time, position, maximum stress etc.

In the first simulations, it was found that the bond breaking strength of the stems was too low and all the main stems broke. The bond strength of the main stem was increased to a value of 1 GPa. Further simulations showed that the bond strength of the berries was also too low, since all the berries were removed from the stems. The bond strength of the berries was increased to 6 MPa.

D.3. Results

Results from the simulation were compared to the results from the experiments. A visual comparison of the pictures taken by the high speed camera and the pictures created during the simulation was also done. The bunches were all simulated under a vibration of 17 Hz and 18 Hz for a total time of 40 seconds. The results were then obtained by determining the number of berries that were removed at 30 seconds and the total number of berries removed at 40 seconds.
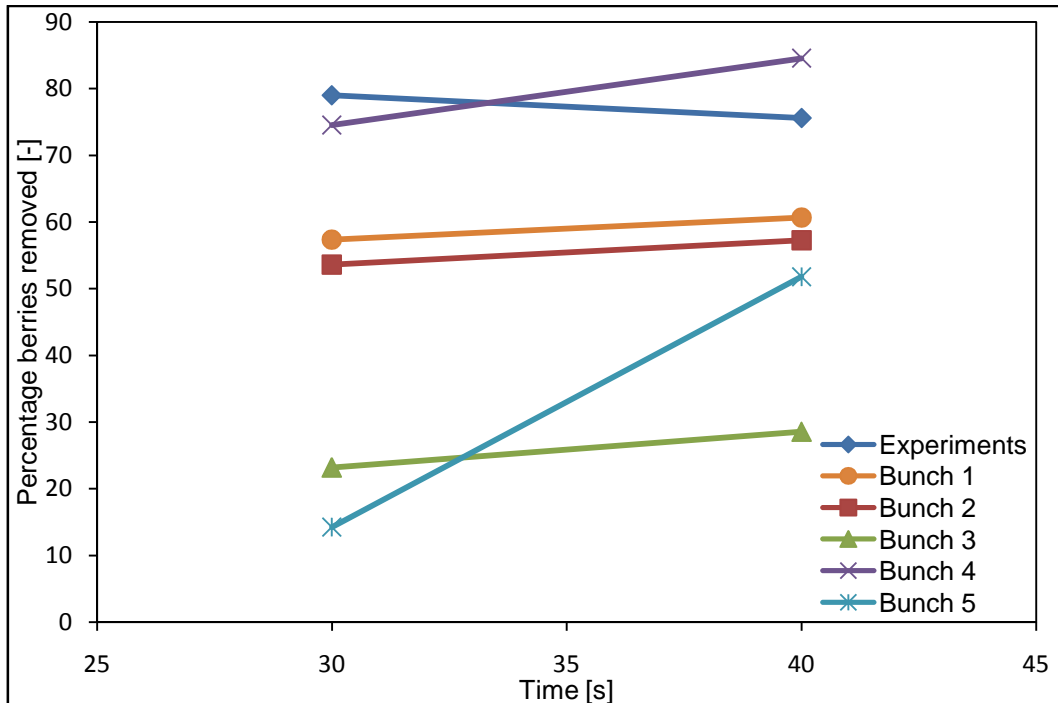

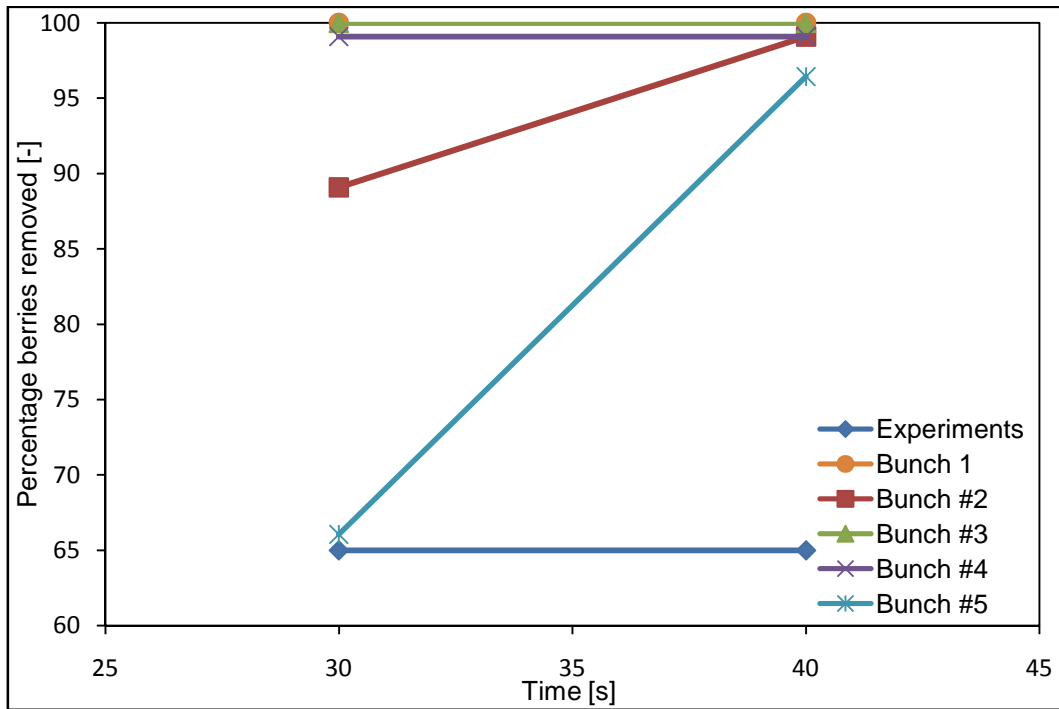Figure 98 - The percentage of berries removed at 17 Hz.

Figure 99 - The percentage of berries removed at 18 Hz.

The percentage of berries removed is compared to the vibration time in Figure 98 and Figure 99 for a vibration frequency of 17 Hz and 18 Hz respectively. One would expect that when the bunch was vibrated for a longer time duration, more berries would be removed. From the experimental results, a slight decrease or no change at all was found in the percentage of berries removed when the time duration was increased. However, since the number of experiments was too low, a final conclusion cannot be reached. The simulation results all showed an increase in the number of berries that was removed after 40 seconds. When the bunches were simulated under a vibration of 18 Hz, some of them lost all their berries after a duration of only 30 seconds.

When the percentage of berries removed is compared to the vibration frequency at 30 and 40 seconds in Figure 100 and Figure 101 respectively, one can see that the experimental trend does not compare well with the simulation trend. In the experiments it was found that the percentage of removed berries decreased when the frequency was increased. However, the simulations showed an increase in the percentage of berries removed with an increase in the vibration frequency.
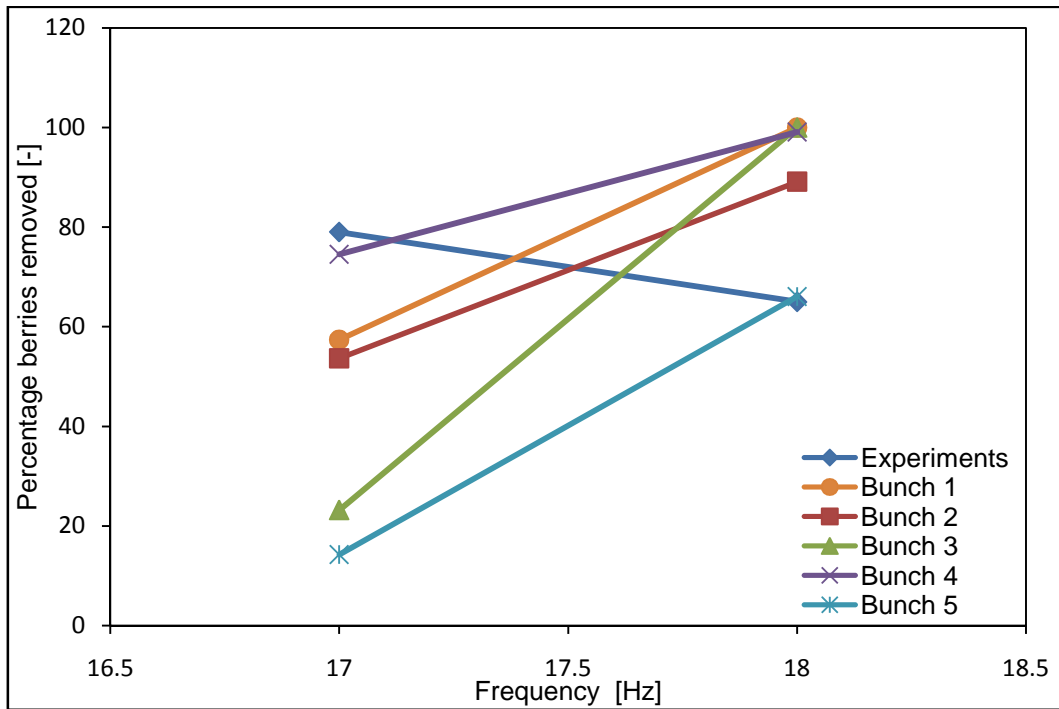
Figure 100 - The percentage of berries removed at 30 seconds for different frequencies.
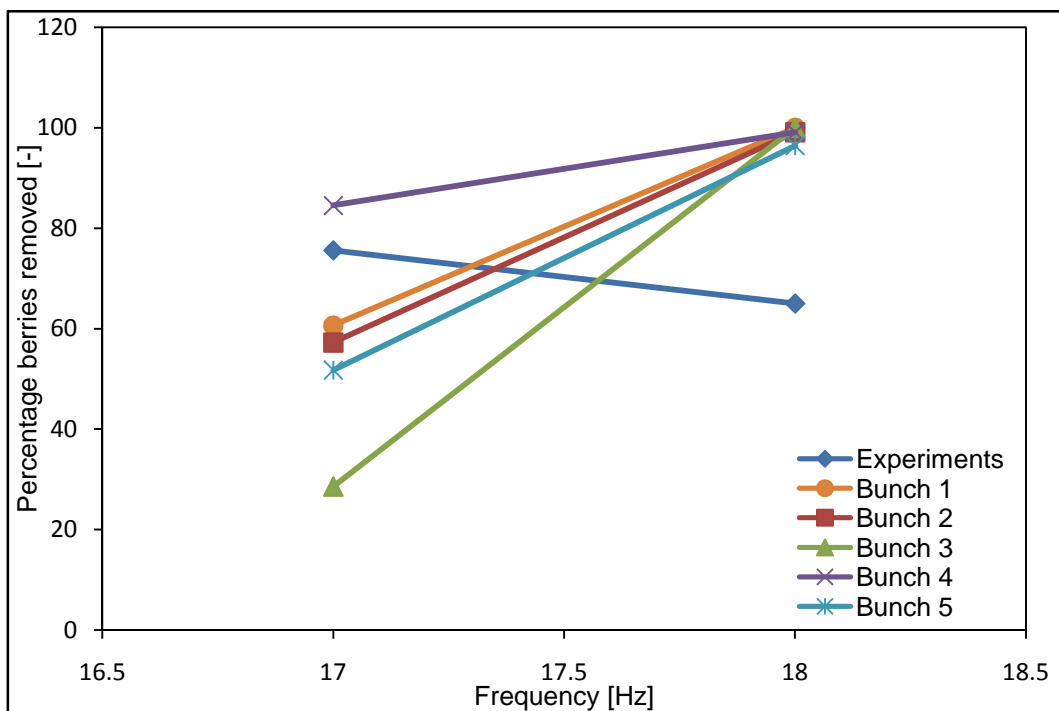

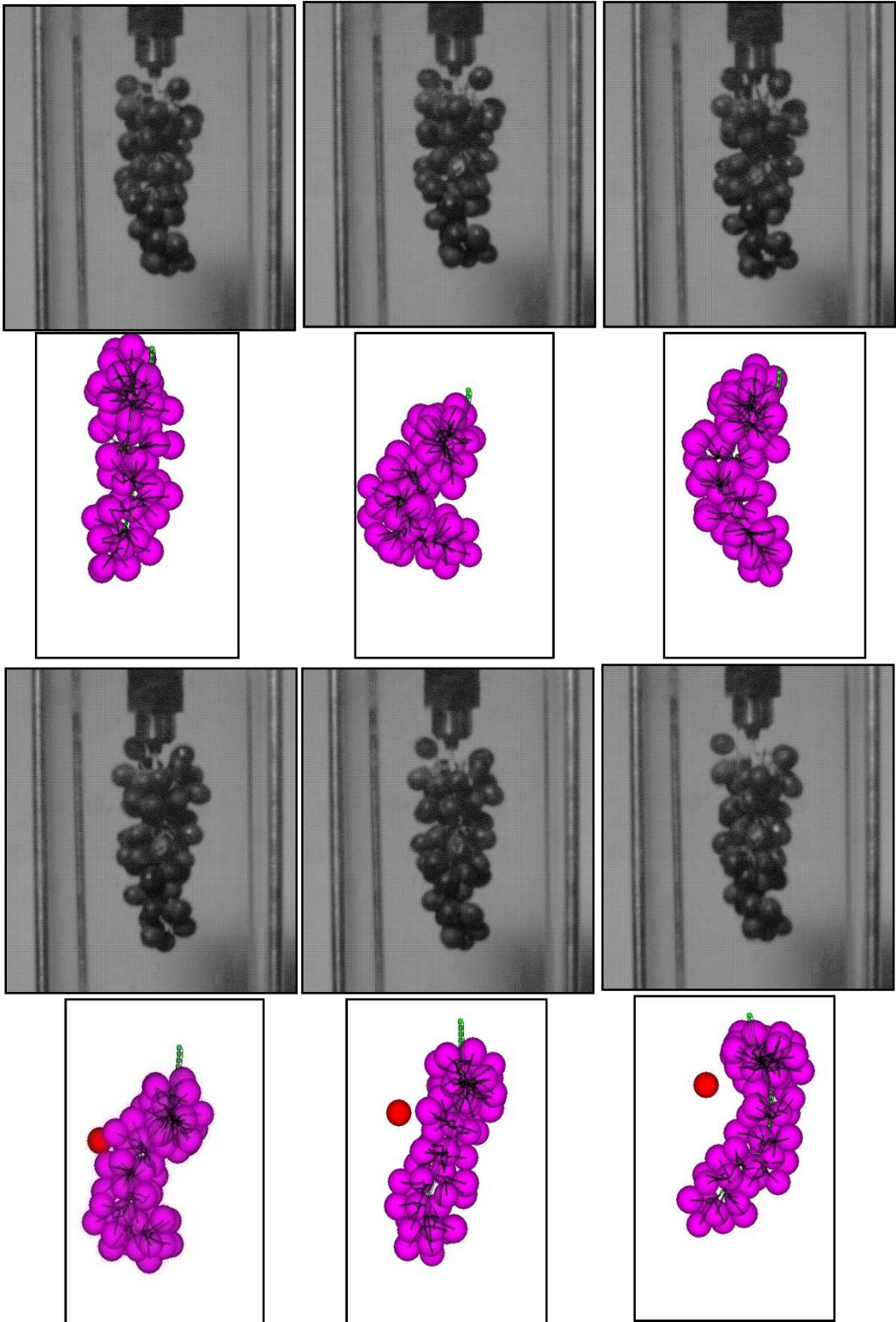Figure 101- The percentage of berries removed at 40 seconds for different frequencies.

Figure 102 - Visual comparison of the vibration of a grape bunch in the DEM simulation to the experiments.

The removal of the berries from the stems under vibration could be simulated using DEM, but with poor accuracy. When vibrating a bunch, high speeds and accelerations are present inside the bunch. Simulating the visco-elastic effect of the bunch materials more accurately could improve the results. Very little experimental data was available to make accurate conclusions and further research is needed.

Appendix E: Ball-Wall Stiffness

In the linear contact model in PFC^{3D} the stiffness of the balls (k_b) and the walls (k_w) are modelled as springs. When a ball makes contact with a wall, the contact is modelled as two springs in series. The calculation of the resultant stiffness of a ball-wall contact (k_{b-w}) is shown in equation 90 and a schematic layout of the ball-wall contact is shown in Figure 103.

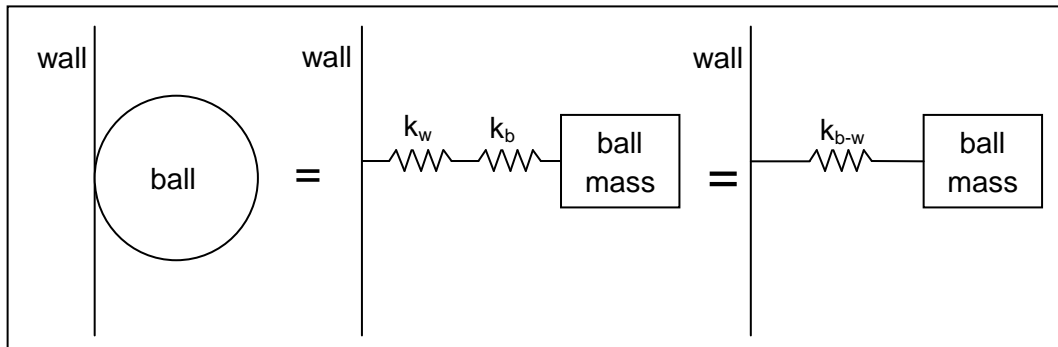$$k_{b-w} = \frac{k_b * k_w}{k_b + k_w} \tag{90}$$

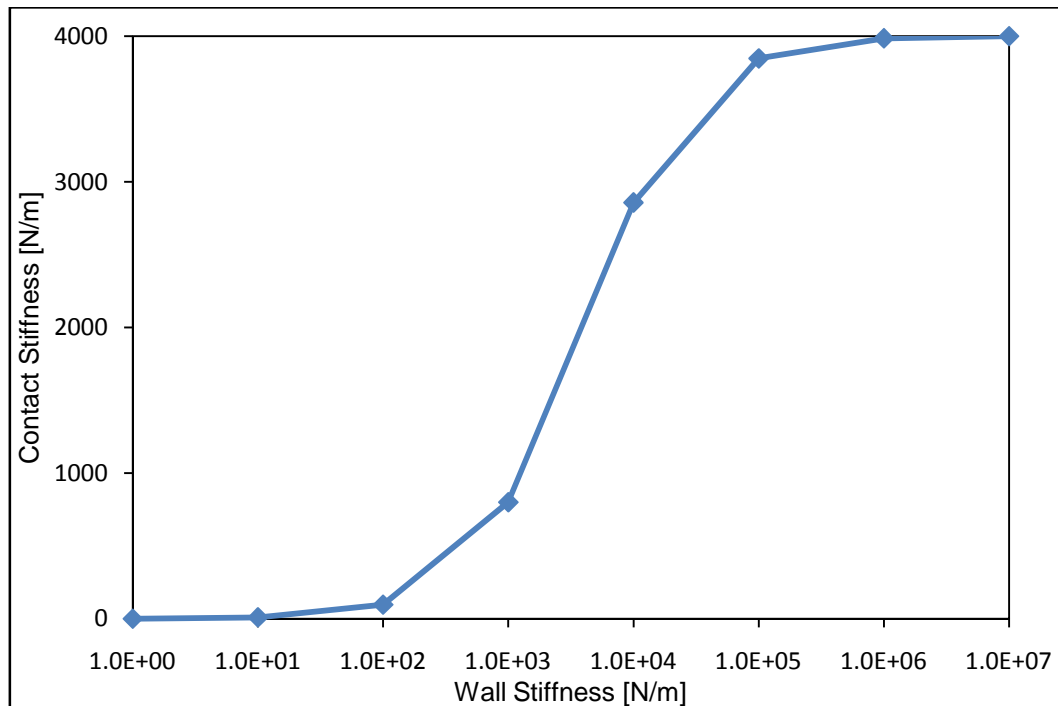Figure 103 - Schematic layout of a ball-wall contact.

Figure 104 - The resultant contact stiffness with increasing wall stiffness and a constant ball stiffness (4000 N/m). Note that the x-axis uses logarithmic scaling.

When the wall stiffness is increased in equation 90, while the ball stiffness is kept constant, the contact stiffness will eventually converge to a maximum value that tends towards the ball stiffness. Figure 104 shows a graph where the ball

stiffness is kept at 4000 N/m and the wall stiffness is varied from zero to 10^7 N/m. When the wall stiffness reaches the square of the ball stiffness, the contact stiffness remains at 4000 N/m. Note that the bottom axis of the chart uses a log scale.

During ball-wall contact in high contact force situations, the deflection of the spring in the ball can be larger than the radius of the ball. The result is that the ball's centre moves through the wall and immediately the original ball-wall contact is lost and a new ball-wall contact is created in the opposite direction, on the opposite side of the wall. The result is that the ball moves through the wall. In Figure 105 a cylindrical wall is moving to the right at a fixed velocity and makes contact with a ball. Before the ball can accelerate to the speed of the cylinder, the deflection of the ball is more that its radius and the ball moves through the wall. Tests have been done using timesteps as small as 10^{-10} s to verify that this is not a numerical error. The contact of the ball and the wall has also been investigated by calculating the deflection of the spring during such a contact using simple harmonic motion equations of a spring-mass system. The calculations reveal that the spring can deflect more than the radius of the ball in such a contact.
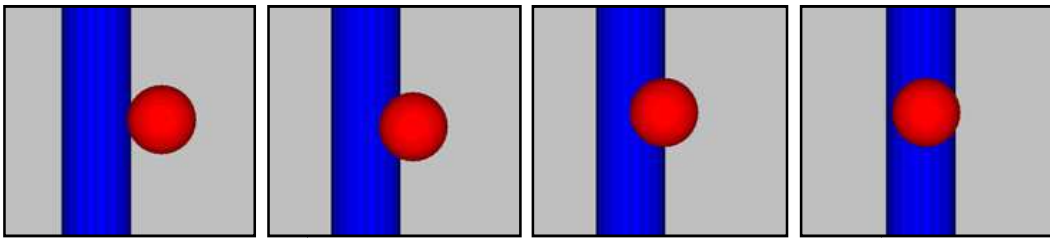

Figure 105 - A ball passing through a moving cylinder in PFC^{3D}.

To prevent the balls from passing through the walls, the contact stiffness needs to be increased. As shown in Figure 104, the maximum contact stiffness cannot be larger than the smallest stiffness in a contact. Thus, infinitely increasing the wall stiffness does not solve the problem. The ball stiffness needs to be increased but this could have a negative effect on the mechanical behaviour of the system.

A possible solution for this problem is to use multiple walls. More than one wall is created at the same location. A ball-wall contact is created between the ball and each of the walls. These contacts act in parallel and as a result the reaction force on the ball is multiplied by the number of walls that it is in contact with (Figure 106) The calculation of the resultant ball-wall contact stiffness is shown in equation 91 where n is the number of walls in the same location.

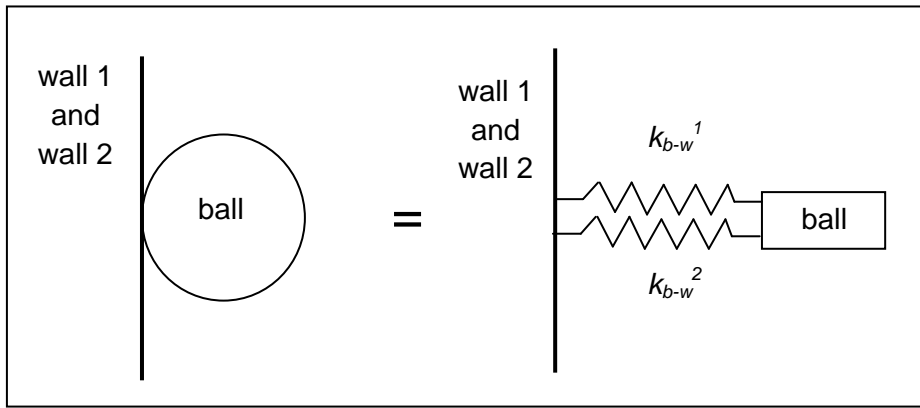$$k_{total} = \sum_{i=1}^{n} k_{b-w}^i$$

(91)

Figure 106 - Ball-wall contact using multiple walls.

By using multiple walls at the same location, the ball-wall contact force can be increased to exceed the ball stiffness, while the ball-ball contact force is unaffected. In this study, the walls were not placed at the same location. Instead the walls were offset from each other to create an increase in the stiffness as the deflection (overlap) of the ball increases. A schematic layout of two walls at an offset is shown in Figure 107. Initial ball-wall contact will yield the same contact stiffness as when using only a single wall. When the ball deflection is equal to the offset between the walls, the ball will make contact with the second wall and another parallel contact force will be created.
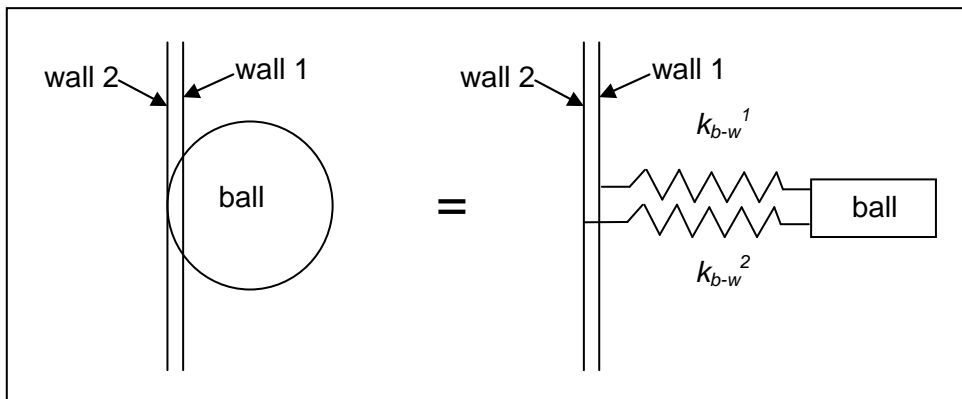

Figure 107 - Ball-wall contact with the walls offset.

By using multiple walls at various offsets, the contact force is increased stepwise as the ball makes contact with more walls. In this way a non-linear contact can be modelled very closely in a piecewise linear fashion. Furthermore, the stiffness of each wall can be set individually in order to create a contact model that models other non-linear contacts very closely.

Reference

Amos, H., 2009. Personal inteview: Destemmers. *Magitec Engineering*, 30 January.

Buhler, 2010. *Buhler Sortex E*. [Online] Available at: www.buhlergroup.com [Accessed 16 September 2010].

Diemme, 2010. *Diemme Winemaking*. [Online] Available at: www.diemme-spa.com [Accessed 22 September 2010].

Falconer, R., 2006. *Automated Sorting of Winegrapes*. [Online] Available at: www.cheng.cam.ac.uk [Accessed 16 September 2010].

Falconer, R., Liebich, B. & Hart, A., 2006. Automated Color Sorting of Hand-Harvested Chardonnay. *American Society for Enology and Viticulture*, 4(57), pp.491-96.

Goussard, P.G., 2008. *Grape Cultivars for Wine Production in South Africa*. 1st ed. Green Point: Cheviot Publishing.

Goussard, P.G. & Du Toit, W., 2010. Personal Interview. *Stellenbosch: Department of Viticulture and Oenology*, 26 January.

Groenewald, J., 2009. *Determining of Grape Properties for use in DEM Simulations*. Final Year Project. Stellenbosch: Stellenbosch University Department of Mechanical and Mechatronic Engineering.

Herold, B., Geyer, M. & Studman, C.J., 2001. Fruit contact pressure distributions - equipment. *Computers and Electronics in Agriculture*, (32), pp.167-79.

Imma, 2010. *Vertical Destemmer*. [Online] Available at: www.imma.it [Accessed 22 September 2010].

Itasca, 2003. *PFC3D - Particle Floe Code in 3 Dimentions. Online Manual*. [Online] (2) Available at: www.itascacg.com [Accessed 30 January 2008].

Kidd, M., 2010. *Personal Interview: Statistical Analysis of Data*. Stellenbosch: Centre for Statistical Consultation, Dept of Statistics and Actuarial Sciences.

Pellenc, 2010. *Pellenc*. [Online] Available at: www.pellenc.com.au [Accessed 16 September 2010].

Phillips, C., 2005. Product Review: Destemmers. *Wine Busisness Monthly*, 15 June.

Prospero Equipment, 2010. *C.M.A Grape Conveyors: Automatic Grape Sorter*. [Online] Available at: www.wineryequipment.com [Accessed 16 September 2010].

Raji, A.O. & Favier, J.F., 2004a. Model for the deformation in agricultural and food particulate materials under bulk compressive loading using discrete element method. I: Theory, model development and validation. *Journal of Food Engineering*, (64), p.359–371.

Raji, A.O. & Favier, J.F., 2004b. Model for the deformation in agricultural and food particulate materials under bulk compressive loading using discrete element method. II: Compression of oilseeds. *Journal of Food Engineering*, (64), pp.373-80.

Scharfenberger, 2010. *Scharfenberger Maschinenbau*. [Online] Available at: www.scharfenberger.de [Accessed 22 September 2010].

Smit, Q., 2009. New Holland Mechanical Grape Harvesters. In *Fruit and Winegrowers Expo*. Cape Town, 2009.

Van Zeebroeck, M. et al., 2008. The simulation of the impact damage to fruit during the passage of a truck over a speed bump by means of the discrete element method. *Biosystems Engineering*, (101), pp.58-68.

Van Zeebroeck, M. et al., 2006. The discrete element method (DEM) to simulate fruit impact damage during transport and handling: Case study of vibration damage during apple bulk transport. *Postharvest Biology and Technology*, (41), pp.92-100.

Van Zeebroeck, M. et al., 2003. Determination of the dynamical behaviour of biological materials duringimpact usinga pendulum device. *Journal of Sound and Vibration*, (266), pp.465-80.

Van Zeebroeck, M. et al., 2007a. The effect of fruit properties on the bruise susceptibility of tomatoes. *Postharvest Biology and Technology*, (45), pp.168-75.

Zhang, X. & Vu-Quoc, L., 2000. Simulation of chute flow of soybeans using an improved tangential force-displacement model. *Mechanics of Materials*, (32), pp.115-29.

Zickler, 2009. *Zickler*. [Online] Available at: www.zickler-gmbh.de [Accessed 22 September 2010].